



TECHNISCHE UNIVERSITÄT MÜNCHEN
FAKULTÄT FÜR INFORMATIK

Lehrstuhl für Echtzeitsysteme und Robotik

Hybrid Parallel-Serial Micromanipulator for Assisting Ophthalmic Surgery

M. Ali Nasser

Vollständiger Abdruck der von der Fakultät für Informatik der Technischen Universität München
zur Erlangung des akademischen Grades eines

Doktor-Ingenieurs (Dr.-Ing.)

genehmigten Dissertation.

Vorsitzender: Univ.-Prof. Dr. Nassir Navab

Prüfer der Dissertation: 1. Univ.-Prof. Dr.-Ing. Alois Knoll

2. Univ.-Prof. Dr. rer. nat. Tim C. Lüth

3. Univ.-Prof. Dr. med. Dr. (Lond.) Chris P. Lohmann

Die Dissertation wurde am 22.09.2014 bei der Technischen Universität München eingereicht
und durch die Fakultät für Informatik am 31.03.2015 angenommen.

Abstract

Since 1970 when the first pars plana vitrectomy was performed, there has been an important change in trends in ophthalmic operations, particularly in Vitreo-retinal surgery. Not only the outcomes of these surgeries have been improved, but also nowadays it is even possible to find cure to ocular conditions that were untreatable before. The increasing positive results in the ophthalmic surgery are most commonly due to the new and better developed surgical techniques, improved low-gauge instrumentation, faster cutters and enhanced visualization tools. Nevertheless, the success of these procedures is still limited by the surgeon's precision and dexterity. In this line, it is the employment of assisting robots what sets a break through the human abilities barrier.

This thesis introduces a novel micro-manipulator which up-skills the ophthalmologists for performing vitreo retinal surgery. The up-skilling tasks which is augmented by this master-slave setup consists of precise movement, tremor cancellation, motion scaling and virtual fixture control. This compact robot, which is intuitively controlled by human surgeons, is designed to be adoptable to standard operation theaters without modification.

Zusammenfassung

Seit Einführung der Pars-Plana-Vitrektomie im Jahre 1970 gab es bedeutsame Fortschritte in der Ophthalmologie, insbesondere im Bereich Vitreoretinaler Chirurgie. Dabei wurden nicht nur Operationsergebnisse erheblich verbessert, vielmehr ist heutzutage die Heilung von Augenerkrankungen möglich, die zuvor als nicht behandelbar galten. Diese Verbesserungen in der Ophthalmochirurgie basieren vor allem auf neuen und weiterentwickelten Chirurgie-Methoden, zunehmende Miniaturisierung von Instrumenten, schnelleren Schneidwerkzeugen und modernen Bildgebungsverfahren. Nichtsdestotrotz werden die Operationsergebnisse immer noch sehr stark durch die Präzision und die Fertigkeiten des Chirurgen beeinflusst und damit limitiert. Dementsprechend stellt der Einsatz von Assistenzrobotern eine Möglichkeit zur Überwindung der Grenzen des Chirurgen dar.

In dieser Dissertation wird ein neuartiger Mikromanipulator vorgestellt, welcher die Möglichkeiten der Ophthalmologen bei der Vitreoretinalen Chirurgie wesentlich verbessert. Die Verbesserungen, die durch dieses Master-Slave-System erreicht werden, machen sich insbesondere in Form von präziseren Bewegungen, dem Eliminieren von Handzittern, der Bewegungsskalierung sowie der Fähigkeit zur Steuerung virtueller Fix- bzw. Sperrbereiche bemerkbar. Der entwickelte kompakte Roboter, welcher auf sehr intuitive Weise vom Chirurgen bedienbar ist, besitzt ein Design, das eine einfache Integration in Standard Operationssälen ohne Adaptierungsaufwand erlaubt.

Acknowledgements

It is with immense gratitude that I acknowledge the support and the help of my engineering advisor, Alois Knoll and my colleagues from the Robotics and Embedded Systems Institute of TUM especially Suraj Nair. Furthermore, I acknowledge my medical advisor, Chris P. Lohmann and his team from Ophthalmology Clinic of Klinikum Rechts der Isar, especially, Mathias Maier, Danie Zapp and Karin Kobuch.

This thesis would have remained a dream without all the support from Ursula Mühle and the management team of Graduate School of Information Science in Health (GSISH), Katharina Lang and Petra Dorfner. I am indebted to my students who were the driving force behind most of the practical works of this project and Aaron Pereira who proof reads this thesis.

I dedicate this thesis to my parents and I share the credit of my work with Martin Eder.

Contents

List of Figures	vii
List of Tables	xi
1 Introduction	1
1.1 Background and Motivation	1
1.1.1 Minimally Invasive Surgery (MIS)	2
1.1.2 Robotic Surgery	3
1.1.3 Ophthalmic Operation	4
1.1.4 Vitreo-Retinal Surgery	4
1.1.5 Retinal Vein Occlusion	5
1.1.6 Retinal Vessel Cannulation Approaches	8
1.1.7 Difficulties for the Human Surgeons	10
1.1.8 Robotic Ophthalmic Surgery	11
1.2 Problem Statement	11
1.3 Contribution	11
1.4 Outline	11
2 Literature Review	13
2.1 Robotic Devices in Surgical Application	13
2.2 Robots for Assisting Ophthalmic Surgery	14
2.3 Limitations of Current Setups	20
2.4 Motivation	20
3 Clinical Studies and Requirement Analysis	21
3.1 Tracking Surgical Motion	21
3.1.1 Background	21

CONTENTS

3.1.2	Methodology and Experiments	22
3.1.3	Data Acquisition and Post-processing	26
3.1.4	Motion Requirements	26
3.1.5	Safety and Emergency	28
3.1.6	Conclusion	29
3.2	Eye Model	30
3.2.1	Eye ball models: state of the art	30
3.2.2	Developed Models	31
3.2.3	Meshed Model and Boundary Conditions	31
3.2.4	Material Properties	32
3.2.5	Results	33
3.2.6	Eyeball FEA Model Conclusion	35
3.3	Design Requirements	36
4	Kinematics	37
4.1	First Prototype	37
4.1.1	Design and Development	37
4.1.2	Evaluation	38
4.1.3	Results	38
4.2	Parallel Coupled Joint Mechanism (PCJM)	39
4.2.1	Mathematical Model	40
4.2.2	CAD Model	41
4.2.3	Kinematics Analysis	42
4.2.4	Advantages of PCJM over Serial Prismatic and Revolute Joint Configuration	43
4.3	Serial Configuration	44
4.3.1	Mathematical Model	44
4.3.2	CAD Model	45
4.3.3	Kinematics Analysis	46
4.3.4	Reachability Analysis	48
4.3.4.1	Workspace	48
4.3.4.2	Reachability within the Eye	49
4.3.4.3	Model of the Eye	50
4.3.5	Optimum Location of the Eye	51

4.3.6	Comparison to Other Locations	52
4.3.7	Experimental Evaluation	54
4.4	Results	59
5	Dynamics	61
5.1	Dynamic Analysis of a PCJM	62
5.1.1	Position and Orientation Control	64
5.1.2	Feedback Linearization of the PCJM	65
5.1.3	A control law for the PCJM	66
5.2	Dynamic Analysis of the robot	67
6	Physical Design and Fabrication	71
6.1	Piezo Actuators	71
6.2	PCJM Fabrication	73
6.3	Robot Fabrication	74
6.4	Mounting Mechanism	77
7	Control and Software Architecture	79
7.1	Linear Piezo Positioner Analysis	79
7.1.1	Velocity-to-Frequency Mapping	81
7.1.2	Calibration Procedure	81
7.2	Control Design	84
7.2.1	Input Device Mapping	84
7.2.2	P-Control	86
7.3	Virtual Fixtures	87
7.3.1	Remote Center-of-Motion	87
7.3.2	Further Applications	89
7.3.2.1	Automatic Location of the RCM	90
7.3.2.2	Epiretinal Membrane Peeling	91
7.4	Simulation Environment	91
7.5	Implementation	93
7.5.1	Software Architecture	93
7.5.2	Hardware Setup	96
7.6	Middle-Ware Based Software Architecture	96

CONTENTS

8 Experiments	101
8.1 OR Compatibility Evaluation	101
8.2 PCJM Evaluation	102
8.3 Robot Evaluation	102
8.4 Virtual Fixture Evaluation	103
8.4.1 Experimental Setup	104
8.4.2 Experimental Results	104
9 Bench to Bedside Translation	111
9.1 Technology and Value Proposition	111
9.2 End User Benefits	111
9.3 Target Market and Market Size	112
9.4 Stakeholders	113
10 Conclusion an future work	115
10.1 Conclusion	115
10.2 Future work	116
10.3 Concluding Remarks	116
References	117

List of Figures

1.1	Trocar system	2
1.2	Anatomy of the Eye	3
1.3	Intra-operative configuration of 3 valve cannulas	4
1.4	Minimally invasive ophthalmic surgery setup	5
1.5	Vitreo-retinal surgery setup	6
1.6	What surgeon sees through ophthalmic microscope	7
1.7	Retinal images: occluded retinal vessels is seen here	7
1.8	Retinal vein cannulation approaches	8
2.1	Robots developed for ophthalmic surgery	14
2.2	Preceyes robotic setup designed and developed at TU/e	17
2.3	RCM mechanism designed and developed at TU/e	18
2.4	Steady-hand eye robot	18
2.5	Micron hand-held instrument	19
3.1	Coordinate frames for the experimental setup	23
3.2	Tracking setup	24
3.3	The position of sensor marked in each captured frame	25
3.4	Tool trajectory in 3D space	27
3.5	Tool position and orientation analysis	27
3.6	Tool linear and angular velocities	28
3.7	Velocity in Z direction	29
3.8	Eye and trocar models	31
3.9	Three layers of the eyeball	32
3.10	Stress and deformation of the eyeball and the muscles	35

LIST OF FIGURES

4.1	First prototype	38
4.2	Parallel Coupled Joint Mechanism (PCJM)	39
4.3	Simple schematic of a PCJM	40
4.4	Parallel Coupled Joint Mechanism (PCJM) models	41
4.5	a: A PCJM and b: its simplified model	41
4.6	A simplified PCJM model	42
4.7	Statics analysis of PCJM	43
4.8	Serial robot and its simplified model	45
4.9	The simplified serial robot.	45
4.10	Hybrid Serial-Parallel configuration	47
4.11	The sampled workspace of the robot	49
4.12	The eye model used in the analysis.	50
4.13	Different rotations of the eye and tilt of the robot.	51
4.14	Reachability analysis at the zero position	52
4.15	Reachability analysis with 30 degrees tilt of the robot	53
4.16	Locations of the candidates with the best performance for every tilt	54
4.17	Results of the performance candidates	55
4.18	Best result for the reachability with zero degrees tilt	56
4.19	An experimental run for the best position without tilting the robot and the eye .	57
4.20	The visible and reachable areas for the best location of the eye without tilting the robot	58
6.1	Physical design and fabrication of the setup.	71
6.2	The stick-slip phase and the saw-tooth signal.	72
6.3	The stick-slip piezo actuator SmarAct SLC1750m [1].	73
6.4	Each PCJM consists of two piezo actuators.	73
6.5	The passive joint of a PCJM	74
6.6	Passive joint components	75
6.7	Physical design and fabrication of the robot.	75
6.8	The robot with mock-op second PCJM segment.	75
6.9	Tool Grippers	76
6.10	Robot configurations	76
6.11	The mounting mechanism of the robot.	77

6.12 Robot mounted on an operating table	77
7.1 The velocity of the second slider against its position	80
7.2 The result of the experiments to determine the velocities at different frequencies on 03.09.2013.	81
7.3 Frequency-to-velocity mapping for the second linear actuator.	82
7.4 The calibration procedure and the trajectory to be tracked.	83
7.5 The calibration procedure with a degenerate piezo actuator.	83
7.6 The mapping from the offset of the input device to velocity.	85
7.7 The location of \mathbf{p}_{rcm}	88
7.8 The user interface of the simulation environment.	92
7.9 The software architecture.	94
7.10 Middle ware based system architecture [2].	98
7.11 Robot controller block diagram	99
7.12 The embedded system based controller setup	100
8.1 PCJM evaluation	102
8.2 Precise motion experiments on one Euro cent coin	103
8.3 The overall setup	105
8.4 The experimental setup	106
8.5 Sequence of images from a video taken during one experiment	106
8.6 Trajectory of one experiment lasting for more than six minutes	107
8.7 The error of the RCM from raw position data of the linear actuators.	108
8.8 Comparison of the tracking error with two different velocity-to-frequency mappings.	109
9.1 Number of new patients diagnosed with RVO	112
9.2 Total number of patients suffering from RVO	113

LIST OF FIGURES

List of Tables

1.1	Advantages and disadvantages of robotic surgery	3
1.2	Comparison of two recent studies aiming towards injection into retinal vessels . .	10
2.1	Quantitative comparison of current ophthalmic robots and human surgeon	20
3.1	Positions and orientations change during vitrectomy on pig's eye	28
3.2	Properties of the eyeball	33
3.3	Four kinds of needle rotation	33
3.4	Properties of the eyeball	34
4.1	The Denavit-Hartenberg parameters (distal) for the serial robot.	46
4.2	Coordinates of the candidates with the best performance in each tilt configuration and the reference location.	53
4.3	Quantitative results of the analysis.	54
4.4	Evaluation results without tilting the robot.	57
4.5	Evaluation results with tilting the robot about 20 degrees.	58
4.6	Evaluation results for the reference.	59
6.1	The most important parameters of the SmarAct SLC1750m [1].	73

Chapter 1

Introduction

This chapter describes the general conditions of the minimally invasive surgery, it shows the usage of trocars for introducing the surgical tool to manipulate the organs and presents the conventional methods of performing intra-ocular surgery using the trocar system. Furthermore, this chapter investigates the difficulties which is caused by motor limitations of human surgeon and introduces robotics methods which can address aforementioned restrictions. Defining the problem statement of this work and the main contribution of the author to address the problem are the main parts of this chapter.

1.1 Background and Motivation

Eye surgeons around the world have to deal with everyday scenarios demanding high-precision manipulation of surgical devices. The inherent scale and fragility of the anatomy cause the retinal surgery to be an extremely difficult procedure even for the most trained and experienced surgeon.

Robots with exceptional geometric accuracy, stability and precise motion in variable scales are suitable choices for assisting surgeons to perform retinal operations under highly demanding circumstances. To date a few robotic devices exist to assist surgeons in such high-precision tasks. However, these devices have some limitations in terms of usability and integration and are not yet clinically used. Proposing an innovative robotic device working towards overcoming the current limitations is the main objective of this thesis. The main focus is the development, control and evaluation of this apparatus such that the inadequacy of prevalent devices and methods can be improved. The delicate technique of vitreo-retinal surgery can then be facili-

1. INTRODUCTION

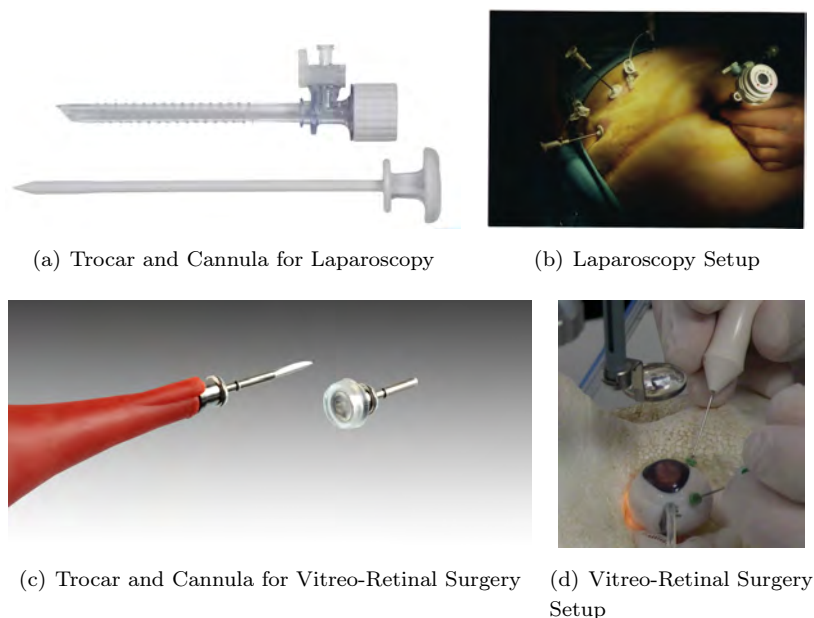


Figure 1.1: Trocar system, [a:LaproSurge-SC001, c:RetiLock-23 Ga valved]

tated, the risk of complications reduced and new perspectives for novel therapeutic strategies may become feasible.

1.1.1 Minimally Invasive Surgery (MIS)

Minimally Invasive Surgery (MIS) - also called laparoscopic surgery - refers to a surgical procedure which is performed through small incision points (usually 0.5-1.5 cm in diameter). To perform MIS, the surgeon introduces surgical tools into the patient body through holes. Usually the surgeon accesses the surgical site through three incision points: one to insert the endoscope, for intra-body visualization, and two others to introduce the surgical tools. A specialized device, called a trocar, is used as an entrance port to keep the incision point open. Trocars are sharp medical instruments which are used to locate cannula (ports) to introduce surgical instruments into body cavities such as abdominal cavity in laparoscopic surgery or vitreous cavity in ophthalmic surgery (see Figure 1.1). The benefit of the MIS over open surgery is the shorter healing time and less damage to the body surface.

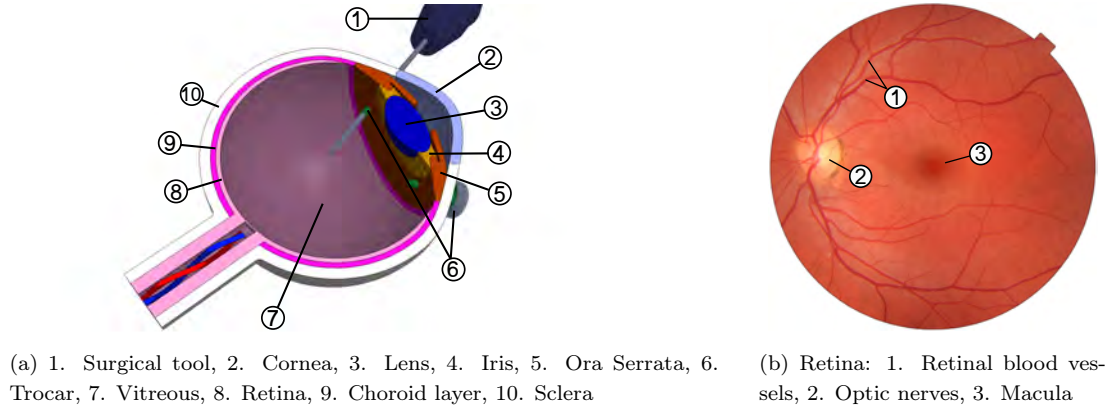


Figure 1.2: Anatomy of the Eye

1.1.2 Robotic Surgery

Since the mid-1980s, after the successful acceptance of robots for industrial applications and the exponential expansion of use in daily manual tasks, biomedical engineering scientists decided to bring robots into the health-care domain as well. The capability of robots for excellent accuracy, time-independent stability, immunity to radiations, motion/force scaling and the ability to integrate multiple input sources have made robot-assisted surgery a fast growing field. Robot-assisted surgery today is proven to be of better quality, have better time/cost effectiveness and be less invasive with more safety and precision. Furthermore, using robots in operating theaters enables real-time feedbacks and documentation. Considering all these aspects, not only have robots improved the current clinical procedures, but they have also opened the doors to new treatment possibilities [3].

Table 1.1: Advantages and disadvantages of robotic surgery [3]

Advantages	Disadvantages
Precision, Accuracy, Stability	Poor decision making/judgment
Motion Scale and tremor cancellation	Poor interpretation of qualitative data
Multitasking and Association of devices	Setup and maintenance expenses
Teleoperation, Haptic feedback	Availability and learning curve
Documentation	Failure malfunction and patient trust

1. INTRODUCTION

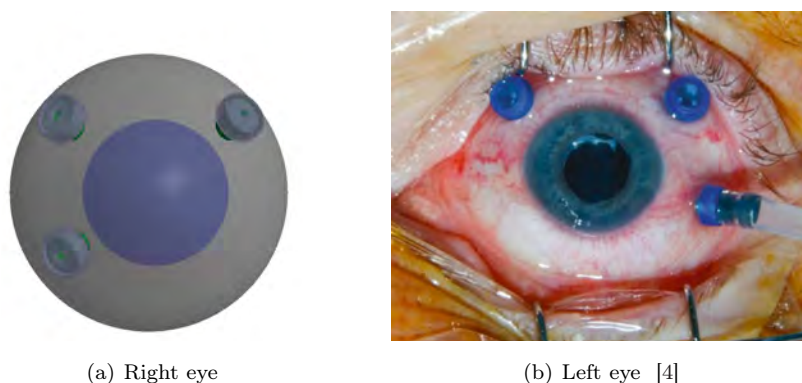


Figure 1.3: Intra-operative configuration of 3 valve cannulas - In this configuration the surgeon's position is above the figures

1.1.3 Ophthalmic Operation

Ophthalmic Operation is the term for surgical procedure which involves the eye. However the interesting eye procedures for this thesis are intra-ocular operation which is a minimally invasive micro-surgery. Intra-ocular operation consists of any procedure performed inside the eye chamber, for instance vitrectomy and vitreo-retinal surgery. In modern ophthalmic procedures, surgeons use the trocar system with the cannula to access the posterior cavity to perform intra-ocular operations. Ophthalmic operation may be performed under topical, local or general anesthesia.

1.1.4 Vitreo-Retinal Surgery

Vitreo-retinal surgery is a subgroup of intra-ocular ophthalmic surgery which deals with the treatment of diseases related to the retina, vitreous and macula, including retinal detachment, macular degeneration, diabetic retinopathy, and uveitis. Retinal and vitreous problems can cause severe loss of vision or even blindness. Ophthalmologists use specialized techniques and instruments to treat vitreo-retinal disorders. Vitreo-retinal surgery may be beneficial for these cases and, if performed in time, might prevent severe loss of vision.

Since the 1970s when the first pars plana vitrectomy was performed [5], there has been an important change in trends in ophthalmic operations, particularly in vitreo-retinal surgery. Not only have the outcomes of these surgeries been improved, but nowadays, it is also possible to find cure to previously untreatable ocular conditions. The increasing positive results in the ophthalmic surgery are mostly due to new and better developed surgical techniques, improved

low-gauge instrumentation, high-speed cutters and upgraded and enhanced visualization tools. To perform vitreo-retinal surgery, after the general pre-operational preparations for ophthalmic surgery, the surgeon sits superior to the patient's head (see Fig. 1.5 and Fig. 1.6). The operation is performed with a high magnification, 3D view through an ophthalmic microscope and he follows these steps (see Fig. 1.7):

- Using the trocar system the microcannula channels are first inserted. Usually three of them are inserted directly into the corneoscleral limbus with a distance of 3.5mm from the cornea.
- The infusion line is then connected to one of the channels. The role of this line is to maintain the intra-ocular pressure at the level selected by the surgeon [4].
- The illumination pipe is introduced through the other channel
- The remaining channel is used as manipulation channel which is utilized to insert micro-surgical tools (e.g. vitrectomy cutter, microforceps)

Then, using the microscope to see the illuminated parts of the eye chamber through the cornea, the surgeon performs the desired operation (see Fig. 1.6).

1.1.5 Retinal Vein Occlusion

Retinal Vein Occlusion (RVO) is an ophthalmic disease with a promising treatment option which currently, due to physiological limitations, is not possible for human surgeons to perform. RVO is one of the most common reasons for blindness and it occurs when a vein or

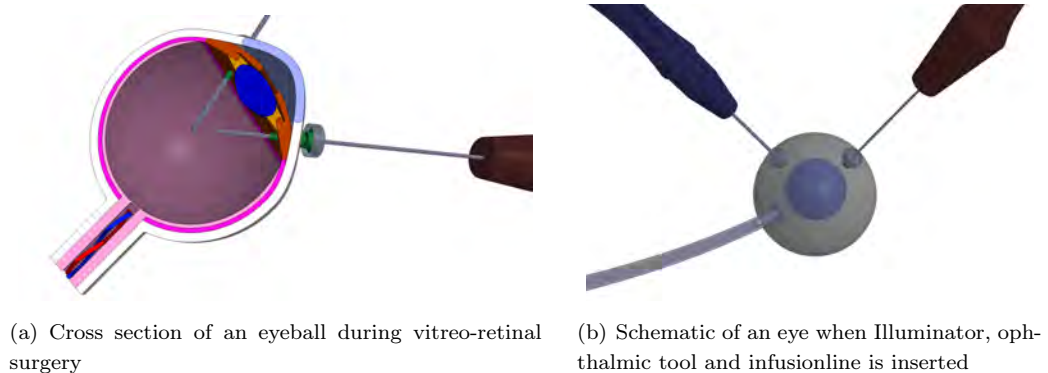


Figure 1.4: Minimally invasive ophthalmic surgery setup

1. INTRODUCTION

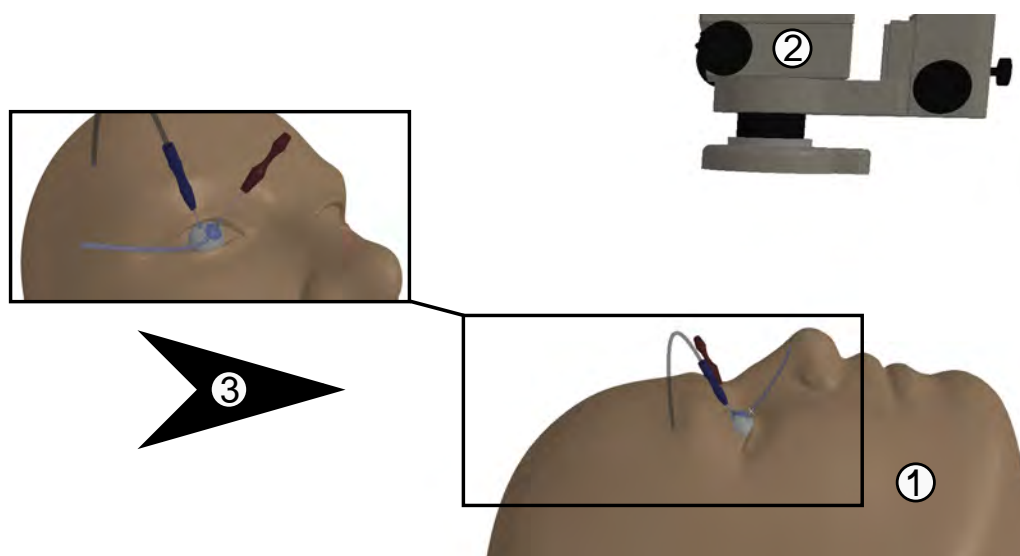


Figure 1.5: vitreo-retinal Surgery setup: 1. Patient, 2. Ophthalmic Microscope, 3. Surgeon's Position in an ophthalmic operation

artery supplying the retina is blocked due to a clot. Blood flow to the photoreceptor cells is therefore restricted and there is a lack of drainage. Untreated, this condition can lead to irreversible vision loss and even blindness. Usually a blockage is caused by diabetes, which damages small blood vessels. The formation of a thrombus (a blood clot) is in most cases the cause of a blockage. Currently over 16 Million people worldwide (with 2% annual growth rate) are suffering from this disease and at present, there is no effective treatment [6]. When RVO occurs, the focus usually lies on controlling bleeding and swelling of the affected area [7]. A more effective treatment is the breakdown of the blocking thrombus and restoration of blood flow. To solve blood clots in vessels, thrombolytic drugs are administered. Thrombolytics, also called fibrinolytics, include recombinant tissue plasminogen activator (rt-PA), a drug that is also commonly used for strokes. For RVO, systemic administration of thrombolytic agents has the downside of yielding high risks of complications such as bleeding [7]. These risks can be avoided by applying lower doses of rt-PA closer to the thrombus. Studies showed that injecting rt-PA in the vitreous, the gel between the lens and the retina, is effective but may be toxic to the retina [8]. To overcome these limitations, techniques are being developed to directly inject thrombolytics into the retinal vessels. Such local application is highly effective and could remove the underlying cause of vision loss by restoring perfusion of the retina. This procedure is called Retinal Endovascular Fibrinolysis (REF) [8]. Although the effect of this method is experimen-

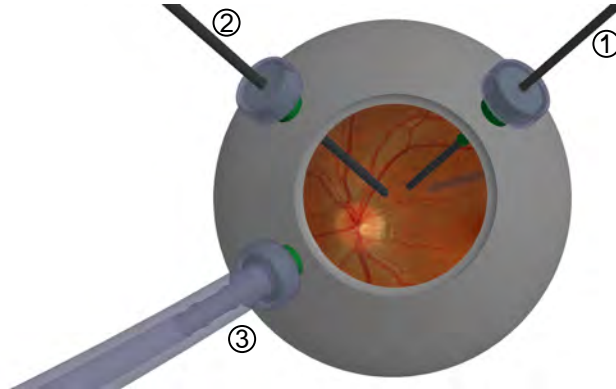


Figure 1.6: What surgeon sees through ophthalmic microscope during vitreo-retinal surgery: 1. Surgical tool, 2. Illuminator, 3. Infusion line

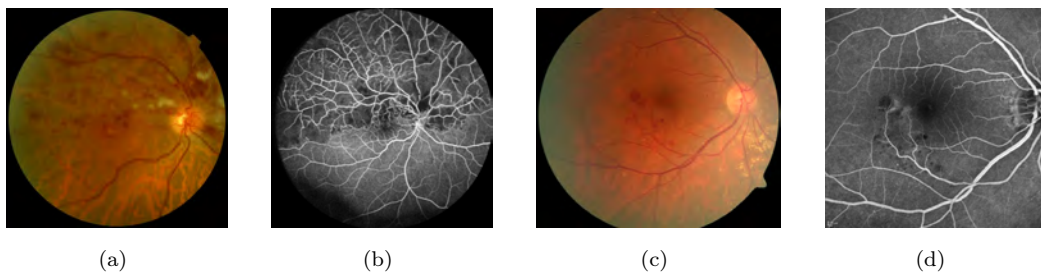


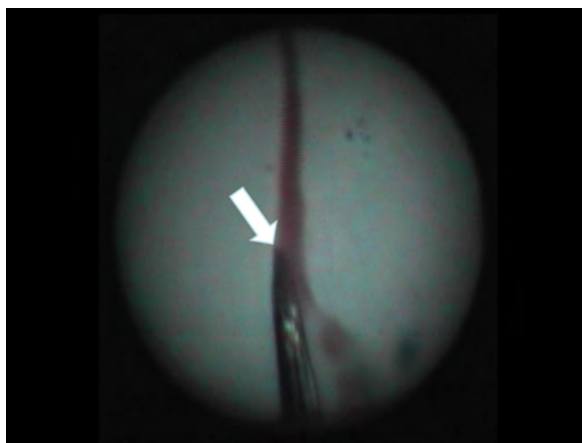
Figure 1.7: Retinal images: occluded retinal vessels is seen here

tally proven, unfortunately this injection can not be performed by human surgeons. Although the method of REF seems promising, it is not yet used in clinical routine. This is because, with present-day approaches, it is likely that complications would occur throughout the surgery [7]. Cannulation of retinal vessels is especially challenging, even for experienced surgeons for several reasons. Retinal vessels are very small and delicate; to puncture structures only $50 - 400 \mu m$ in diameter [9], human precision is hardly sufficient. In particular surrounding retinal tissue should not be damaged [6]. This requires a very steady hand surgeon and high endurance, otherwise permanent damage to the retina may result. Another challenge is the estimation of force needed to push the needle through the vessel wall. This is because these forces are so small that the surgeon can not rely on haptic feedback any more [9]. In order to help deal with these limitations, good visual feedback has to be provided. Common operating microscopes provide insufficient magnification and only a fixed viewing point. New technical developments make it possible to use smaller devices and at the same time get a better visualization. On the other hand, common surgical instruments for cannulation are too large [7]. The diameter of

1. INTRODUCTION



(a) Curved glass micropipette with beveled tip [8]



(b) View through the endoscope on the catheter, that is aligned with a branch retinal vein. The arrow marks the tip of the catheter [7]

Figure 1.8: Retinal vein cannulation approaches

retinal vessels depends where on the retina they are located. The optic disc is the retinal area where the optic nerves and the blood vessels enter the eye. Therefore the vessels entering the eye are called Central Retinal Vessels. As the distance to the optic disc increases, the diameters of the vessels decrease. At the same time the risk of the retina being detached rises, because it is less tightly adhered. Those small veins and arteries are named Branch Retinal Vessels. A distinction is made between Central Retinal Vessel Occlusion (CRVO) and branch retinal vessel occlusion (BRVO) [7]. An occlusion of a branch retinal vessel only affects a part of the retina, whereas a blockage of the central retinal vein or artery is more serious. The size of the injection device is a challenge particularly when dealing with BRVO. Microneedles with very small diameter are therefore needed. Finally, as for all new medical procedures, there is a need for objective criteria determining the success of the surgery. Clinical trials depend on methods for evaluation to show the superiority of this approach in comparison to conservative treatment. There are a few suggestions for how to show that reperfusion was successfully accomplished. Finding a way to increase the precision of the surgeon's motion enables the treatment of RVO.

1.1.6 Retinal Vessel Cannulation Approaches

The surgery in which clot-solving drugs are directly injected in the retinal vessels includes a procedure named sclerotomy. It involves placing surgical instruments through one or more ports in the sclera, the white of the eye. By entering the eye through such a port and advancing

further through the vitreous, the retina can be reached. Because of the thin structures that retinal vessels present, the size of the tool puncturing the vessel is crucial. In the following, two studies are presented which suggest different procedures for the application of fibrinolytics for RVO. The first paper focuses on feasibility and evaluation of retinal endovascular fibrinolysis (REF). In the second, a study by Hattenbach et al. [7], a new tool improving visual feedback is introduced. In a test by Pournaras et al. [8] surgery was performed on several anesthetized pigs. An artificial blockage of a retinal vein was achieved by local application of drugs and exposing the veins to a laser beam. The microinjection of the thrombolytic drug was done manually and under an operating microscope. Therefore a glass micropipette for entering the vein and subsequent injection was specifically designed and produced. Its tip has a diameter of $30\ \mu\text{m}$ and is beveled (see Fig. 1.8). The micropipette was used to puncture the vein by hand. At a bifurcation directly before the thrombus 2ml of thrombolytics were injected. For the control test, balanced salt solution was injected in one eye. Afterwards the eyes were removed and the results were evaluated histologically. A technically more sophisticated approach is proposed by Hattenbach et al. [7]. In their study they focus on better visualization to help the surgeon targeting the vessel. This is achieved by attaching an endoscope directly on a catheter. The endoscope is a gradient index endoscope developed for eye surgery which has a high resolution. Its fiber-optic end is attached onto a glass sleeve, on which the catheter is mounted. The catheter is made out of quartz-glass and is coated in polyamide. The tip of the catheter is angled in order to reach into the field of view optimally. Its diameter is only 10 to $20\ \mu\text{m}$ and is sharpened at the end. To minimize the possibility of leakage, a single piece system was designed. This is because high pressure is needed for the injection through small catheters. In contrast to the study by Pournaras et al. the procedure was not done in vivo but on eyes removed from pig cadavers. In addition they did not artificially induce a vessel occlusion, so no blockage was present. During the surgery visual feedback was being provided by both an operating microscope and the endoscope on the catheter system. The catheter was oriented manually to be parallel to the retinal vein or artery. The targeted site of injection and the end of the catheter in view, the vessel wall was pierced. Besides the injection of rt-PA, hypertonic solution (hyper-HES) and salt solution were used.

1. INTRODUCTION

Table 1.2: Comparison of two recent studies aiming towards injection into retinal vessels

Pournaras et al. [8]	Hattenbach et al. [7]
Size of microneedle tip	
30 μm	10 - 20 μm
Test objects	
12 eyes of 12 minipigs	11 enucleated eyes of pigs
Number of injections performed	
12 injections	25 injections
Injected liquids	
rt-PA in 11 eyes and BSS in one control eye	rt-PA in 3 eyes, hyper-HES in 3 and BSS in 5 of the eyes
Time of needle held inside vessel	
30 s	1-5 min
Location of punctured vessels	
Major veins near optic disc	1-15 disc diameters away from optic disc

1.1.7 Difficulties for the Human Surgeons

The inherent scale and fragility of the anatomy make the retinal surgery a prohibitively difficult procedure for human surgeons. Due to physiological dexterity limitations, the surgeon's movement skills are not sufficient enough to perform tasks such as accurately manipulating the microsurgical tools. The needed precision for some of the procedures is less than 10 μm while the best recorded precision of the human surgeons is around 100 μm [10] which would decrease dramatically by time/fatigue. The dexterity limitations of the human surgeons make intra-ocular ophthalmic operations hard to perform and even impossible in some cases. Although the concept of some retinal disease treatments have been proved in the laboratory, due to the aforementioned difficulties the clinical realization of these concepts is not feasible by human surgeons.

Another limitation of human surgeons relating to ophthalmic surgery is the lack of intra-ocular perception. Precise estimation of the tooltip distance from the surface of the retina and observing the intraocular forces is not possible. This information can help to increase the quality and decrease the risk of the surgery.

1.1.8 Robotic Ophthalmic Surgery

Robots with exceptional geometric accuracy, stability and precise motion in variable scales and conditions are suitable choices for assisting ophthalmic surgeons to perform retinal surgeries under highly demanding circumstances. There are several factors which make the robots suitable assistants for ophthalmic surgeons. Robots will upskill the surgeons by increasing the precision of surgeon's manipulation and remove the physiological tremor. Virtual fixture capabilities and integration of various input/output sources are another benefit of using robots as a ophthalmic surgery assistant. In general using a functional robot in the ophthalmic operating room will upskill surgeons, increases the operation safety and decreases the operation time. All these factors will add value to the surgery towards solving the current operational difficulties and establish new avenues for the development of novel treatments.

1.2 Problem Statement

Upskilling the human surgeons for performing vitreo-retinal operation is the main objective of this work. To realize this objective a robotic solution is proposed. The design and development of a robotic setup which assists the surgeon to perform sophisticated intraocular ophthalmic operations is described in this thesis.

1.3 Contribution

The contribution of this work is the design and development of a novel hybrid parallel-serial micromanipulator which is designed to assist surgeons for performing vitreo-retinal surgery. This mechanism addresses key unsolved questions such as integration into clinical environments, compactness, environmental vibrations. The proposed mechanism has given this micro-manipulator a better intuition for ophthalmic operations in comparison to the state of the art.

1.4 Outline

The remainder of this thesis is organized as follows: Chapter 2 introduces the state of the art in the domain of medical robotics and specifically describes robots for assisting ophthalmic surgery. It also describes the limitations of the current setups and discusses the motivation of this work. The methods for defining the requirements of the end-user in this project are described in chapter 3 which includes the tracking of the surgeons' motion and the modeling

1. INTRODUCTION

of the eye. Chapter 4 introduces the proposed kinematics of the robot with its analysis and evaluations; this is where the different prototypes are shown. The dynamic analysis of the robot is described in chapter 5, which is followed by physical design and fabrication of the robot as well as the mounting mechanism, based on the requirements presented in the previous chapters. Chapter 7 presents the robot controller together with software architecture implementation. The experimental setup, experiment design and performance of several non-clinical and clinical experiments are described in chapter 8. Chapter 9 briefly discusses the bench to bedside translation and technology transfer strategies for such a medical robot. The conclusions of this thesis and opportunities for further work are presented in chapter 10.

Chapter 2

Literature Review

This chapter presents the current methods which are aiming to address the previously mentioned problem statement. Here, surgical robotic research groups and ophthalmic researchers with this objective are mentioned. Comparison of the technologies, description of the limitations and the approach of this work to break through these limitations are also included in this chapter.

2.1 Robotic Devices in Surgical Application

Most of the early surgical robots were modified industrial manipulators such as [11]. In 1985 the first robot assisted surgery was performed using a modified industrial robot, Puma 560. The setup was used to define the trajectory of a brain biopsy [12]. Since then, numerous robotic setups specialized for surgical applications have been developed. Specifically advancement in minimally invasive surgery has been a catalyst to speed up the surgical robotic field expansion. Minimally invasive surgery offers lots of benefits for surgeons, hospitals and patients, and using robots adds significant values to this operations [13]. The most frequently used surgical robot for minimally invasive operations today is the da Vinci¹ surgical system. To include human decision making in the robotic operations, surgeons are closing the control loop by one of the following ways:

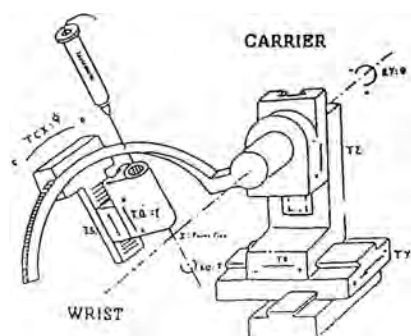
Teleoperator control: where the motion of the surgeon is applied using an input device and the robot moves accordingly.

Cooperative control: where both the surgeon and the robot are grasping the surgical tool simultaneously. In cooperative control, the role of the robot is to overcome human surgeon's limitations, usually a force sensor is used to detect and assist the desired surgeon motion.

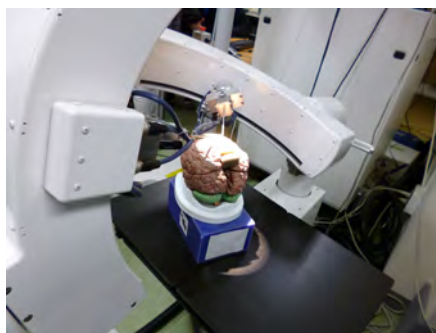
¹Intuitive Surgical, Mountain View, CA, USA

2. LITERATURE REVIEW

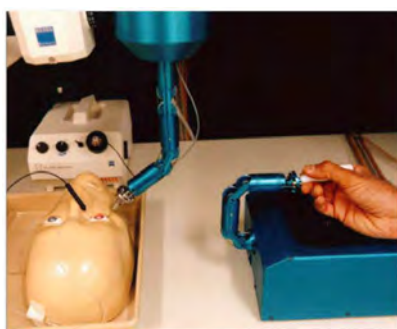
2.2 Robots for Assisting Ophthalmic Surgery



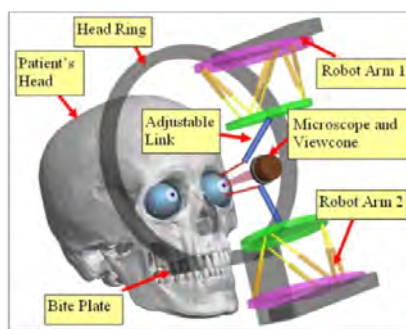
(a) Stereotaxical Micro-telemanipulator for Ocular Surgery (S.M.O.S) [14]



(b) Ophthalmic setup designed at Tokyo University



(c) Ophthalmic setup designed at jet portion lab [15]



(d) Ophthalmic setup designed at Columbia University [16]

Figure 2.1: Robots developed for ophthalmic surgery

There are currently no robotic systems used for clinical ophthalmic therapy. However, various developed systems have been trialled in the laboratory to perform animal and cadaver eye experiments. Moreover, many of these systems have shown some success in performing specific ophthalmic procedures like external ocular surgery and anterior segment surgery, but none of them have been proven 100% reliable in posterior segment surgery. As a consequence, there is no ocular surgical robotic system available in the market yet, despite the intensive research.

Fragility of the eye anatomy and the necessary precision for ophthalmic surgery have made this medical field an attractive area for robotic scientists. Robots are a promising tool to overcome the ophthalmologists' limitations. They bring high geometric accuracy and stability at variable scale and, if designed properly, they will help to alleviate the surgeon's fatigue and stress from the surgical site.

2.2 Robots for Assisting Ophthalmic Surgery

The earliest robotic setup to assist eye surgeons was developed in 1981 (see Figure 2.1). It was a Stereotaxical Microtelemanipulator for Ocular Surgery (S.M.O.S) based on a Remote Center of Motion (RCM) mechanism. This four Degrees Of Freedom (DOF) mechanism pivots the tool around the RCM point [14]. Since the late 1980s several research groups have introduced robotic setups for application in ophthalmic surgery. These groups were interested in procedures such as retinal vessel cannulation [17], drainage device implantation [18], intra-vascular drug delivery and micro-vascular pressure measurement [19].

A research team from Tokyo University was one of the first groups to develop a prototype for robot assisted ophthalmic surgery based on S.M.O.S kinematics. In this project Japanese engineers, working together with ophthalmic surgeons and neurosurgeons, developed a master/slave prototype to address the present limitations of vitreoretinal surgery. The master device and slave device are placed in different workstations, and commands from the input device are given to the slave through a real-time computer every $10ms$ via local area network. The movements of the input are performed by the slave robot with a scaling factor of 40:1. It is possible to attach several existing surgical micromanipulators to the tip of the slave robot. The manipulator has 5 DOF which consist of three translational movements in the x, y and z directions; one rotation around the instrument axis and a gripping/releasing and a cutting movement. It is constructed with a pair of spherical guides allowing the x-axis and y-axis planar motion as well the ability to move the end effector position up and down along the axis of the surgical tool. The setup was used in successful ophthalmic procedures such as posterior vitreous detachment, retinal vessel sheathotomy using 25-gauge microscissors, and microcannulation of retinal vessels with a diameter of 100 microns in porcine eye [20, 21, 22]. Currently this setup is modified to be used for brain surgery (see Figure 2.1).

In 1997 the researchers from Jet Propulsion Lab (JPL) at California Institute of Technology together with the National Aeronautics and Space Administration (NASA) introduced an ophthalmic 6DOF telemanipulator with the precision of 10 microns [15]. This was the first ophthalmic robot with force sensing which was reflected from the slave robot to the master device to enhance the sense of touch. The JPL ophthalmic robot prototype has been used to demonstrate single-arm simulated eye microsurgical tasks and dual-arm micro-suturing procedures. Virtual reality applications of this setup include using the input device as a haptic interface and in the use of virtual augmentation to the real-word feedback to improve operator

2. LITERATURE REVIEW

performance.

A novel theoretical hybrid two-armed micro-surgical slave robot equipped with intra-ocular dexterity devices was designed and simulated by Columbia University. They introduced a mounting method using a bite plate to fix the robot with respect to the patient's head. The interesting feature introduced in this work was the 16-DOF precise manipulation of the tool inside the eye whilst manipulating and stabilizing the eye itself under the microscope [16, 23, 24].

Intraocular Robotic Interventional and Surgical System (IRISS) is another RCM mechanism which was designed by University of California, Los Angeles. It consists of a mechanical RCM configuration which can be mounted onto the head of the patient. The setup focused mainly on lens capsulorhexis in cataract surgery, 23-gauge vitrectomy and retinal vein microcannulation [25].

A research group from the Netherlands, TU Eindhoven, is another active group that developed a RCM mechanism for ophthalmic surgery. In their setup two slave robots are mounted on an operation table (see figure 2.3), these robots are controlled using a customized master console [26]. The surgeon sits at the master module adjacent to the patients bed. This module comprises of the master devices and a stereo monitor from which the surgeon can presumably observe the images of the eye acquired by the microscope. The set-up of the system can be seen in Figure 2.2¹. Each slave device consists of two main parts: the instrument manipulators and their passive support system (see Figure 2.3). The instrument manipulators are designed in such a way that they are able to move with 4 DOF, the three rotational movement and one translational movement required in vitreoretinal surgery, when a kinematically defined RCM is set. Moreover, the instrument manipulators are equipped with an on board instrument-changing system, where instruments are stored and changed when needed. The manipulators are designed with high stiffness, they are backlash-free and exhibit low friction. The forces on the instrument is measured to supply force feedback to the surgeon via haptic interfaces. The master devices are 5 DOF serial kinematic devices. Two revolute actuated joints are mounted in series, allowing for two swing movements. In a second improved prototype, these actuators will be mounted in parallel to reduce inertia. In series to them, a parallel layout is used to provide twist motion and translational motion along the instrument axis. At the end of the link, there

¹<http://www.preceyes.nl/>

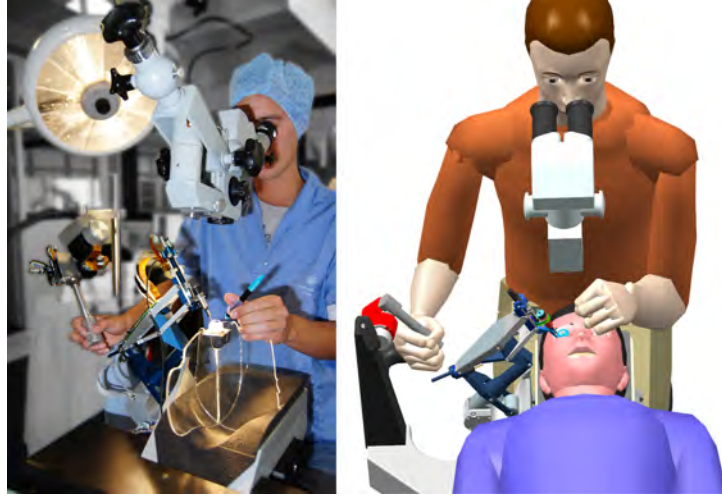


Figure 2.2: Preceyes robotic setup designed and developed at TU Eindhoven

is a button which is used to operate the gripper in the slave part. The scaled haptic feedback is delivered to this button. Moreover, the motion effects by the surgeon is provided to the slave devices tremor free and scaled down. When the surgeon operates the master device, it is so configured, that the surgeon feels as if they are grasping the surgical instrument near its tip, inside the eye. The EyeRaHS device is however quite bulky. This can present a problem when integrating it into the OR. A surgical robot is not needed in every ocular surgery intervention, therefore it is desirable that the robot does not occupy a static place in the OR, which would be the case with the EyeRaHS Robot.

All the setups mentioned above are listed in the category of master-slave robotics setups, where the surgeon is moving the surgical tool, attached to the end effector of the robot, by means of an input interface. The robots in this category are also called telemanipulators. The other category of the surgical robotics setups are robots with cooperative based controller, where both the robot and surgeon are sharing the surgical tool. Usually in this modality the robot predicts the surgeon motion by using force/torque sensors and after cancellation of the physiological tremor it helps the surgeon to move the surgical tool precisely. Steady-Hand Eye robot and Micron are cooperative robots designed to assist ophthalmic surgery.

The Steady-Hand Eye Robot project was started in the late 90's at Johns Hopkins University. Steady-Hand is a cooperatively-controlled robot assistant designed for retinal microsurgery. Co-

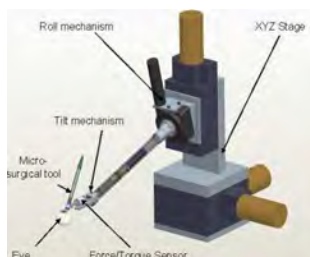
2. LITERATURE REVIEW



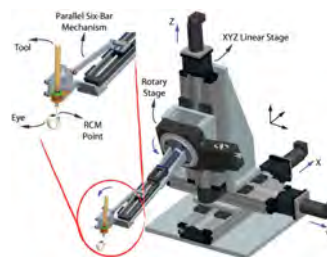
Figure 2.3: RCM mechanism designed and developed at Technical University of Eindhoven, Netherlands



(a) First version of the robot was published in 2000 [27]



(b) Modified robot which was published in 2007 [28]



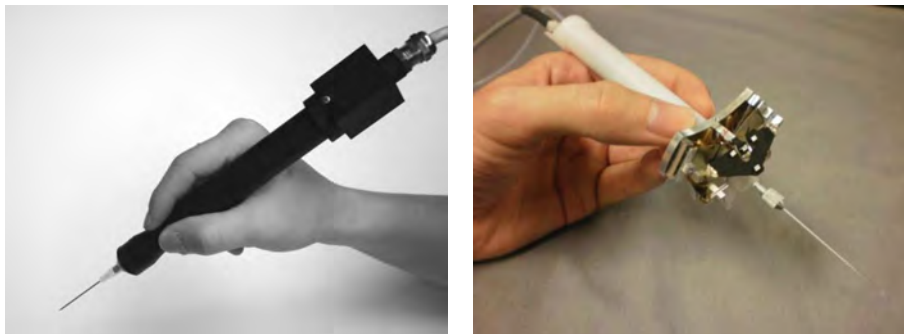
(c) Latest version which was published in 2010 [29]

Figure 2.4: Steady-Hand Eye Robot, Designed and developed at Johns Hopkins University

operative control allows the surgeon to have full control of the robot, with his hand movements dictating the movements of the robot exactly. The robot is able to move with five DOF, three translations for the positioning of the tool when about to be inserted and the two rotations needed during the phase of vitreoretinal surgery, when the tool is already inside the eye. The manipulator consists of four modular parts. The base of the robot is a X - Y - Z linear stage for translation. Attached to the base there is a rotary stage for rolling movements. Tilting movements are possible thanks to a parallel six-bar linkage attached to the rotational joint. At the end effector of the robot, there is a tool adapter with a handle force sensor. Thanks to this force sensor, the forces that the surgeon exerts when moving the tool are measured and the robot is able to accompany this movement tremor free and with higher precision than the

2.2 Robots for Assisting Ophthalmic Surgery

surgeon's hand could have alone. The robot can also be a valuable assistant during high-risk procedures, by incorporating virtual fixtures to help protect the patient, and by eliminating physiological tremor in the surgeon's hand during surgery. Two versions of the Steady-Hand Eye robot is developed so far, the precision and the stiffness is improved in new version and its more intuitive for the surgeons to control. By integrating force sensors on the surgical tool shaft the surgeon have a better intraocular perception while operating with the Steady-Hand Eye robot [27, 28, 29, 30, 31, 32, 33, 34, 35, 36].



(a) Micron Hand-held instrument published in 2004 [37]

(b) Micron Hand-held instrument published in 2010 [38]

Figure 2.5: Micron Hand-held instrument designed and developed by Carnegie Mellon University

Micron is another cooperatively controlled robot for ophthalmic surgery which was first described in a publication in 2000. It is a hand-held microsurgical instrument which is designed to actively detect and cancel human physiological tremor and other unwanted movement during vitreo-retinal microsurgery [39]. The compact instrument was designed based on piezo actuation technology [40] and Micro Electro Mechanical Systems (MEMS) technology [41]. In principle the Micron hand-held instrument senses the motion of the surgeon using the integrated accelerometer and vision based methods [42, 43], filters the physiological tremor and unwanted motion [44, 45, 46, 47, 48] and generates the accurate, filtered motion [37, 49, 50, 51, 52, 53, 54, 55, 56]. The performance of the Micron hand-held instrument is evaluated using image processing techniques [57, 58, 59] and it is utilized in Retinal Vein Cannulation [60], Laser retinal surgery, semiautomated intraocular laser surgery [61] and even cell manipulation experiments [38].

2. LITERATURE REVIEW

Table 2.1: Quantitative comparison of current ophthalmic robots and human surgeon

	Preceyes [62]	Steady-Hand [29]	Micron [47]	Surgeon
Precision (μm)	~ 10	~ 10	~ 5	~ 108
Workspace (mm)	$50 \times 50 \times 50$	$100 \times 100 \times 100$	$1 \times 1 \times 0.5$	N/A
Virtual Fixture	Fixed	Yes	Limited	No
Motion Scale	Yes	No	No	No
Robot Weight (g)	890	> 15000	170	N/A
Setup Weight (g)	~ 8000	> 15000	170	N/A
Force feedback	No	Yes	No	No

A different and conceptual robotic approach for ophthalmic surgery assistance was integration of a micro robot or a Hexapod surgical system (HSS) to Da Vinci macro robot. The precision and dexterity of this approach was validated by introduction of a vitrectome in a porcine eye.

2.3 Limitations of Current Setups

Table. 2.1 shows the quantitative comparison of the current setups including human surgeons for vitreo-retinal micromanipulation. Although all robotic groups achieved valuable results, none of the systems are clinically compatible and thus they have not been successfully commercialized, this is due to the fact that the setups are not intuitive for the operation room crew; either these setups are bulky or they miss at least one key feature which make them hard to be integrated into conventional clinical area.

2.4 Motivation

Taking both the state of the art and the actual clinical requirements into consideration was the initial stage for proposing a novel approach in robot assisted eye surgery. The idea of this work originated from the Ophthalmology Department of the Klinikum Rechts der Isar, Munich and based on a clinical need to find a way to upskill the surgeon for performing precise intra-ocular micro-manipulation such as retinal vein cannulation. Having such a device will not only help surgeons cure diseases which were previously intreatable but will also enable the realization of future technologies like retinal chip implantation.

Chapter 3

Clinical Studies and Requirement Analysis

In order to design a clinically functional, compact and precise robotic device for medical applications one of the most important initial steps is defining the realistic requirements. Before taking design steps, the actual clinical requirements for patient, surgeons and hospitals should be carefully analyzed. In this section the requirement analysis methods for ophthalmic surgery are discussed. The first part is a tracking method for clinical motion observation and the second part is a method to model the anatomy of the eye to define the ophthalmic characteristics.

3.1 Tracking Surgical Motion

To reproduce a clinical robotic motion of the surgical tool equivalent to the hand of the surgeons, an understanding of the surgeon's motion during the ophthalmic procedures is needed [10, 63, 64, 65, 66, 67]. Hence, in this work a clinical tracking setup was used to record the surgeon's motion while he was operating. The outcome of this series of experiments was a data set containing the positions, orientations, velocities, accelerations and the working volume information.

3.1.1 Background

Optical Tracking (OT) and Electromagnetic Tracking (EMT) are the most famous tracking methods for clinical hand or tool motion. In OT, rigid optical markers are attached to the tool or onto the surgeon's glove, and precise 3D position and orientation of the markers are recorded by multiple cameras. In EMT, an electromagnetic field generator is used near the surgical site and the relative 3D position and orientation of a sensor, which is attached to the tool or glove,

3. CLINICAL STUDIES AND REQUIREMENT ANALYSIS

are observed with respect to the transmitter frame. Although the precision of OT is better than EMT, continuous visibility of the markers needs to be maintained during the procedure, i.e. occlusion must be avoided. Furthermore, the optical markers are not as small as EMT sensors, so the weight and length added to the tool are not negligible. Consequently, the motions during procedures which have limited movements with limited forces, such as in vitreo-retinal surgery, completely change in the presence of current OT markers. Thus, a promising alternative method for vitreo-retinal surgical tool tracking is EMT, where the visibility of the sensors is not a factor, and the sensor's weight and size are negligible [68]. In this work an electromagnetic tracking system is used to record the motion of the surgeon during a real vitreo-retinal operation. The result of this work is a complete motion analysis of vitreo-retinal surgical tool in 6 DOF. Since the complete tracking data with relevant analysis during ophthalmology has not been collected before, this data is later used to optimize the design of a medical assisted device for vitreo-retinal surgery and simplify the trade-off between compactness and performance for engineers. The clinical data observed here will substitute the assumptions which are currently used in robotic designs and also serve as a toolkit for the validation phase. This clinical data consists of working volume, tool position, tool orientation, angular and linear velocities, accelerations, trajectories and the emergency reaction of the surgeon. In the design phase, which will be described in the next chapters, this data is useful for choosing suitable actuators and in the validation phase it is used as a reference for system behavior.

3.1.2 Methodology and Experiments

Tracking System: To simulate the clinical environment as realistically as possible, the experiments were set up in a surgeons' training room at the Klinikum Rechts der Isar¹. Here the training is performed on a training table with a pig's eye, which is geometrically similar to human eye. In fact, this setup is exactly like an operation on a human eye. The tracking system of this work comprises an electromagnetic tracking system, a "3D Guidance microBird" (Ascension Technology, USA) with mid-range transmitter and model 180 sensors². This system captures motion with 0.8 mm and 0.5 degrees precision which is acceptable for the objective of this study. The optimal tracking volume for this combination (from the transmitter center, as seen in Figure 3.1) is:

- $X = 20$ to $51cm$

¹<http://www.augenklinik.med.tum.de/>

²<http://www.ascension-tech.com/>

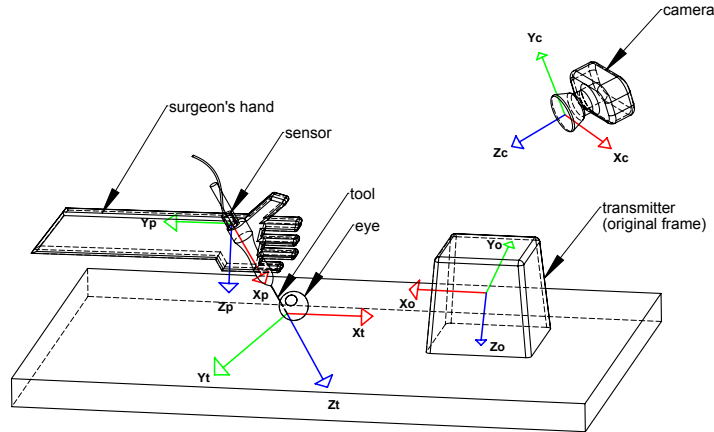


Figure 3.1: Coordinate frames for the experimental setup, transmitter coordinate frame is used as the original coordinate frame for sensor and camera [68]

- $Y = \pm 23cm$
- $Z = \pm 15cm$

The transmitter was placed on the table close to the patient's head in the optimal tracking area (see Figure 3.2). As shown in Figure 3.2 the sensor placed on the instrument did not interfere with the handling, and the movement by the surgeon was not affected in any direction. In order to maintain optimum tracking accuracy a non-metallic table was used. The DC EM tracking system is theoretically susceptible to metals with high magnetic permeability [69], but in our application such effects were minimized, by removing the metallic objects from the operation site as far as possible. In order to have visual supervision over the experiments a 1.3 megapixel camera was integrated into the tracking setup in an appropriate location, so as to cover the surgical area (see Figure 3.2). The purpose of combining the information observed from the electromagnetic system and the images taken by camera was to improve the tracking procedure, which will later be used as feedback for data validation and a suitable way of motion visualization. First, the complete hardware setup, including placement of the camera and the transmitter in suitable locations, was prepared. In the next step an expert surgeon prepared the pig's eye for operation, followed by the procedures consisting of the adjustment of the microscope, inserting the trocars (a 23 Gauge trocar system was used) and connecting the infusion line. Then he was asked to perform an operation while the tracking software was running. The tracking software developed for this study gathers the information of the position (X, Y, Z in millimeter) and orientation (Azimuth (A), Elevation (E), and Roll (R) in degrees),

3. CLINICAL STUDIES AND REQUIREMENT ANALYSIS

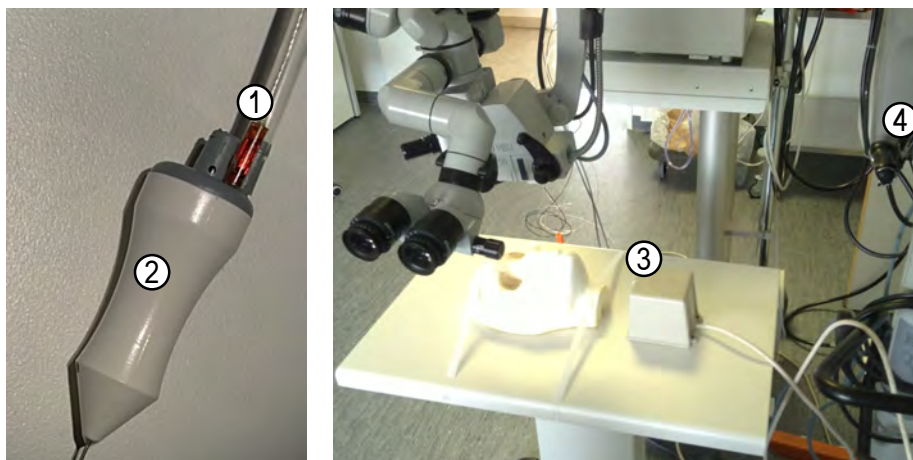


Figure 3.2: Tracking setup: 1. EMT sensor, 2. Surgical tool, 3. EMT transmitter, 4. Camera

adds data from timestamp, and saves all information continuously in a file during the procedure.

At each time stamp the data contains:

- An ID for each piece of data point. The image captured by the camera for each data has the same ID for further references.
- X , Y and Z in millimeters, representing the relative position of sensor with respect to the transmitter frame shown in Figure 3.1.
- A , E and R in degrees, representing the relative orientation of sensor with respect to the transmitter frame shown in Figure 3.1 in degrees.
- A time stamp in seconds, representing when the data was captured.

In this study the exact position of the EMT sensor in 6 DOF was desired, however, one would be able to analyze any point along the medical tool (e.g. tool tip) by simple homogeneous transformation.

Augmented Reality: In order to complete the interaction loop during surgery and to have visual feedback during the procedure, a camera was added to our tracking system. The camera was calibrated to project a 3D point (sensor position and orientation), which is known with respect to EMT transmitter shown in Figure 3.2. By setting the transmitter frame as the original frame for EMT system and the camera, the position and the orientation of the sensor

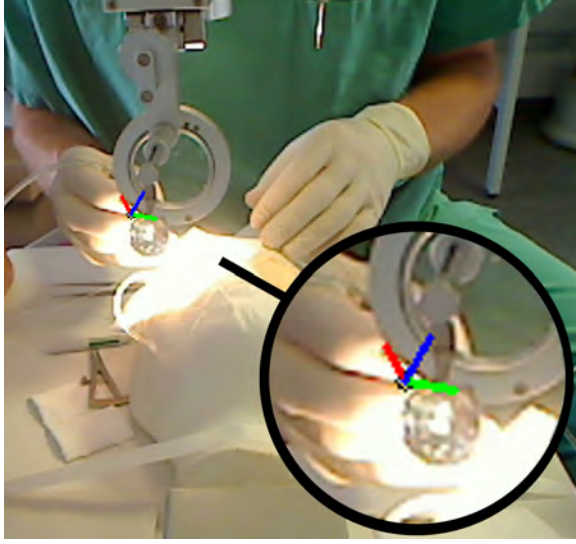


Figure 3.3: In each captured frame the position of sensor is marked with a black dot and the orientation of the sensor is represented by a coordinate frame

could be projected onto the image. The projection was performed as follows. The projection matrix P was defined as:

$$P = \begin{array}{c} \text{intrinsic} \\ \left[\begin{array}{cccc} f_x & 0 & c_x & 0 \\ 0 & f_y & c_y & 0 \\ 0 & 0 & 1 & 0 \end{array} \right] \end{array} \begin{array}{c} \text{extrinsic} \\ \left[\begin{array}{cccc} R_{1,1} & R_{1,2} & R_{1,3} & t_x \\ R_{2,1} & R_{2,2} & R_{2,3} & t_y \\ R_{3,1} & R_{3,2} & R_{3,3} & t_z \\ 0 & 0 & 0 & 1 \end{array} \right] \end{array} \quad (3.1)$$

The P is a 3 by 4 matrix defined by multiplication of the intrinsic matrix by the extrinsic matrix. The intrinsic matrix represents the intrinsic camera parameters, which depend only on camera characteristics such as focal length f , pixel size and principal points. The extrinsic matrix encodes the current position and orientation of the camera and defines the rotation matrix and translation vector of camera with respect to a known frame, in this case, this EMT transmitter center frame. Both intrinsic and extrinsic matrices were extracted by a camera calibration procedure using a calibration pattern with known 3D geometry [70]. Next, in order to project the 3D position of the sensor into the current image, the following computation was used:

$$\begin{bmatrix} x_c \\ y_c \\ 1 \end{bmatrix} = P \begin{bmatrix} x_p \\ y_p \\ z_p \\ 1 \end{bmatrix} \quad (3.2)$$

3. CLINICAL STUDIES AND REQUIREMENT ANALYSIS

where x_c and y_c are pixel coordinates and define the position of the sensor on each image. To project the orientation of the sensor, the rotation matrix was used to visualize the coordinate frame of the sensor on each frame with respect to its relevant A , E and R angles. In order to track all the orientations without singularities, the quaternion based rotation representation was used. To project coordinate frames of the sensor on the image the following technique was implemented:

$$\overbrace{\begin{bmatrix} x_x & x_y & x_z \\ y_x & y_y & y_z \\ z_x & z_y & z_z \end{bmatrix}}^{X_{axis}|Y_{axis}|Z_{axis}} = R \begin{bmatrix} d & 0 & 0 \\ 0 & d & 0 \\ 0 & 0 & d \end{bmatrix} \quad (3.3)$$

where d is the length of the axis (in pixels), which will be presented on the image. From the projection of X_{axis} , Y_{axis} and Z_{axis} and by connecting this point to the center point, positions and orientations of the sensor connected to the surgical tool were visualized. In Figure 3.3 a frame captured during the procedure is presented.

3.1.3 Data Acquisition and Post-processing

With the aim of getting more realistic data, the surgeon was asked to perform the operation three times and the raw data for all motions were captured. Then the raw data were analyzed in terms of total working volume, positions, velocities, accelerations and trajectories. The total duration of operation was five minutes which consisted of three phases: Approaching the tool-tip to the eye, insertion of the tool tip into the eye through trocar ports, and tool manipulation inside the eye. In total around 12000 data entries were captured to cover all possible motions during tool manipulation inside the eye. Here, 70 seconds of the vitrectomy performance were analyzed. The vitrectomy procedure was used because the procedure of removing vitreous from the eye (vitrectomy) has the most significant motions among all intra-ocular operations.

3.1.4 Motion Requirements

Tool positions can be seen in Figure 3.4 and Figure 3.5(a) during the vitrectomy of the pig's eye. To simplify the visualizations, the insertion point of the tool-tip was chosen as the reference point and the position and the orientation values were visualized with respect to insertion point. In Table. 3.1 the information observed from the raw data, including minimum and maximum position of the tool and motion ranges for each axis, is summarized. For this procedure the working volume of the surgeon can be defined as $47 \times 63 \times 97 \text{ mm}$ (see Figure 3.4). An interesting fact, which can be observed from these graphs, is that the motion in the X and Y directions is

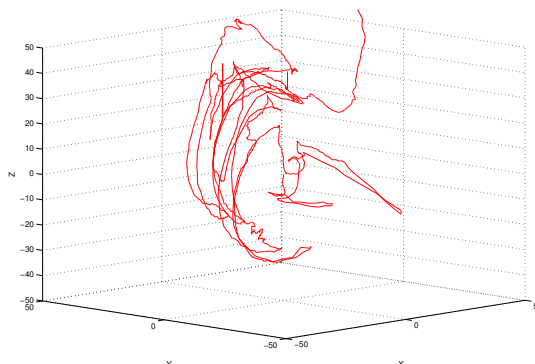
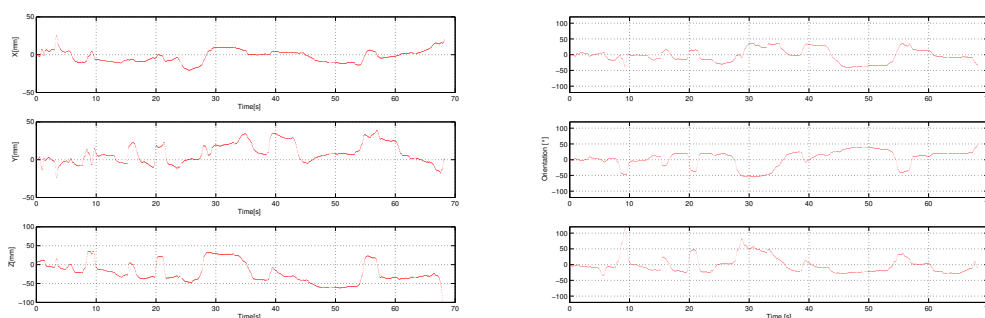


Figure 3.4: Tool trajectory in 3D space

minimal, while the Z displacement is less than $-27mm$ (see Figure 3.5(a)). In other words, the tool tip movement will decrease as it approaches the retina. Figure 3.5(b) represents the tool motion in terms of orientations in this procedure. The maximum, minimum, and the range of angular motion in different directions can be seen in Table 3.1. According to the observation from the angular and linear motions of ophthalmologic surgery, the angular motion about X and Y and linear motion of these axes vary together, which is a consequence of the Remote Center of Motion (RCM) constraint. This constraint forces the surgeon to pivot the tool about the insertion point which is the trocar inserted on the surface of the sclera. However, the rotation around the tool axis (Z) is independent of the linear motion along Z . Figure 4.1(a) shows the linear velocities of the tool. The maximum velocity along the X and Y directions is $20 \frac{mm}{s}$ and along Z direction is $40 \frac{mm}{s}$, but the average velocities are less than $5 \frac{mm}{s}$. Another observation from the velocity diagram is the hand tremor of the surgeon in different directions which can



(a) Tool position during a major procedure in x (1st plot), y (2nd plot) and z (last plot) axes [68]

(b) Tool Orientation during a major procedure A (1st Plot), E (2nd Plot) and R (Last Plot) [68]

Figure 3.5: Tool position and orientation analysis

3. CLINICAL STUDIES AND REQUIREMENT ANALYSIS

Table 3.1: Positions and orientations change during vitrectomy on pig’s eye

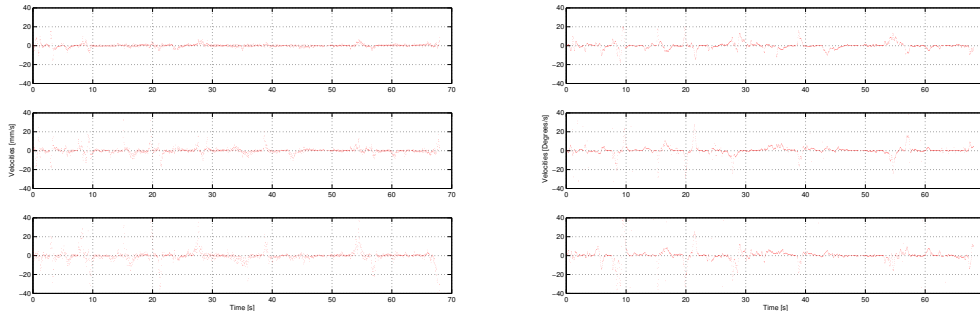
—	X	Y	Z	A	E	R
Min	-21mm	-24mm	-61mm	-36°	-50°	-114°
Max	+26mm	+39mm	+36mm	+16°	+22°	+35°
Range	47mm	63mm	97mm	52°	72°	149°

be observed more specifically than within the position diagram. This effect is consequence of moving to the higher order domain. However, the EMT method is not suitable to measure surgeon’s tremor precisely which according to the state of the art reported less than $200\mu m$ [53].

Figure 4.1(c) is the diagram of angular velocities in the A , E and R directions. The maximum angular velocity around X is $20 \frac{\text{degrees}}{\text{s}}$, around Y is $25 \frac{\text{degrees}}{\text{s}}$ and around Z is $40 \frac{\text{degrees}}{\text{s}}$. The reason of allowing greater angular velocity around Z is the smaller risk of tool rotation around its axis. As in the diagram of linear velocity, Figure 4.1(c), the tremor of the surgeon during angular motions is visible.

3.1.5 Safety and Emergency

Figure 3.7 represents the velocity of the tool in the Z direction when the surgeon wishes to approach the retina. In the left plot the Z motion of the tool can be seen; the right plot shows the Z velocity for the same motion. The comparison of these two plots clearly shows that the velocity in the Z direction is inversely related to the tool-tip distance from the retina. This is due to safety reasons; the surgeon tries to avoid contact with the retinal surface. This condition is important when no intra-ocular force feedback is available and the surgeon must rely on visual feedback from a microscope. The emergency procedure in retinal surgery is to remove the tool



(a) Linear velocities in X , Y and Z directions [68] (b) Angular velocities about X (Azimuth), Y (Elevation) and Z (Roll) [68]

Figure 3.6: Tool linear and angular velocities

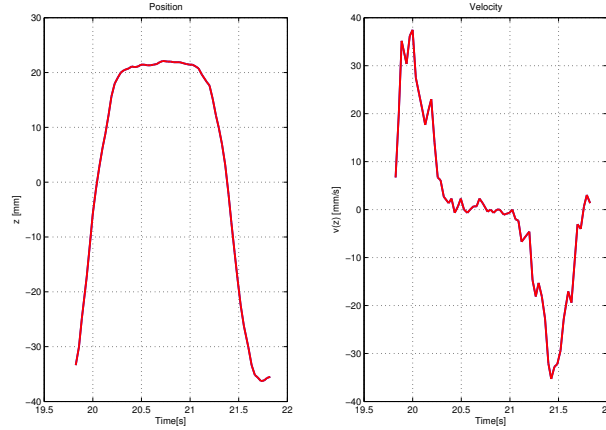


Figure 3.7: Velocity in Z direction while surgeon approaches the retina; left plot is position and right plot is velocity

along the approach axis without any other angular or linear motion. Therefore, it is necessary to design a surgical device or robot for assisting surgeons in retinal surgery, such that it has independent motion along approach axis in the end-effector.

3.1.6 Conclusion

In this chapter the surgical motion during vitreo-retinal surgery was clinically recorded and analyzed. For this purpose, an experimental setup with a combination of an electromagnetic tracking system and a camera was developed. During the experiments, the precise motion of an expert surgeon in 6 DOF was observed and determined. The outcomes of this study are as follows:

- trajectory and working volume of the tool
- position analysis
- orientation analysis
- linear and angular velocities of the tool during the procedures
- emergency reaction by the surgeon

This information, which has not been collected before, will be used to design robotic devices with the aim of performing vitreo-retinal surgery, it is also a clinical reference for validation purposes.

3.2 Eye Model

Understanding the physical properties of the eye and defining the force and torque boundaries during ophthalmic operations are two vital steps towards design and development of robotic solutions for eye surgery. This section describes the development of an eyeball FEA model. Unlike other eyeball FEA studies, this 3D eyeball model contains all three layers of the inner eye: retina, choroid and sclera. Furthermore, the model includes six ocular muscles. The intra-ocular rotation of a needle tool using a trocar during the surgery is another aspect which was considered in this study. Although variables such as the thickness of the layers and the property of the orbits and the muscles are unique for every individual, the model was developed by introducing some assumptions and constraints for an average eye. However, by changing a few parameters, a modified model suitable for individuals can be generated. The model gives the stress distribution when the needle rotates inside the eyeball. The results of this study will give a numerical understanding of the forces which are necessary for ophthalmic operation.

3.2.1 Eye ball models: state of the art

Schutte et al. developed an eyeball FEA model containing 3D orbital biomechanical interactions, such as the four rectus muscles, the eyeball, the orbital fat and also the interactions between these tissues [71]. Yiyi generated an FEA eyeball model with six muscles, and validated the eyeball movement caused by the outside forces [72]. Uchio developed a simulation of an eyeball, which contained cornea, sclera, lens and vitreous layers [73]. This study determined the physical and mechanical impact conditions of foreign bodies caused by intra-ocular foreign body (IOFB) injuries, they used blunt shaped missiles to evaluate the surface of the cornea or sclera, but there was no muscles attached. Norman developed a 2D model of the human sclera, but their model contained only sclera and the optic nerve head [74]. Qi Wei presented a 3D biomechanical model of the oculo motor plant. They obtained simulated results of the eyeball gaze position and trajectories, but the four resulting muscles were modeled as prismatic joints [75]. The most common way to obtain a eyeball geometric model is by deriving the geometry of the orbital structures from MRI scans. Previous studies were used this method to observe the geometric model [71]. Kleut was able to create a 3D model of a human head in Matlab using MRI DICOM data [76]. Norman employed Amira to create a meshed volume of the ocular anatomy from segmented MRI images [74].

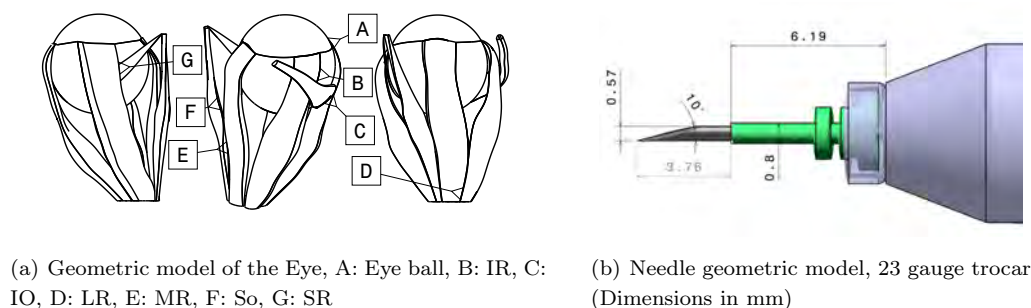


Figure 3.8: Eye and Trocar models [77]

3.2.2 Developed Models

A 3D FEA model of an eyeball and the attached muscles is modeled in this work. The rotation of the needle will lead to a movement of the orbit, and then of the muscles. The orbit will also rotate and influence the needle in turn. By analyzing the stress distribution and the displacement of the attached muscle, the necessary, and maximum allowed force and displacement of the needle is defined. These data are used to design relevant control approaches for the ophthalmic robot.

Eyeball model: The geometric model used in this work is given by Schutte from Delft University of Technology [71], and was derived from frontal MRI scans. A 3D region-growing algorithm was used to accurately segment the anatomical structures of interests, such as the orbit and six extra ocular muscles: Superior rectus (SR), Inferior rectus (IR), Lateral rectus (LR), Medial rectus (MR), Superior oblique (SO) and Inferior oblique (IO) (see Figure 3.8).

Needle model: The most common tools which are used in current ophthalmic surgeries are 23 gauge tools with cross-section diameter of 0.574mm. As a representation of one of these tools, a needle is modeled in this study (Figure 3.8.b shows a simple trocar system tool). Here the needle is assumed to be a rigid body.

3.2.3 Meshed Model and Boundary Conditions

To create the finite elements, the geometric model was imported to the finite-element preprocessor software in IGES format. First, the insertion point of the needle was subtracted from the eyeball surface with a Boolean method. The resulting shell then contains 3089 elements (160 tri elements and 2929 quad elements). Next, the muscles were subdivided into tetrahedral elements with an average edge length of 1mm, resulting in a total number of 16405 muscle

3. CLINICAL STUDIES AND REQUIREMENT ANALYSIS

elements. The needle was considered to be a rigid body and it was meshed into 20 rigid elements (R3D4 element type). The four rectus muscles of the eye and the superior oblique muscle

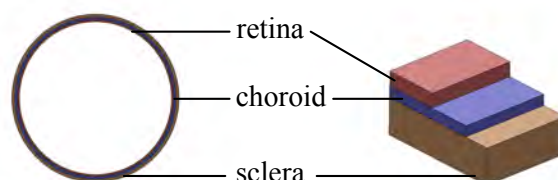


Figure 3.9: Three layers of the eyeball [77]

were fixed to the back of the eye at one end (See Figure 4.1(a)). In the same way, the inferior oblique muscle is attached to the lower front of the nasal orbital wall [72] in this model. This anatomical layout was modeled and additionally, all of the six muscles were connected to the eyeball at the insertion nodes. The eyeball surface was coupled with the central point $(0, 0, 0)$. Considering the natural movement of the eye, this central point was constrained to have solely 3 DOF and perform only rotational movements. The nodes on the eyeball in contact with the needle were assumed to be attached to the surface of the needle. The intra-ocular pressure (IOP) of 2kPa, uniformly distributed on the inner surface of the eyeball, was also taken into consideration within the simulations.

3.2.4 Material Properties

The eyeball is made of several tissues. It consists of three layers, sclera, choroid and retina. According to [76, 78, 79], the thicknesses of these three layers are not constant throughout the whole surface. The innermost layer, the retina, is only present in 72% of the orbit, more precisely in the distal part of the eyeball. However, considering the simplicity of the geometric model and the deformation of the tissues during the surgery, the thicknesses of the layers are assumed to be constant, and there is assumed to be no other tissue inside the eyeball (see Figure 3.9). As it can be seen in Table. 3.2 the tissue properties are assumed to be linear and elastic. The extra ocular muscles are hyper-elastic, and they have similar material properties to silicone rubber [79]. The detailed data of the rubbers mechanical properties can be found in [80]. The surgical needle is made of steel. In contact with the ocular soft tissue, in order to penetrate it, the deformation of the tool is almost none, especially when compared to that

of the eyeball. Both the stress and the deformation can be thus ignored. With the aim of reducing computation costs, the needle is modeled as a rigid body. It should be mentioned that all these values were determined during the course of this thesis. Other research groups, use different values due to the inconstancy of layer thickness, represent different vales., e.g. the mean thickness of retina is 100 - 230 μm in [81], but 249 μm in [82], it depends on the age and the health of the case study, and the insertion position of the needle. It is too complex to define the thickness of the retina in different locations. To reduce the calculations, these assumptions needs to be taken.

Table 3.2: Properties of the eyeball

Property	Sclera	Choroid	Retina
E (Young's modulus)	2900kPa [76]	220kPa [76]	20kPa [76]
ν (Poisson's ratio)	0.4	0.49	0.49 [78]
Thickness (μm)	700 [79]	80 [76]	200

3.2.5 Results

Schutte et al. [71] simulated the eyeball with the rotation of 10.5° as a result of external forces exerted by a tool; Gomez-Perez et al. in their work [83] simulated the eyeball rotating 79.1° due to muscle movement. In this work, the needle was assumed to have a fixed rotation 10° around the incision point in different axes. Table 3.3 shows four different kinds of rotations which was simulated in this work.

Table 3.3: Four kinds of needle rotation

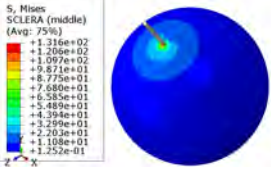
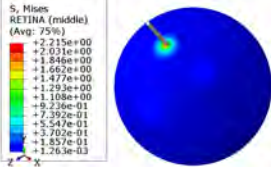
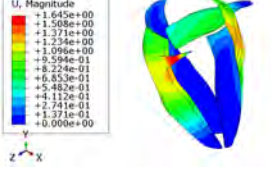
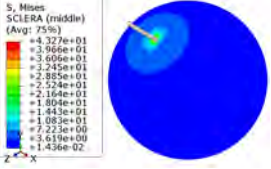
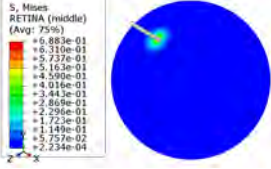
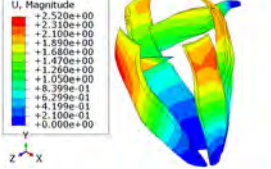
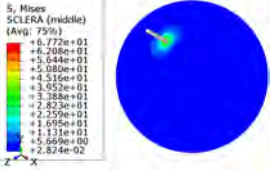
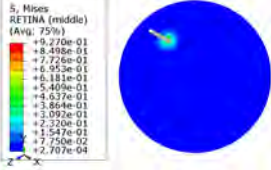
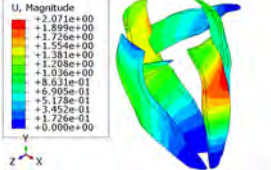
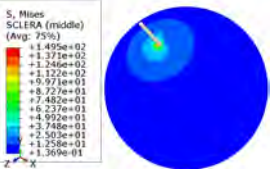
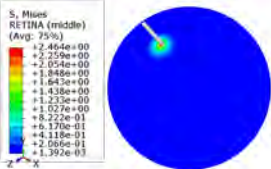
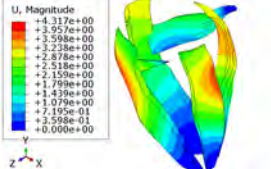
Case	Boundary condition
Case 1	$x=10^\circ, y=0^\circ, z=0^\circ$
Case 2	$x=0^\circ, y=10^\circ, z=0^\circ$
Case 3	$x=0^\circ, y=0^\circ, z=10^\circ$
Case 4	$x=10^\circ, y=10^\circ, z=10^\circ$

Case1: In the first scenario simulated, the needle which was docked to the entry point rotates solely around the x axis. The needle movement is thus constrained to one degree of freedom. The von Mises stress on sclera and retina is shown in Table. 3.4. The largest stress on the sclera is 131.6MPa and on the retina it is 2.2MPa. The highest deformation on the tissue

3. CLINICAL STUDIES AND REQUIREMENT ANALYSIS

is $1.64mm$, located on the superior oblique muscle as it can be seen in Table. 3.4. Accordingly, when the needle rotates around the x axis, the portion of the sclera near the needle will bear the greatest pressure and the stress on retina will be subsequently lower. The SO muscle will deform greatly in order to keep the eyeball steady.

Table 3.4: Properties of the eyeball

	Stress on Sclera	Stress on retina	Muscles deformation
Case 1	 <p>S, Mises SCLERA (middle) (Avg: 75%)</p> <ul style="list-style-type: none"> +1.316e+02 +1.209e+02 +1.097e+02 +9.871e+01 +8.773e+01 +7.680e+01 +6.585e+01 +5.489e+01 +4.394e+01 +3.298e+01 +2.203e+01 +1.108e+01 +1.252e-01 	 <p>S, Mises RETINA (middle) (Avg: 75%)</p> <ul style="list-style-type: none"> +2.215e+00 +2.031e+00 +1.848e+00 +1.662e+00 +1.477e+00 +1.293e+00 +1.108e+00 +9.236e-01 +7.392e-01 +5.547e-01 +3.702e-01 +1.857e-01 +1.263e-03 	 <p>U, Magnitude RETINA (middle) (Avg: 75%)</p> <ul style="list-style-type: none"> +1.645e+00 +1.508e+00 +1.371e+00 +1.234e+00 +1.096e+00 +9.594e-01 +8.224e-01 +6.853e-01 +5.482e-01 +4.112e-01 +2.741e-01 +1.371e-01 +0.000e+00
Case 2	 <p>S, Mises SCLERA (middle) (Avg: 75%)</p> <ul style="list-style-type: none"> +4.327e+01 +3.966e+01 +3.606e+01 +3.245e+01 +2.885e+01 +2.524e+01 +2.164e+01 +1.804e+01 +1.443e+01 +1.083e+01 +7.223e+00 +3.619e+00 +1.436e-02 	 <p>S, Mises RETINA (middle) (Avg: 75%)</p> <ul style="list-style-type: none"> +6.883e-01 +6.310e-01 +5.737e-01 +5.163e-01 +4.589e-01 +4.016e-01 +3.443e-01 +2.869e-01 +2.295e-01 +1.721e-01 +1.148e-01 +5.757e-02 +2.734e-04 	 <p>U, Magnitude RETINA (middle) (Avg: 75%)</p> <ul style="list-style-type: none"> +2.520e+00 +2.310e+00 +2.100e+00 +1.890e+00 +1.680e+00 +1.470e+00 +1.260e+00 +1.050e+00 +8.399e-01 +6.299e-01 +4.199e-01 +2.100e-01 +0.000e+00
Case 3	 <p>S, Mises SCLERA (middle) (Avg: 75%)</p> <ul style="list-style-type: none"> +6.772e+01 +6.208e+01 +5.644e+01 +5.080e+01 +4.516e+01 +3.952e+01 +3.388e+01 +2.823e+01 +2.259e+01 +1.695e+01 +1.131e+01 +5.669e+00 +2.824e-02 	 <p>S, Mises RETINA (middle) (Avg: 75%)</p> <ul style="list-style-type: none"> +9.270e-01 +8.408e-01 +7.546e-01 +6.683e-01 +5.821e-01 +4.959e-01 +4.097e-01 +3.235e-01 +2.373e-01 +1.511e-01 +7.502e-02 +3.750e-02 +2.707e-04 	 <p>U, Magnitude RETINA (middle) (Avg: 75%)</p> <ul style="list-style-type: none"> +2.071e+00 +1.899e+00 +1.726e+00 +1.554e+00 +1.381e+00 +1.208e+00 +1.036e+00 +8.631e-01 +6.905e-01 +5.178e-01 +3.452e-01 +1.726e-01 +0.000e+00
Case 4	 <p>S, Mises SCLERA (middle) (Avg: 75%)</p> <ul style="list-style-type: none"> +1.495e+02 +1.371e+02 +1.246e+02 +1.122e+02 +9.971e+01 +8.727e+01 +7.482e+01 +6.237e+01 +4.992e+01 +3.748e+01 +2.503e+01 +1.258e+01 +1.369e-01 	 <p>S, Mises RETINA (middle) (Avg: 75%)</p> <ul style="list-style-type: none"> +2.464e+00 +2.259e+00 +2.054e+00 +1.848e+00 +1.643e+00 +1.438e+00 +1.233e+00 +1.027e+00 +8.22e-01 +6.170e-01 +4.118e-01 +2.060e-01 +1.392e-03 	 <p>U, Magnitude RETINA (middle) (Avg: 75%)</p> <ul style="list-style-type: none"> +4.317e+00 +3.998e+00 +3.679e+00 +3.360e+00 +3.041e+00 +2.722e+00 +2.403e+00 +2.084e+00 +1.765e+00 +1.446e+00 +1.127e+00 +8.08e-01 +4.891e-01 +0.000e+00

Case 2: In another scenario the needle rotation of 10° fixed at the incision point and around the y axis is modeled. As in the first scenario, the other degrees of freedom are fixed. The von Mises stress on sclera and retina is illustrated in Table 3.4. The largest stress on sclera is $43.27MPa$, on the retina it is $0.68MPa$. The most substantial deformation of the tissue is $2.52mm$, this being located on the SR muscle.

Case 3: In the case of a 10° rotation of the needle exclusively around the z axis and fixed at the incision point with the other degrees of freedom constrained, the von Mises stress on sclera and retina is shown in Table 3.4. The maximum stresses on the sclera and retina are found to be $67.72MPa$ and $0.93MPa$ respectively. In this case the MR muscle undergoes the

highest deformation, which is 2.07mm .

Case 4: A movement with higher degrees of freedom is modeled as well. In this case, the needle rotates 10° around the x , y and z axis simultaneously and fixed at the incision point. Higher maximum stresses can be observed on both sclera and retina compared with the previous cases: 149MPa and 2.46MPa . The maximum deformation, borne by the SR muscle in this case is also higher: 4.37mm .

The noticeable rise in the stresses can be explained by the fact that the needle rotates about three axes, and consequently, the total displacement is at a maximum. As shown in Figure 3.10(a), the sclera bears a greater stress than the retina. This is due to the material properties; more specifically the fact that the sclera has a larger Young's modulus than the retina. The force on the eyeball layers in case 1 is 0.67% bigger than in case 2, and it surpasses the one in case 3 by 49% . The location of the needle and the angle of the needle with respect to the eyeball, gives rise to this difference. As Figure 3.10(b) shows, different rotation directions produce maximum deformation located in different muscles. In this respect, the length, thickness and the position of the muscle cannot be ignored in the biomechanical analysis of the orbit.

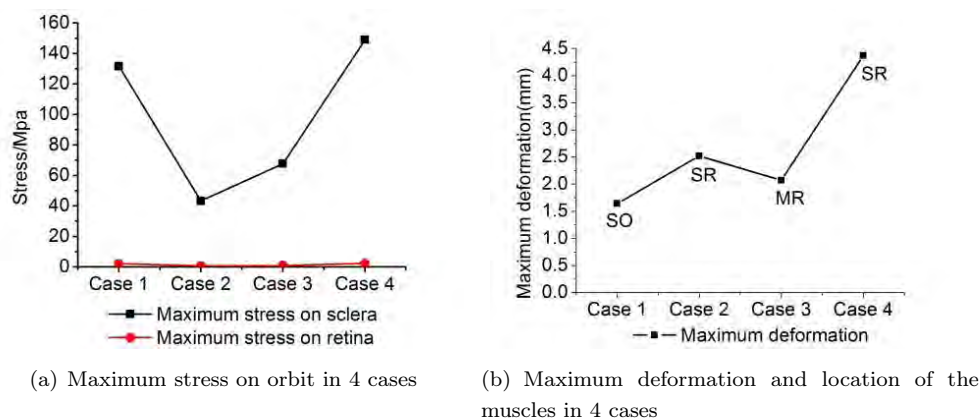


Figure 3.10: Stress and deformation of the eyeball and the muscles [77]

3.2.6 Eyeball FEA Model Conclusion

An eyeball FEA model with three layers together with the attached muscles was developed in this part of the work. This model also includes the needle penetrating the three layers of the inner eye, which can simulate the rotation of the needle during an eye surgery accurately. The

3. CLINICAL STUDIES AND REQUIREMENT ANALYSIS

IOP was also considered in this analysis. The simulated results specifically the stress and strain distribution, the pressure on the surface of the eyeball and the displacement of the muscles give a better understanding of how the eyeball interacts with surgical devices. This can help in the design of a mechanical robot. The sclera has a larger Young's modulus than the retina. Taking this into account when the robot is programmed to assist in the eyeball surgery, a much larger force will be exerted on the sclera than on the retina, as the needle moves inside the eyeball. Furthermore, as mentioned previously, when the needle rotates around the x axis, the orbit layers will bear more force than when the needle is rotating in other directions. The position of the muscle can also affect the stress distribution on the eyeball. Correspondingly, if the surgeon has knowledge prior to the operation about the precise force and deformation that the eye can undergo, the surgery can be planned optimally. Concerning future research, in this domain, in order to overcome the limitations of the current assumptions, more detailed work could be undertaken. The thickness of the layers could be made variable; the aqueous fluid inside the eye might be added to the FEA model; and friction between the eyeball and the needle might be considered. Moreover, the material properties of the ocular tissue should be validated with some empirical data.

3.3 Design Requirements

This chapter analyzed the requirements of the ophthalmic surgical robot which deals with the physiological behaviors of the surgeon and the anatomical properties of the eye. A series of studies was carried out comprising surgeon's motion tracking and eyeball modeling during the requirement analysis. The observed data from the tracking contains position, velocity and acceleration of the surgical tool in 6DOF while being manipulated by the surgeon during an ophthalmic operation. It also gives an understanding of the surgeon's behavior in three operational phase: approach, insertion and manipulation. Eyeball modeling on the other hands offer information regarding the minimum and maximum force and torques needed to perform the vitreo-retinal surgery. Both sets of information are used to design the robotic setup, simulation environment and also to evaluate the results in each development phase.

Chapter 4

Kinematics

Following the requirement analysis and taking the state of the art into consideration, the kinematic design of the manipulator was begun. To optimize the design and development, surgeons, as end users, was kept updated in each step of this phase. Their evaluation and feedback were an important factor for kinematics modification. This chapter presents the first prototype of the manipulator, the reasons why the first prototype failed and the successful modified design: a Hybrid Parallel-Serial configuration.

4.1 First Prototype

The first step after the definition of requirements was to design and develop a preliminary prototype. An early stage prototype, as a physical and touchable device, could aid the medical doctors understanding of the robotic technology. Although the first prototype had serious challenges for adoption into the clinical environment, it helped to establish a Medicine-Engineering interdisciplinary language.

4.1.1 Design and Development

Figure 4.1 shows the kinematics of the first prototype. It consisted of two main segments: The first segment was a 3DOF serial configuration of revolute joints and the second segment was a parallel configuration of three prismatic joints attached to the first segment. The dimensions of the prototype was $220 \times 60 \times 60mm$ and its weight was $0.450 kg$. By using piezo actuation technology, hypothetically speaking, the precision of the robot could be less than $20\mu m$. This robot was designed to be mounted on the ophthalmic microscope. During the surgery, whenever the up-skilling of the surgeon's manipulation was needed (e.g. retinal vein cannulation), the

4. KINEMATICS

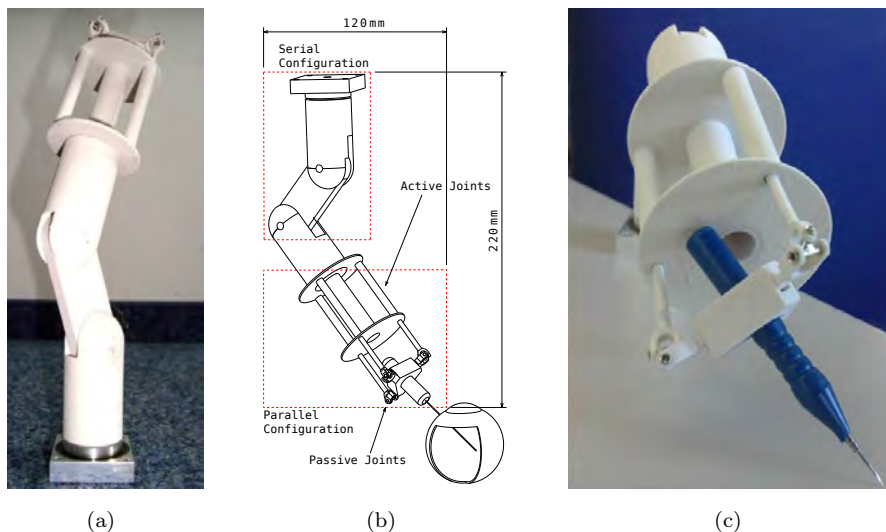


Figure 4.1: First prototype

robot could be utilized. The surgeon, using a 6DOF input device, could control the precise motion of the robot.

4.1.2 Evaluation

A mock up model of this early stage prototype, using a 3D prototyping printer ¹, was built. The mock up model was evaluated by surgeons under clinical conditions. Preliminary experiments show that although this configuration satisfies the precision and intra-ocular maneuver, it would be complicated to integrate into the ophthalmic operation room. The main source of these complications was the microscope-mounting concept. The relative position of the microscope with respect to the patient's body is not constant during the surgery. Therefore, it causes an additional unwanted motion which must be compensated. However, the large mechanical loop between robot-microscope-operation table-patient dramatically increase the setup vibration.

4.1.3 Results

Based on surgeons' feedback and results from clinical experiment, it was realized that this configuration is not suitable for eye surgery. Following the evaluation of the first prototype, these conclusions were drawn:

¹EOS-FORMIGA P110

4.2 Parallel Coupled Joint Mechanism (PCJM)

- In principle, Hybrid Parallel-Serial configuration is suitable as it offers precision and stability.
- Piezo actuators are appropriate choices for ophthalmic micromanipulator actuation. This technology enables the highest precision in a compact package.
- To guarantee the intuitive control of the robot at least five degrees of freedom are necessary.
- Ideally the robot should be mounted on the eye or the head of the patient.

4.2 Parallel Coupled Joint Mechanism (PCJM)



Figure 4.2: Parallel Coupled Joint Mechanism (PCJM), developed as the main joint mechanism of the robot for ophthalmic surgery [84].

Taking all the aforementioned experiences, including the requirements and prototype results, into consideration, a new version of the micro-manipulator was designed. The new setup design was based on a small innovative, robotic joint with high precision and high stability. This 2DOF mechanism was invented for this work, and is called Parallel Coupled Joint Mechanism (PCJM).

In this mechanism the differential displacement of two translational motions is converted to one translation and one rotation (see Figure 4.3). It should be noted that $L1$ and $L2$ are linear displacements of each prismatic joint at distance d from each other.

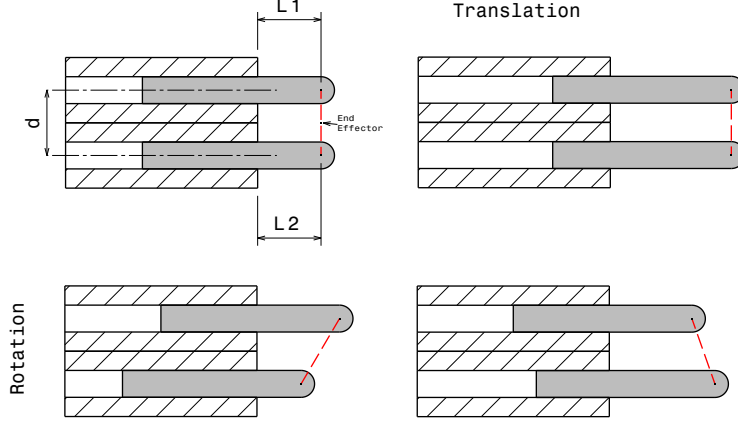


Figure 4.3: Simple schematic of a PCJM

4.2.1 Mathematical Model

Figure 4.5 shows the simplified model of a PCJM which was developed in this work. L and θ are linear and angular displacements of the mechanism, d_m is the length of the end effector and L_{tool} is the length of the tool, from gripper to tool tip. Eq. (4.1) represents the simplification of the mechanism by mapping $L1$ and $L2$ to L and θ , respectively:

$$L = \frac{L1 + L2}{2}, \quad \theta = \arctan\left(\frac{L2 - L1}{d}\right) \quad (4.1)$$

To guarantee a 1:1 mapping of $L1$, $L2$ to L and θ , the singularities of the mapping should be analyzed. The Jacobian matrix (J_L) is written as follows:

$$\begin{bmatrix} q_1 \\ q_2 \end{bmatrix} = f \begin{bmatrix} L1 \\ L2 \end{bmatrix}, \quad q_1 = L \quad \text{and} \quad q_2 = \theta \quad (4.2)$$

$$\dot{q} = \overbrace{\frac{\partial f(L)}{\partial L}}^{J_L} \dot{L}$$

$$\begin{bmatrix} \dot{q}_1 \\ \dot{q}_2 \end{bmatrix} = \begin{bmatrix} \frac{1}{2} & \frac{1}{2} \\ \frac{-d}{d^2 + (L2 - L1)^2} & \frac{d}{d^2 + (L2 - L1)^2} \end{bmatrix} \begin{bmatrix} \dot{L}_1 \\ \dot{L}_2 \end{bmatrix}$$

It can be observed that the determinant of the Jacobian matrix (J_L) is 0, if and only if $d = 0$ which implies that for the proposed configuration, where the distance of two prismatic parallel actuators is more than 0, J_L matrix is full rank. Therefore, no singularities exist, in other words, for any $L1$ and $L2$ there exist a unique L and θ and vice versa.

4.2 Parallel Coupled Joint Mechanism (PCJM)

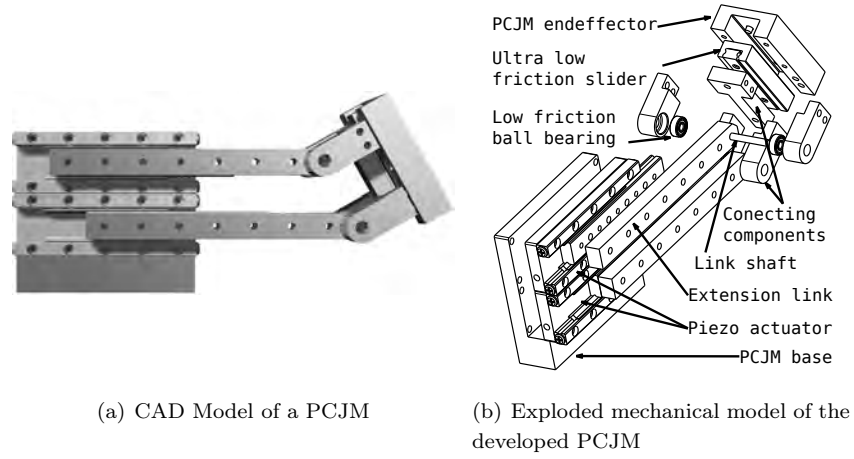


Figure 4.4: Parallel Coupled Joint Mechanism (PCJM) models

4.2.2 CAD Model

Following the mathematical proof of the concept, a realistic CAD model of a PCJM was developed (see Figure 4.4(a)). The model consists of two actuated prismatic joints, two passive rotational joints and a passive slider (see Figure 4.4(b)).

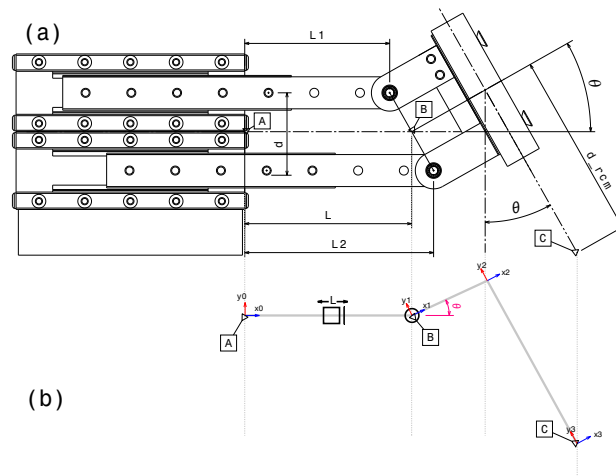


Figure 4.5: a: A PCJM and b: its simplified model

4. KINEMATICS

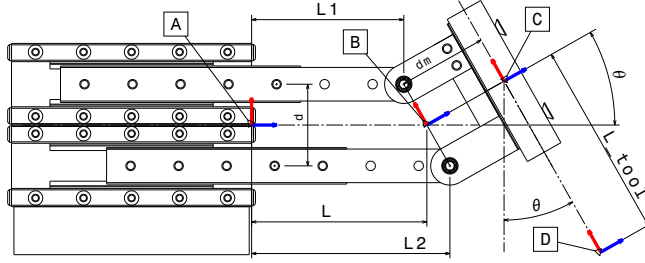


Figure 4.6: A simplified PCJM model

4.2.3 Kinematics Analysis

The modeled PCJM, or in general any PCJM configuration, is simplified to a prismatic and a revolute joint (see Figure 4.5). Therefore, its kinematics are analyzed as a simple serial configuration.

For instance, the simplified homogeneous transformation matrix of point B in Figure 4.6 with respect to point A is:

$$T_A^B = \begin{bmatrix} \cos \theta & -\sin \theta & 0 & L \\ \sin \theta & \cos \theta & 0 & 0 \\ 0 & 0 & 1 & 0 \\ 0 & 0 & 0 & 1 \end{bmatrix} \quad (4.3)$$

Forward Kinematics: For points A, B, C and D in Figure 4.6, homogeneous transformation matrix $T_A^D = T_A^B T_B^C T_C^D$ of the tool tip (D) with respect to the base (A) is:

$$T_A^D = \begin{bmatrix} \cos \theta & -\sin \theta & 0 & \overbrace{L - L_{tool} \sin \theta + d_m \cos \theta}^{F.K} \\ \sin \theta & \cos \theta & 0 & L_{tool} \cos \theta + d_m \sin \theta \\ 0 & 0 & 1 & 0 \\ 0 & 0 & 0 & 1 \end{bmatrix} \quad (4.4)$$

The homogeneous transformation matrices are simplified by substituting L_1 and L_2 for θ and L . The substitution procedure is accomplished using trigonometric identities.

$$\cos \left(\arctan \left(\frac{L_2 - L_1}{d} \right) \right) = \frac{1}{\sqrt{1 + \frac{(L_2 - L_1)^2}{d^2}}} \quad (4.5)$$

$$\sin \left(\arctan \left(\frac{L_2 - L_1}{d} \right) \right) = \frac{L_2 - L_1}{d \sqrt{1 + \frac{(L_2 - L_1)^2}{d^2}}}$$

Using these formulae, configurations consisting of PCJM can be simplified and analyzed as a simple serial manipulator.

Inverse Kinematics: The inverse kinematic equations of a PCJM (for the point B) in Figure 4.6 is:

$$L1 = L + \frac{d}{2} \sin(\theta), \quad L2 = L - \frac{d}{2} \sin(\theta) \quad (4.6)$$

Semi-mechanical Variable Remote Center of Motion (RCM) Determination: For medical and surgical applications, such as eye surgery, it is necessary to pivot the tool around a certain point (e.g. pivoting the ophthalmic tool around the trocars). Taking the forward kinematics equations from (4.4), the 2D position of Point D (X_D, Y_D) in Figure 4.6 and solving Eq.(4.7), a unique dependency of L , θ and L_{tool} is observed.

$$\begin{bmatrix} L - L_{tool} \sin \theta + d_m \cos \theta \\ L_{tool} \cos \theta + d_m \sin \theta \\ 0 \\ 1 \end{bmatrix} = \begin{bmatrix} X_D \\ Y_D \\ 0 \\ 1 \end{bmatrix} \quad (4.7)$$

This dependency enables pivoting the tool around point D as a Remote Center of Motion (RCM). In the $L1$ and $L2$ domain, this situation is interpreted as the dependent differential displacement of two parallel prismatic joints. Changing the RCM during the motion is therefore possible. This situation for intraocular ophthalmic surgery is relevant when the surgeons need to move the eye to see different regions of the retina.

4.2.4 Advantages of PCJM over Serial Prismatic and Revolute Joint Configuration

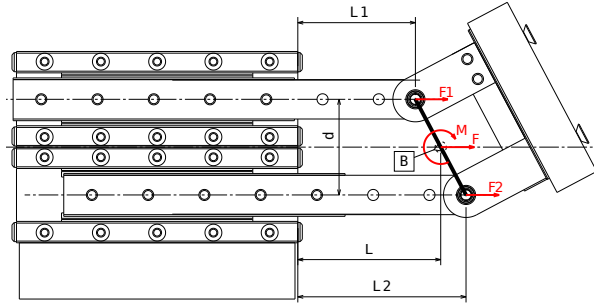


Figure 4.7: Statics analysis of PCJM

As described in the previous paragraphs, the PCJM is similar to a serial pair of prismatic-revolute joints. The advantages of this mechanism over standard serial prismatic-revolute configuration are as follows:

Stiffness: the parallel pair provides higher stiffness of the end effector against mechanical disturbances than a serial configuration [85, 86, 87].

4. KINEMATICS

Precision: piezo prismatic actuators with sub nano precision are among the most accurate available actuators.

Output force: Figure 4.7 presents the static forces of PCJM. The total force which is applied to point B is $F = F1 + F2$ and the moment applied to that point is $M = \frac{\vec{d} \times (\vec{F1} - \vec{F2})}{2}$. Therefore, both actuators apply forces and moments to point B, as opposed to a classic serial prismatic-rotational configuration of a prismatic actuator with output force of greater than F and rotational actuator with the moment of greater than M . Therefore, both actuators apply both force and moment to B, whereas in a traditional serial configuration, only the prismatic actuators provides force and the revolute actuator provides moment. In order to match the combined force and moments of the PCJM, much more powerful, and therefore heavier actuators would be necessary. Therefore, the proposed mechanism can be more compact than a serial pair applying the same force and moment.

Adjustable RCM: Any physical and virtual point that is in angular reach of the system can be defined as the pivoting point of the end effector or attached tool. This point can be changed or moved during motion.

4.3 Serial Configuration

Following the theoretical proof of the PCJM concept and simulation-based evaluations, a serial configuration of PCJM segments was proposed to perform 6 DOF manipulation. This configuration consisted of three main serial segments; 1) two PCJMs, 2) the tool gripper comprising a prismatic actuator for tool translation and 3) an optional revolute actuator for tool rotation.

Figure 4.8.(a) represents the serial configuration. In the previous section, it was shown that the parallel coupled joint can be represented by a prismatic and a revolute joint to simplify the analysis. In Figure 4.8.(b) the simplified model of the serial robot is shown.

4.3.1 Mathematical Model

To simplify the analysis, each PCJM can be represented by a prismatic and a revolute joint. Considering the mechanical structure of the manipulator, a more realistic simplified model is observed, which is shown in Figure 4.9. The Denavit-Hartenberg parameters [89] were derived from a CAD model and are listed in Table 4.1.

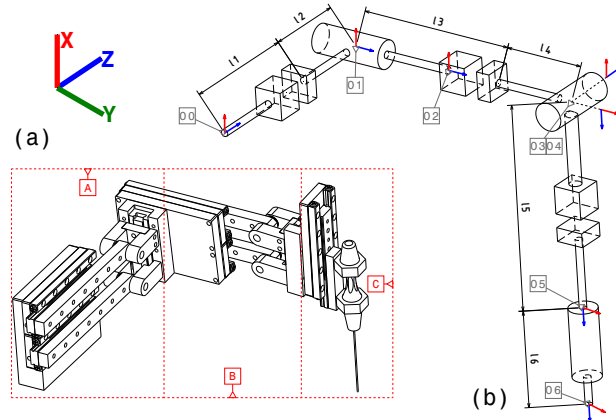


Figure 4.8: (a) Serial robot: A and B are parallel coupled joint elements. C is the tool gripper consisting of a prismatic actuator and an optional tool rotator, (b) relevant and simplified model of the serial robot [88].

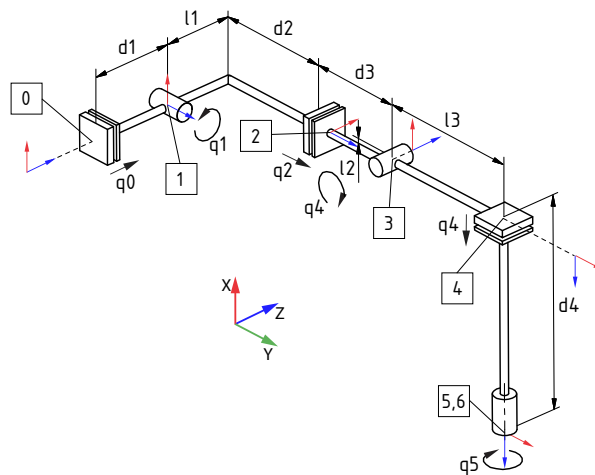


Figure 4.9: The simplified serial robot.

4.3.2 CAD Model

A CAD model of the serial manipulator consisting of two PCJM segments and an additional prismatic stage (actuator) was generated (see Figure 4.10). Suitable interfaces to link two stages was modeled and design details such as assembly methods were considered. A prototype of the micro-manipulator using this model was later prepared using a 3D prototyping machine. The same model was used to develop the simulation/training environment of the setup.

4. KINEMATICS

Table 4.1: The Denavit-Hartenberg parameters (distal) for the serial robot.

Link	ϕ_i	d_i	a_i	α_i	Offsets	mm
1	0	$d_1 + q_0$	0	$-\frac{\pi}{2}$	l_1	32.5
2	$q_1 - \frac{\pi}{2}$	d_2	l_1	0	l_2	1.33
3	$\frac{\pi}{2}$	$d_3 + q_2$	l_2	$\frac{\pi}{2}$	l_3	40.5
4	$q_3 + \frac{\pi}{2}$	0	l_3	$-\frac{\pi}{2}$	d_1	22
5	0	$d_4 + q_4$	0	0	d_2	20
6	q_5	0	0	0	d_3	22
					d_4	55.35

4.3.3 Kinematics Analysis

Here, the kinematic analysis of the serial robot is discussed. **Forward Kinematics** Using Table. 4.1 the forward kinematics of the manipulator is calculated as:

$$T_0^6 = \prod_{i=1}^6 T_{i-1}^i \quad (4.8)$$

where $T_{i-1}^i \in \mathbb{R}^{4 \times 4}$ is the homogeneous transformation from frame i to $i - 1$ and is determined via the Denavit-Hartenberg parameters. The resulting transformation matrix (T_0^6) is given as:

$$\begin{pmatrix} -s_1 s_5 - c_1 c_5 s_3 & c_1 s_3 s_5 - c_5 s_1 & -c_1 c_3 & l_2 c_1 + l_1 s_1 - c_1 c_3 (d_4 + q_4) - l_3 c_1 s_3 \\ c_3 c_5 & -c_3 s_5 & -s_3 & d_2 + d_3 + q_2 - s_3 (d_4 + q_4) + l_3 c_3 \\ c_5 s_1 s_3 - c_1 s_5 & -c_1 c_5 - s_1 s_3 s_5 & c_3 s_1 & d_1 + q_0 + l_1 c_1 - l_2 s_1 + c_3 s_1 (d_4 + q_4) + l_3 s_1 s_3 \\ 0 & 0 & 0 & 1 \end{pmatrix} \quad (4.9)$$

with $s_i := \sin(q_i)$, $c_i := \cos(q_i)$.

The last column defines the forward kinematics of the end effector

$$\begin{pmatrix} e_x \\ e_y \\ e_z \end{pmatrix} = \begin{pmatrix} l_2 c_1 + l_1 s_1 - c_1 c_3 (d_4 + q_4) - l_3 c_1 s_3 \\ d_2 + d_3 + q_2 - s_3 (d_4 + q_4) + l_3 c_3 \\ d_1 + q_0 + l_1 c_1 - l_2 s_1 + c_3 s_1 (d_4 + q_4) + l_3 s_1 s_3 \end{pmatrix} \quad (4.10)$$

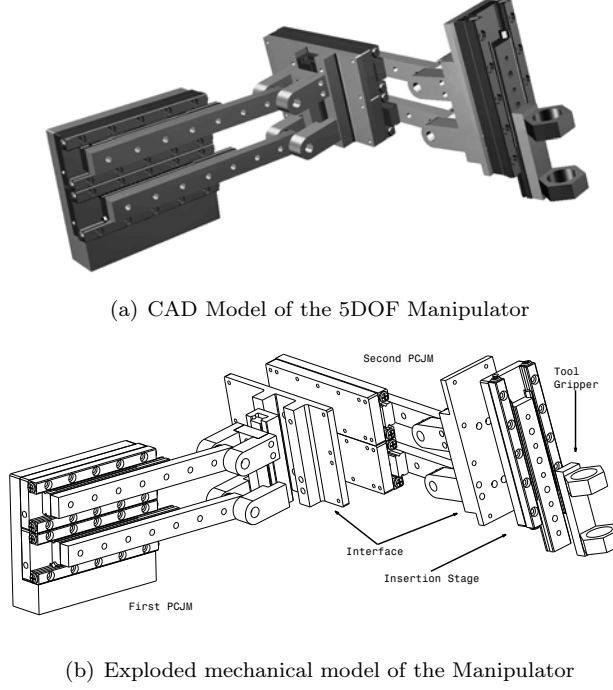


Figure 4.10: Hybrid Serial-Parallel configuration

Inverse Kinematics Given the numerical transformation matrix T_0^6 , the inverse kinematics can be directly derived. First the revolute offsets are calculated via¹:

$$\begin{aligned} q_1 &= \operatorname{atan2}(T_0^6(3, 3), -T_0^6(1, 3)) &&= \operatorname{atan2}(c_3 s_1, c_3 c_1) \\ q_3 &= \operatorname{atan2}\left(-T_0^6(2, 3), -\frac{T_0^6(1, 3)}{c_1}\right) &&= \operatorname{atan2}(s_3, c_3) \\ q_5 &= \operatorname{atan2}(-T_0^6(2, 2), T_0^6(2, 1)) &&= \operatorname{atan2}(c_3 s_5, c_3 c_5) \end{aligned}$$

For the translational part the inverse kinematics is solved for q_4 , q_2 and q_0 :

$$\begin{pmatrix} q_4 \\ q_2 \\ q_0 \end{pmatrix} = \begin{pmatrix} -\frac{p_x - l_2 c_1 - l_1 s_1 + d_4 c_1 c_3 + l_3 c_1 s_3}{c_1 c_3} \\ p_y - d_3 - d_2 + s_3(d_4 + q_4) - l_3 c_3 \\ p_z - d_1 - l_1 c_1 + l_2 s_1 - c_3 s_1(d_4 + q_4) - l_3 s_1 s_3 \end{pmatrix} \quad (4.11)$$

Furthermore, the mapping from L_i and θ_i of the PCJMs and the configuration of the pris-

¹All $\operatorname{atan2}$ operations and divisions are well defined due to the mechanical design of the robot i.e. c_1 and c_3 will never reach zero.

4. KINEMATICS

matic and revolute joints from the serial robot is defined as:

$$L_2 := q_0, \quad \theta_1 := q_1 \quad (4.12)$$

$$L_4 := q_2, \quad \theta_2 := q_3 \quad (4.13)$$

and

$$L_1 := L_2 - d * \tan(\theta_1) \quad (4.14)$$

$$L_3 := L_4 + d * \tan(\theta_2) \quad (4.15)$$

where the signs differ because of the reversed coordinate frames at the respective revolute joints.

Singularities To determine singularities in the serial configuration, the Jacobian matrix was analyzed:

$$J = \begin{bmatrix} 0 & c_2 s_1 L_5 & 0 & c_1 s_2 L_5 & -c_1 c_2 & 0 \\ 0 & 0 & 1 & -c_2 L_5 & -s_2 & 0 \\ 1 & c_1 c_2 L_5 & 0 & 0 & c_2 s_1 & 0 \\ 0 & 0 & 0 & -s_1 s_2 L_5 & 0 & -c_1 c_2 \\ 0 & 1 & 0 & s_1 & 0 & -s_2 \\ 0 & 0 & 0 & c_1 & 0 & c_2 s_1 \end{bmatrix} \quad (4.16)$$

The determinant is:

$$\det(J) = c_1^3 c_2^2 + c_1 c_2^2 s_1^2 \quad (4.17)$$

This determinant is zero, if and only if $\theta_1 = 2k\pi$ or $\theta_2 = 2k\pi$ which for this robot is an impossible configuration. Therefore, this robot has no singularities in its working space.

Semi-mechanical Variable RCM Determination (3D Space): Similar to the determination of the RCM for a single joint, utilizing PCJM in a 6DOF robot permits variable RCMs in 3D space. Any virtual or physical points in space (excluding the singular configuration) can be defined as a pivoting point. During the motion this point is movable. The importance of this specification for ophthalmic surgery is that the surgeon can move the eyeball by changing the position of the RCM during the surgery, and continue the operation. In conventional manual ophthalmic surgery this situation helps surgeons to see the different areas of the retina through the microscope.

4.3.4 Reachability Analysis

Considering the physical characteristics of the robot and its position and orientation with respect to the eye, reachability of the surgical tool is investigated in this section.

4.3.4.1 Workspace

Considering only translational movement, i.e. is parallel movement of the first four piezo positioners with travel ranges of $\pm 15mm$, the workspace is bounded by a cube with dimensions $30 \times 30 \times 30mm$. By also taking rotations into account, i.e. displacement of the linear positioners

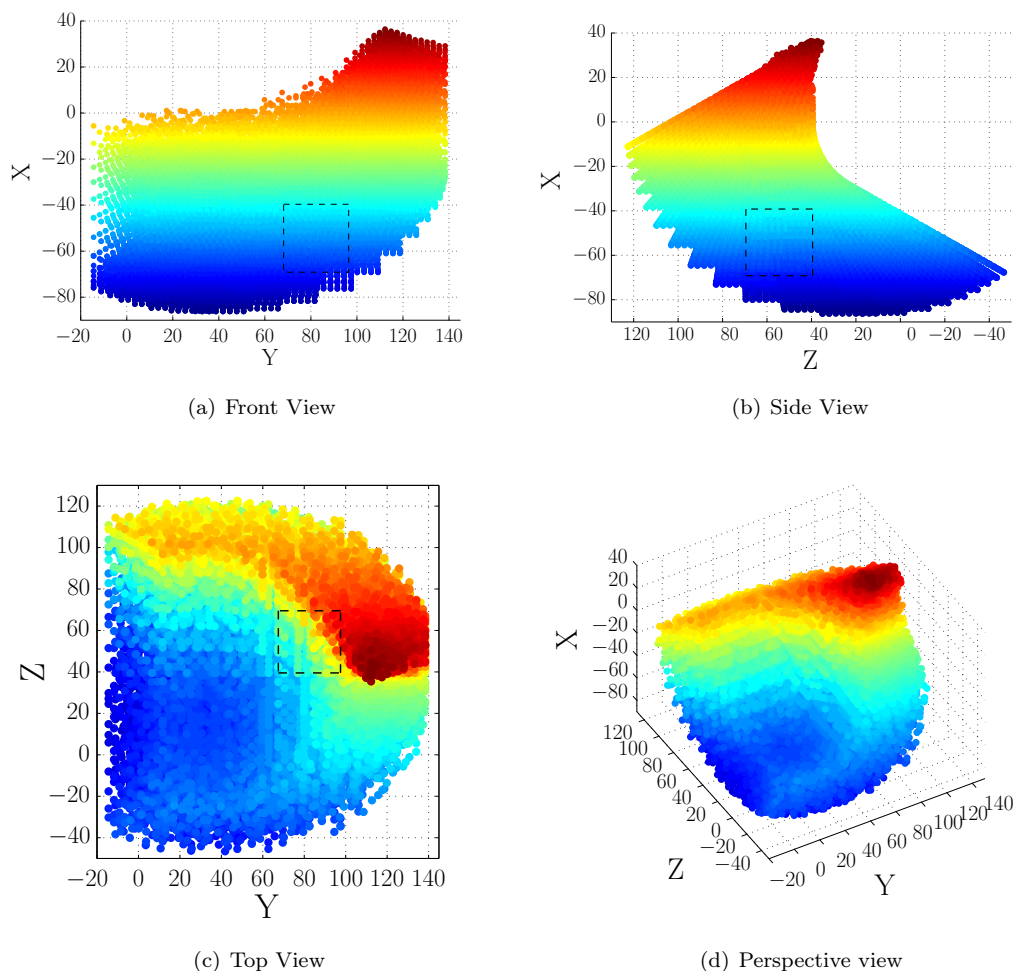


Figure 4.11: The sampled workspace of the robot

with respect to each other, the workspace is determined as displayed in Figure 4.11. The figure shows sampled positions the end effector can obtain. The rectangle in every view shows the area that is accessible with translational movement only.

4.3.4.2 Reachability within the Eye

For the robot to be used in practice, it is essential that it covers the regions of the eye that have to be accessible during a surgical procedure. However, enforcing an RCM constraint limits the workspace considerably, depending on where it is placed. This is due to the fact that two degrees of freedom are lost. As a result, in order to access different regions of the retina, the RCM location needs to be changed accordingly during surgery. To further assess the practicability of the robotic setup the reachability within the eye is examined under different RCM constraints.

4. KINEMATICS

More specifically, the location of the eye with respect to the robot base is investigated, which then automatically defines the location of the RCM on the eye. Moreover, the tilt of the robot about the z -axis is included.

4.3.4.3 Model of the Eye

Due to the fact that the posterior part of the eye can be assumed to be spherical [90], the eye is modeled as a simple sphere with a diameter of 24.2mm [91]. The cannula for inserting

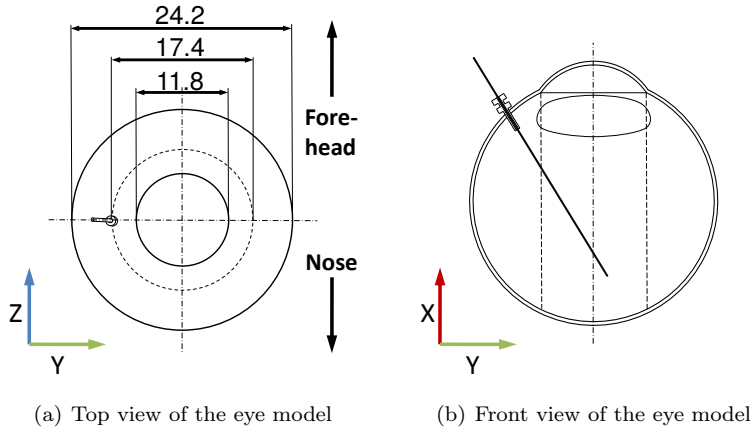


Figure 4.12: The eye model used in the analysis.

the tool into the eye is placed about 3.5mm away from the cornea [4] and defines the location of the RCM. Additionally, another constraint is taken into account: Because the surgeon uses the microscope during intra-ocular procedures it is essential that areas which are accessible overlap with the field of view of the microscope. For this, a simple model is applied where the inner eye is assumed to be visible through a circular hole defined by the average radius of the cornea without refractions from the lens. This is a suitable approximation, because normally the radius of the pupil is not as wide as the cornea. Figure 4.12 shows the relevant parameters of the model. The diameter of the eyeball and the cornea are taken from [91]. The diameter on which the cannula is placed, is a result of the offset by 3.5mm from the cornea [62]. By rotating the eye about its center, the RCM is relocated and the line of sight transforms accordingly, as displayed in Figure 4.13(a) and 4.13(b). In the analysis a maximum rotation of the eye of 30 degrees about the z -axis is assumed and the rotation in the direction of the cannula is limited to a maximum of -15 degrees. For the y -axis the rotation is limited to ± 10 degrees. Additionally, in rotating the eye about its center it is assumed that the RCM location can be determined automatically and that translational movement of the eye is negligible as proposed in [75].

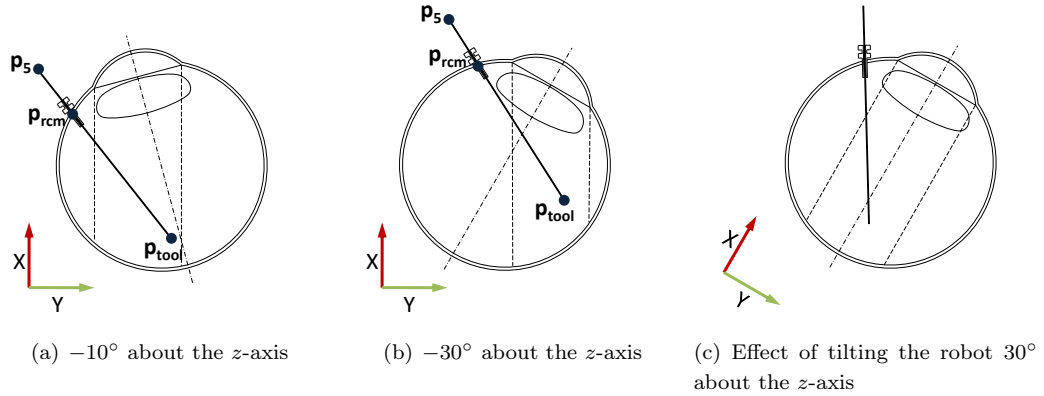


Figure 4.13: Different rotations of the eye and tilt of the robot.

4.3.5 Optimum Location of the Eye

For determining the optimum location of the eye with respect to the robot base for robotized surgery as well as the necessary tilt of the robot the following method is applied:

- First, a suitable location is determined by observation during the clinical trials until satisfactory results are yielded within a certain predefined range of rotations of the eye. This location is referred to as *the reference location*.
- Second, the workspace of the robot is sampled. The sampled points are taken as an input for initial RCM locations from which the offset of the eye is calculated and then compared to the reference. The reference will be used for preliminary filtering to reduce computational complexity as well as in-depth determining potentially better locations.

In the analysis the eyeball is rotated by -10 to 30 degrees about the z -axis and -10 to 10 degrees about the y -axis in steps of 10 degree.

A first and naive approach is to place the eye within the $30 \times 30 \times 30$ mm cube to obtain potentially satisfactory results. More specifically, the center of the eye is set to the location of the tip of the tool where all actuators are in reference positions. From this the RCM location is calculated and the analysis of reachable as well as visible areas within the eye is conducted. Figure 4.14.a illustrates the result with the eye in zero position. The red dots represent areas that can be reached by the instrument of the robot. Blue dots are those which are visible through the simplified circular hole. Green dots indicate areas that are visible and reachable, however, they are not present in this configuration. With the chosen offset for the center of the eye, the reachable area is quite large, but the setup is not of much usage, because areas that are visible are not accessible by the robot. The situation is similar within the neighbourhood of the chosen offset. Therefore, another parameter is taken into account. By rotating the robot clockwise about its z -axis the workspace is shifted and has a similar effect to rotating the eye in the reverse direction, as shown in Figure 4.13(c). Thus the reachable areas move towards

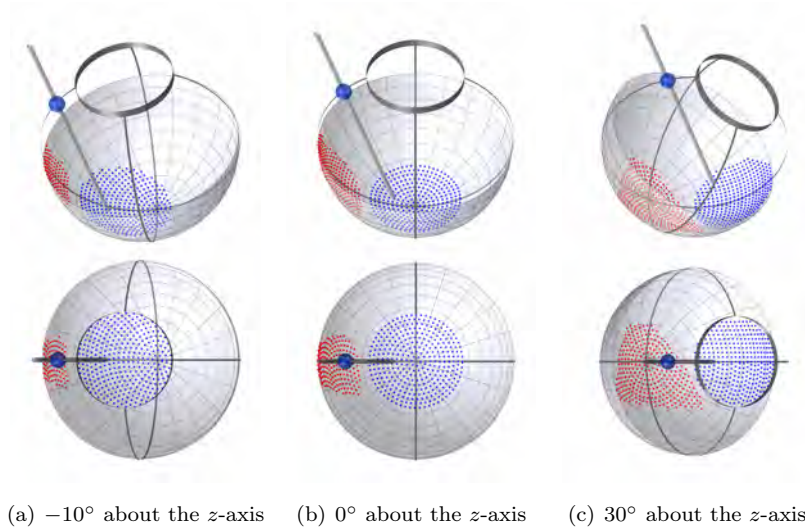


Figure 4.14: Reachability analysis of the instrument with the eye at the zero position. (Red: Reachable Zone, Blue: Visible Zone, Green: Reachable-Visible (operation) Zone)

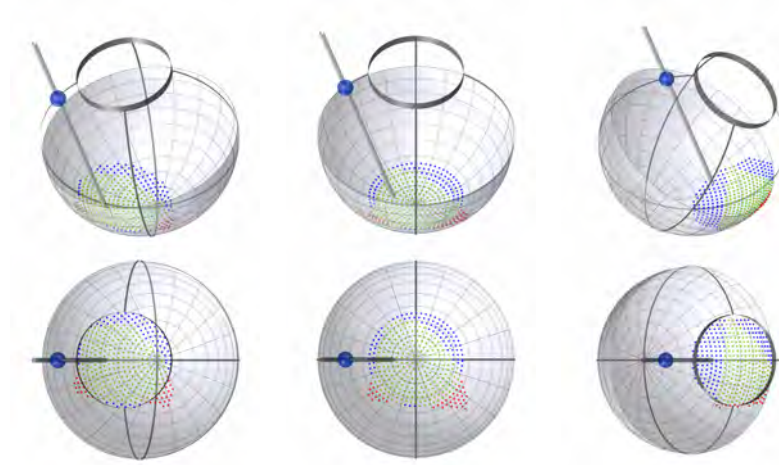
the center of the eye where they intersect with the visible area. In the experiment, tilting the robot about 30 degrees yields satisfactory results with the same offset as previously chosen. Compared to the former result where none of the reachable points are visible, the overlap of reachable and visible areas is much better by tilting the robot. Figure 4.15 shows the qualitative results with different rotations of the eye. In the following, this configuration is referred to as *reference*.

4.3.6 Comparison to Other Locations

To compare the reference with other candidates, the robot’s workspace is sampled by positioning the five actuators in 3mm steps within their working range of $\pm 15mm$. The position of the end effector is calculated via forward kinematics. This yields $11^5 = 161051$ points. To get rid of configurations that yield much worse results than the reference, the workspace is filtered by analysing the reachability of the robot without rotating the eye, while tilting the robot about the z -axis within a range of 0 – 30 degrees with 10 degree steps. Candidates that yield worse results with every progressive tilt of the robot are discarded. The filtered candidates are then more closely analysed within the full rotation range of the eye, i.e. the combination of –10 to 30 degrees about the z -axis and –10 to 10 degrees about the y -axis.

Results

In the following, the overlap of visible and reachable areas is referred to as the *coverage* or *performance*. The candidates obtained for each tilt of the robot and rotation of the eye with the best performance are chosen as the center of a sphere with diameter 10mm. Candidates



(a) -10° about the z -axis (b) 0° about the z -axis (c) 30° about the z -axis

Figure 4.15: Reachability analysis with 30 degrees tilt of the robot, which is set as *reference*. (Red: Reachable Zone, Blue: Visible Zone)

within this neighbourhood are further considered in the analysis and are illustrated in Figure 4.16 within the workspace. The exact locations of the candidates with the best performance are listed in Table 4.2. Figure 4.17(a) shows the best and worst performance of candidates within each neighbourhood. Figure 4.17(b) illustrates the average coverage and the standard deviation for each configuration within the region of interest. The results are summarized in Table 4.3. All values correspond to the mean percentage of overlap of visible and reachable points for all configurations of the eye considered.

As the results show, the maximum coverage of the reference is similar to those obtained in the analysis. However, the deviation is higher and at worst only a coverage of around 44% is obtained, implying that the region around the reference is more volatile. This is crucial in a practical setting where the location of the eye cannot be positioned exactly at the desired coordinates and its parameters may change from patient to patient. Thus the regions of interest obtained in the analysis are very helpful. Figure 4.18 illustrates the performance of the best eye location with 0 degrees tilt of the robot qualitatively.

Table 4.2: Coordinates of the candidates with the best performance in each tilt configuration and the reference location.

	ref	0°	10°	20°	30°
x	-54.19	-22.19	-31.15	-39.84	-46.96
y	82.50	104.68	98.62	90.03	78.66
z	54.50	55.90	55.83	55.90	56.10

4. KINEMATICS

Table 4.3: Quantitative results of the analysis.

	ref	0°	10°	20°	30°
Mean	0.66	0.80	0.88	0.91	0.91
Deviation	0.11	0.03	0.02	0.03	0.02
Max	0.89	0.84	0.93	0.95	0.95
Min	0.44	0.71	0.81	0.84	0.85

4.3.7 Experimental Evaluation

The improved model and its results are evaluated experimentally using the simulation environment. For this, three of the previously determined locations of the eye are chosen

- the reference position determined by observation
- the optimal location of the eye without tilting the robot
- the optimal location which yielded the best overall results, in the case tilting the robot by about 20 degrees

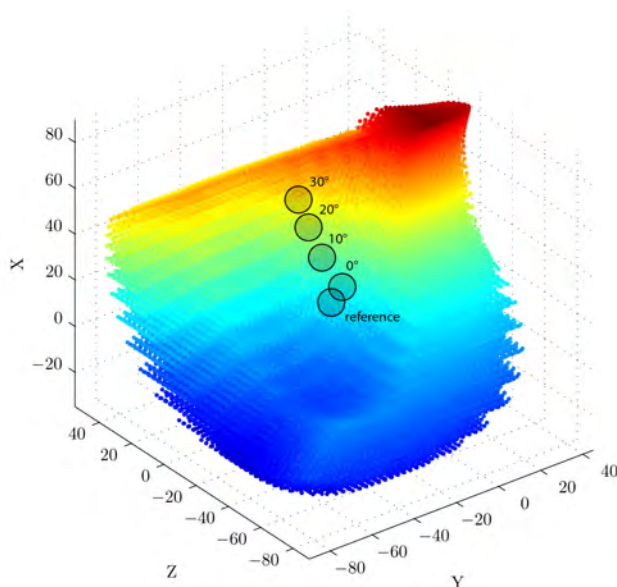
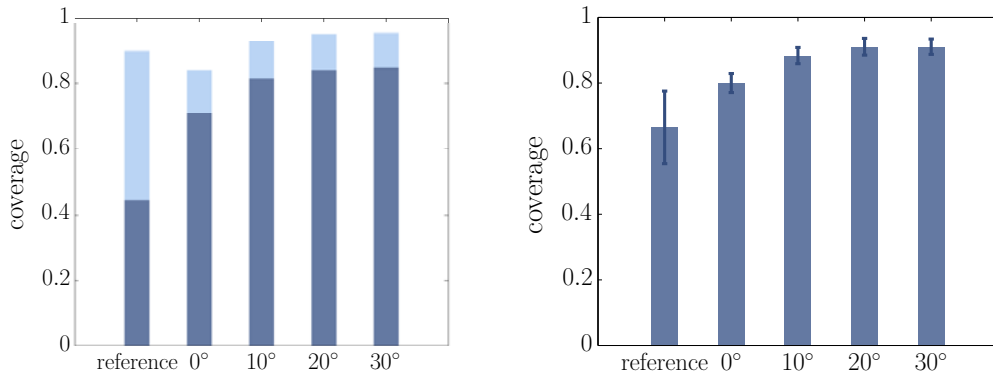


Figure 4.16: Locations of the candidates with the best performance for every tilt and the reference within the workspace. The circles indicate the spherical neighbourhood. The origin of the coordinate frame is the tip of the needle in zero position, which coincides with the location of the reference.



(a) Best end worst performance of candidates within the spherical neighbourhood (b) Average performance of candidates within the neighbourhood and their standard deviation

Figure 4.17: Results of the performance of candidates within the region of interest in comparison to the reference.

For each location, the area that can be reached by the tool is examined. For three rotations of the eye about the z -axis: -10 , 0 and 30 degrees. A simulation is run where the eye is placed at the calculated offset and the robot is tilted about the z -axis. The robot is controlled via the 3D mouse and at the beginning the tip of the instrument is placed where the cannula is supposed to be inserted. This position is indicated by a blue ring on the 3D model of the eye. For the -10 and 30 degrees configuration, the eye must first be rotated about the z -axis before the RCM is set. It should be mentioned that the RCM is set manually, which inhibits placing it exactly at the position where the maximum coverage could be obtained. After fixing the RCM the needle is inserted into the eye and moved in all directions at an offset from the retina as far as possible. The positions are recorded and it is indicated whether the retina can be touched with the current orientation of the robot. Also, the actual limits of the linear positioners are considered. These are slightly different from those assumed in the former section and are set to

$$L_1, L_2 \in [-14.5, 12.5], L_3, L_4 \in [-13, 14.5], L_5 \in [-13.5, 14.5] \quad (4.18)$$

One experiment which is performed to determine the optimal position without tilting the robot and zero rotation of the eye is shown in Figure 4.19. The red area indicates the positions on the retina that can be reached. This procedure is repeated for all configurations listed above, including rotations of the eye about the z -axis with -10 , 0 and 30 degrees. Then the area which was reached during the experiment is compared to the prediction from the model as presented in the former section. For simplicity, the areas are projected onto a plane.

4. KINEMATICS

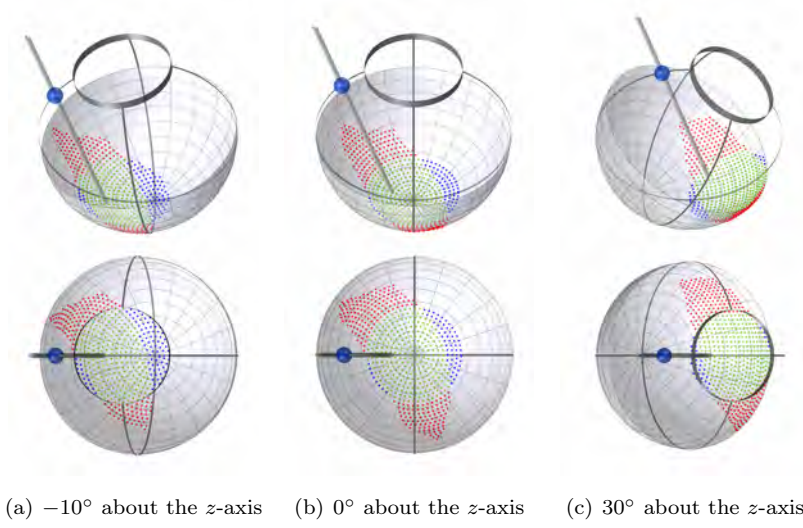


Figure 4.18: Best result for the reachability with 0 degrees tilt of the robot. (Red: Reachable Zone, Blue: Visible Zone, Green: Reachable-Visible (operation) Zone)

The following indicators are used to quantitatively assess the results:

- Overlap of reachable areas r :

$$o_r = \frac{M_r \cap E_r}{M_r \cup E_r} \quad (4.19)$$

where M_r defines the reachable area predicted by the model M and E_r the area reached during the experimental run E .

- Overlap of visible and reachable areas rv :

$$o_{rv} = \frac{M_{rv} \cap E_{rv}}{M_{rv} \cup E_{rv}} \quad (4.20)$$

where M_{rv} defines the reachable and visible area predicted by the model and E_{rv} the area that was seen and reached during the experimental run.

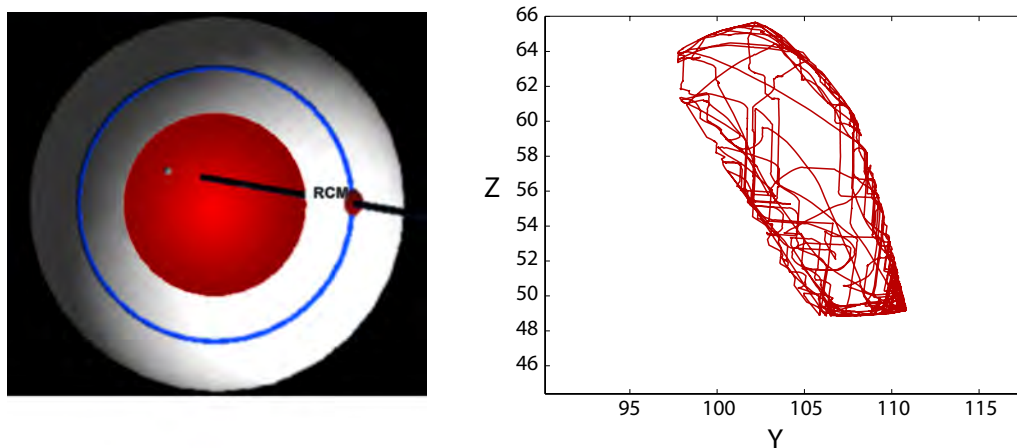
- Ratio of the M_{rv} to visible area for the model:

$$v_M = \frac{M_{rv}}{V} \quad (4.21)$$

where V defines the visible area seen through the microscope as defined in the previous section.

- Ratio of the visible area and E_{rv} for the experimental run:

$$v_E = \frac{E_{rv}}{V} \quad (4.22)$$



(a) Experimental run in the simulation environment. The grey dot indicates the point on the retina the tool is aimed at

(b) Recorded trajectory of reachable points on the retina from one experimental run. The shaded region indicates the reachable area derived from the trajectory

Figure 4.19: One experimental run for the best position without tilting the robot and no rotation of the eye.

The first two indicators yield information about how well the model predicts the reachability. The last two ratios give more detail about the overall quality of the position of the eye. Figure 4.20 shows the planar projection of the areas on the retina for the best position of the eye with no tilt of the robot for each rotation considered. It also illustrates the areas that are evaluated by the listed indicators. Tables 4.4, 4.5 and 4.6 show the related quantitative results for all configurations evaluated.

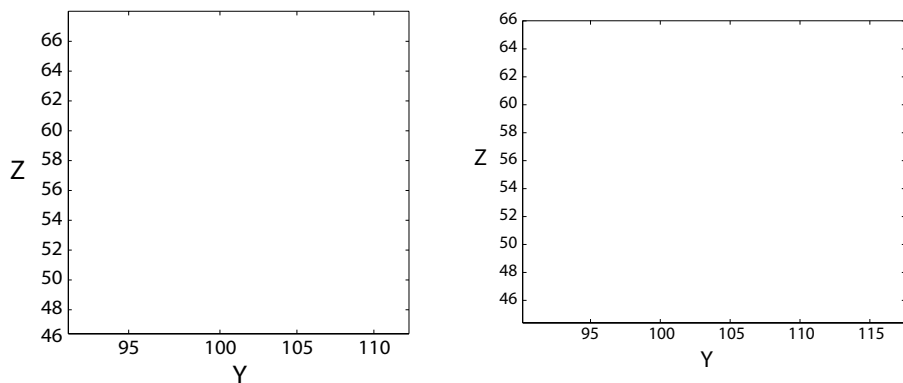
Table 4.4: Evaluation results without tilting the robot.

	-10°	0°	30°	avg.
o_r	0.69	0.71	0.76	0.72
o_{rv}	0.84	0.86	0.92	0.87
v_M	0.76	0.87	0.69	0.77
v_E	0.63	0.74	0.63	0.67

Discussion

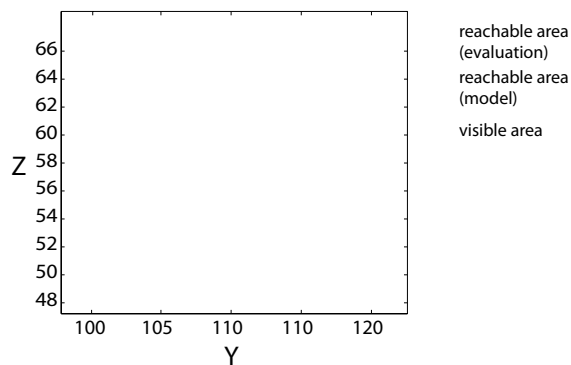
The difference between the prediction of the model and the experimental run are most evident for the overlap of reachable areas o_r . Firstly, this can be attributed to the fact that the actual limits of the robot are smaller than those assumed in the model. Secondly, as Figure 4.20 illustrates, the reachable areas during the experimental run do not necessarily lie within the

4. KINEMATICS



(a) -10° rotation of the eye about the z -axis

(b) 0° about the z -axis



(c) 30° about the z -axis

Figure 4.20: The visible and reachable areas for the best location of the eye without tilting the robot predicted by the model and determined during the experimental run. Quantitative results are listed in Table 4.4.

area predicted by the model. This is because the location of the RCM during an experimental

Table 4.5: Evaluation results with tilting the robot about 20 degrees.

	-10°	0°	30°	avg.
o_r	0.78	0.85	0.77	0.80
o_{rv}	0.89	0.94	0.99	0.94
v_M	0.89	0.97	0.95	0.94
v_E	0.81	0.89	0.87	0.86

run cannot be placed exactly on the surface of the eye, because of the eye rotation is controlled manually. This is not the case with the model. The overlap of reachable and visible areas is

more consistent, because differences of the limits of the actuators do not affect central positions so much. Looking at the percentage of reachable areas within the visible area v_M and v_E , the model yields better results than those obtained during the experimental run. Clearly, this is also due to the smaller ranges of the positioners. Furthermore, because the RCM is set manually and used as an input for the model as well, the coverage reached in the model is not the maximum. Nevertheless, the evaluation shows that the model is consistent and satisfactory results can be achieved.

4.4 Results

This chapter presented the design of the robot using the requirements defined in previous chapter. In Section 4.3.4, the robot is analyzed with respect to its reachability within the eye. The best position of the eye for maximizing the area on the retina that can be reached with the tool was determined. This is essential for practical integration of the setup into conventional clinical procedure. In an experimental evaluation with the simulation environment the consistency of the results is examined. In Section 8.4.2 the overall approach and implementation will be evaluated during two experimental sessions. Several experiments using porcine eyes were conducted, which yielded valuable results. These are an important feedback for future work and improvements of the design of the robot and the approach.

Table 4.6: Evaluation results for the reference.

	-10°	0°	30°	avg.
o_r	0.81	0.82	0.81	0.81
o_{rv}	0.92	0.89	0.90	0.90
v_M	0.80	0.75	0.72	0.76
v_E	0.79	0.69	0.66	0.71

4. KINEMATICS

Chapter 5

Dynamics

When studying the dynamics of a mechanical system, one usually considers one of two famous methods: the Newton-Euler method and Lagrange’s method. Lagrange’s method has the advantage of being very general: the system doesn’t even have to be mechanical. It could also account for flexible mechanisms (if their behavior can be represented in the kinetic energy function that is required for Lagrange’s method). A derivation of the mechanism’s dynamics using Lagrange’s method can be found in [84].

While only applicable to rigid multi-body systems, the Newton-Euler method offers the following advantages to Lagrange’s method in the domain of rigid multi-body systems:

- Fewer “points of failure” at the beginning: While Lagrange’s method depends on the selection of a correct energy function at the beginning, the Newton-Euler method requires only position vectors of all bodies in absolute coordinates and all forces and torques acting on each body.
- More transparency: The physical meaning of each term is clearer than in Lagrange’s method, where one mostly deals with various differentiations of the Lagrangian. Consequently, it makes the equations easier to verify.
- Easier to automate: The literature contains various derivations of recursive Newton-Euler algorithms that can be implemented on a computer. However, one doesn’t necessarily need to resort to such derivation when trying to implement the algorithms. A somewhat “semi-automatic” implementation that follows the method as explained.

Simplifications: Strictly speaking, the robot has *seven* rigid bodies, each one with its distinct mass and moment of inertia:

- The beams of linear joints l_1 and l_2 .
- The end effector of the first PCJM.

5. DYNAMICS

- The beams of linear joints l_3 and l_4 .
- The end effector of the second PCJM.
- The robot's tool tip (end effector of the final linear joint l_5).

Considering the masses and inertias of each PCJM's linear joints themselves would require introducing additional position vectors for their respective centers of gravity as well as their own coordinate frames and distinct Jacobians. Assuming that their masses are at least two orders of magnitude lower than the mass of a PCJM end effector, let alone the whole robot, it would mean introducing a lot of effort to remove a small error. Small discrepancies like that can be compensated by a well thought-out control law.

In this chapter the dynamic behavior of the robot will be investigated by first analyzing the dynamic behavior of a single PCJM and then analyzing the serial configuration.

5.1 Dynamic Analysis of a PCJM

Assumptions: Here a PCJM is considered in which its end effector is displaced by some distance d_2 from the center of rotation. Consequently, rotating by an angle α results in a non-zero positional displacement along the y-axis. The position in x- and y-axis and the angle α are of interest; the goal is to move the system into a desired configuration.

Position and acceleration of the end effector: Let the end effector's position in cartesian coordinates would be:

$$\mathbf{r} = \begin{bmatrix} a \\ d_2 \sin(\alpha) \end{bmatrix} \quad (5.1)$$

Here, the x-position is:

$$a = \frac{1}{2}(l_1 + l_2) + d_2 \cos(\alpha)$$

Differentiating \mathbf{r} twice yields:

$$\ddot{\mathbf{r}} = \begin{bmatrix} \ddot{a} \\ d_2 \cos(\alpha)\ddot{\alpha} - d_2 \sin(\alpha)\dot{\alpha}^2 \end{bmatrix} \quad (5.2)$$

Using the Newton-Euler method, the PCJM's dynamic equations are therefore derived. These will later be used to derive a linearization function that transforms the system into a simple double-integrator for which a controller can readily be found by pole placement.

Forces and torques: Let u_1 and u_2 be the *forces* exerted along the two prismatic joints l_1 and l_2 . The total force exerted by these joints along the x-axis is $u_1 + u_2$, and along the y-axis, gravity influences the system. This forms the vector:

$$\mathbf{u} = \begin{bmatrix} u_1 + u_2 \\ m \cdot g \end{bmatrix}$$

According to Newton:

$$m \cdot \ddot{\mathbf{r}} - \mathbf{u} = 0$$

Next, a set of *natural coordinates* for our system need to be chosen. a is desired, the position along the x-axis and α , the angle. Therefore:

$$\mathbf{q} = \begin{bmatrix} a \\ \alpha \end{bmatrix}$$

The *translational Jacobian* J_T is then:

$$J_T = \frac{\partial \mathbf{r}}{\partial \mathbf{q}} = \begin{bmatrix} 1 & 0 \\ 0 & d_2 \cos(\alpha) \end{bmatrix}$$

The sum of the torques which are present in the center of rotation between the two prismatic joints are, according to Euler, proportional to the acceleration of α :

$$I\ddot{\alpha} = \left[\frac{d}{2} + d_2 \sin(\alpha) \right] u_1 - \left[\frac{d}{2} + d_2 \sin(\alpha) \right] u_2$$

The *rotational Jacobian* J_R is:

$$J_R = \frac{\partial \alpha}{\partial \mathbf{q}} = \begin{bmatrix} 0 & 1 \end{bmatrix}$$

The method of Newton-Euler allows projection of Newton and Euler equations into the space of natural coordinates, as defined above by the vector \mathbf{q} , using the transposed translational and rotational Jacobians:

$$\begin{aligned} J_T^T (m \cdot \ddot{\mathbf{r}} - \mathbf{u}) &= 0 \\ J_R^T \left(I\ddot{\alpha} - \begin{bmatrix} \frac{d}{2} + d_2 \sin(\alpha) \\ -\frac{d}{2} - d_2 \sin(\alpha) \end{bmatrix} \mathbf{u} \right) &= 0 \end{aligned}$$

Combining the above equations to two equations gives the PCJM's dynamic equations:

$$\begin{aligned} m\ddot{a} - (u_1 + u_2) &= 0 \\ d_2 \cos(\alpha) [m d_2 \cos(\alpha) \ddot{\alpha} - m d_2 \sin(\alpha) \dot{\alpha}^2] - m d_2 \cos(\alpha) g + I\ddot{\alpha} - m \left(-\frac{d}{2} - d_2 \sin(\alpha) \right) g &= 0 \end{aligned}$$

Standard form for second-order mechanical systems: Next, these equations must be rewritten in the standard form (see section 5.2 for further details):

$$\mathbf{u} = M(\mathbf{q})\ddot{\mathbf{q}} + C(\mathbf{q}, \dot{\mathbf{q}})\dot{\mathbf{q}} + G(\mathbf{q}) \quad (5.3)$$

To form the mass matrix $M(\mathbf{q})$, all those terms from the dynamic equations which are multiplied by \ddot{a} or $\ddot{\alpha}$ (which are the elements of $\ddot{\mathbf{q}}$) need to be considered:

$$M(\mathbf{q}) = \begin{bmatrix} m & 0 \\ 0 & I + m \cdot d_2^2 \cdot \cos(\alpha) \cos(\alpha) \end{bmatrix}$$

5. DYNAMICS

$G(\mathbf{q})$ consists of all terms containing the gravity acceleration g :

$$G(\mathbf{q}) = \begin{bmatrix} 0 \\ [m \cdot d_2 \cos(\alpha) + \frac{m d}{2} + m \cdot d_2 \sin(\alpha)]g \end{bmatrix}$$

The remaining terms form the centrifugal and Coriolis terms:

$$C(\mathbf{q}, \dot{\mathbf{q}}) = \begin{bmatrix} 0 \\ m \cdot d_2^2 \cdot \cos(\alpha) \sin(\alpha) \dot{\alpha}^2 \end{bmatrix}$$

5.1.1 Position and Orientation Control

The Newton-Euler method requires that the system be brought into the form:

$$\dot{\mathbf{x}} = \mathbf{a}(\mathbf{x}) + \mathbf{b}(\mathbf{x})\mathbf{u}$$

where $\mathbf{u} = [u_1, u_2]^T$ is the *input force and torque vector*. To achieve this, define $\tilde{\mathbf{q}} := \dot{\mathbf{q}}$. Then, Equation (5.3) becomes:

$$M(\mathbf{q})\dot{\tilde{\mathbf{q}}} + C(\mathbf{q}, \tilde{\mathbf{q}})\tilde{\mathbf{q}} + G(\mathbf{q}) = \mathbf{u}$$

which can be solved for $\tilde{\mathbf{q}}$ to achieve the desired form:

$$\begin{aligned} M(\mathbf{q})\dot{\tilde{\mathbf{q}}} &= \mathbf{u} - C(\mathbf{q}, \tilde{\mathbf{q}})\tilde{\mathbf{q}} - G(\mathbf{q}) \\ \Leftrightarrow \dot{\tilde{\mathbf{q}}} &= M(\mathbf{q})^{-1}(\mathbf{u} - C(\mathbf{q}, \tilde{\mathbf{q}})\tilde{\mathbf{q}} - G(\mathbf{q})) \\ &= M(\mathbf{q})^{-1}\mathbf{u} - M(\mathbf{q})^{-1}(C(\mathbf{q}, \tilde{\mathbf{q}})\tilde{\mathbf{q}} + G(\mathbf{q})) \end{aligned}$$

With the state $\mathbf{x} := [\tilde{\mathbf{q}}, \mathbf{q}]^T$, the system dynamics can be re-stated as:

$$\begin{aligned} \dot{\mathbf{x}} &= \begin{bmatrix} \tilde{\mathbf{q}} \\ M(\mathbf{q})^{-1}(\mathbf{u} - C(\mathbf{q}, \tilde{\mathbf{q}})\tilde{\mathbf{q}} - G(\mathbf{q})) \end{bmatrix} \\ &= \begin{bmatrix} \dot{\alpha} \\ \dot{\alpha} \\ \frac{1}{m}u_1 \\ -\frac{1}{d_2^2 \cdot m \cos(\alpha)^2 + I} (\dot{\alpha}^2 \cdot d_2^2 m \sin(\alpha) \cos(\alpha) + d_2 g m (\sin(\alpha) + \cos(\alpha)) + \frac{1}{2} d_2 g m - u_2) \end{bmatrix} \quad (5.4) \\ &= \underbrace{\begin{bmatrix} \dot{\alpha} \\ \dot{\alpha} \\ 0 \\ \frac{\dot{\alpha}^2 \cdot d_2^2 m \sin(\alpha) \cos(\alpha) + d_2 g m (\sin(\alpha) + \cos(\alpha)) + \frac{1}{2} d_2 g m}{d_2^2 \cdot m \cos(\alpha)^2 + I} \end{bmatrix}}_{\mathbf{a}(\mathbf{x})} + \underbrace{\begin{bmatrix} 0 & 0 \\ 0 & 0 \\ \frac{1}{m} & 0 \\ 0 & -\frac{1}{d_2^2 \cdot m \cos(\alpha)^2 + I} \end{bmatrix}}_{\mathbf{b}(\mathbf{x})} \mathbf{u} \end{aligned}$$

with the inverse mass matrix:

$$M(\mathbf{q})^{-1} = \begin{bmatrix} \frac{1}{m} & 0 \\ 0 & \frac{1}{d_2^2 m \cos(\alpha)^2 + I} \end{bmatrix}$$

5.1.2 Feedback Linearization of the PCJM

Now, Feedback Linearization can be applied to the system (5.4). The system's *output* equation was chosen as follows:

$$y = \begin{bmatrix} a \\ \alpha \end{bmatrix}$$

Subsequent Lie differentiation of the output yields:

$$\begin{aligned} L_a y &:= \frac{\partial y}{\partial \mathbf{x}} \dot{\mathbf{x}} = \frac{\partial y}{\partial \mathbf{x}} [a(\mathbf{x}) + b(\mathbf{x})\mathbf{u}] \\ &= L_a y + L_b y \mathbf{u} \\ &= \frac{\partial y}{\partial \mathbf{x}} a(\mathbf{x}) \\ &= \begin{bmatrix} 1 & 0 & 0 & 0 \\ 0 & 1 & 0 & 0 \end{bmatrix} \cdot \begin{bmatrix} \dot{a} \\ \dot{\alpha} \\ 0 \\ \frac{\dot{\alpha}^2 \cdot d_2^2 m \sin(\alpha) \cos(\alpha) + d_2 g m (\sin(\alpha) + \cos(\alpha)) + \frac{1}{2} d_2 g m}{d_2^2 \cdot m \cos(\alpha)^2 + I} \end{bmatrix} = \begin{bmatrix} \dot{a} \\ \dot{\alpha} \end{bmatrix} \end{aligned}$$

The input doesn't yet appear in the output's Lie derivative. So, another differentiation is needed. The second Lie derivatives are:

$$\begin{aligned} L_a^2 y &= \frac{\partial L_a y}{\partial \mathbf{x}} \dot{\mathbf{x}} = \frac{\partial L_a y}{\partial \mathbf{x}} [a(\mathbf{x}) + b(\mathbf{x})\mathbf{u}] \\ &= \begin{bmatrix} 0 & 0 & 1 & 0 \\ 0 & 0 & 0 & 1 \end{bmatrix} \cdot [a(\mathbf{x}) + b(\mathbf{x})\mathbf{u}] \\ &= \underbrace{\begin{bmatrix} 0 \\ \frac{\dot{\alpha}^2 \cdot d_2^2 m \sin(\alpha) \cos(\alpha) + d_2 g m (\sin(\alpha) + \cos(\alpha)) + \frac{1}{2} d_2 g m}{d_2^2 \cdot m \cos(\alpha)^2 + I} \end{bmatrix}}_{:=f(\mathbf{x})} + \underbrace{\begin{bmatrix} \frac{1}{m} & 0 \\ 0 & -\frac{1}{d_2^2 \cdot m \cos(\alpha)^2 + I} \end{bmatrix}}_{:=D(\mathbf{x})} \mathbf{u} \end{aligned}$$

The system has two dimensions, therefore the linearization is complete and there are no internal dynamics. $D(\mathbf{x})$ is called the *decoupling matrix*. Suppose output y needs to match some desired position – which also implies a desired acceleration for y . Then the equations above define how \ddot{y} , the acceleration of the output, depends on the joint accelerations \mathbf{u} . Formally, the goal is:

$$\ddot{y} = \mathbf{r} \quad (5.5)$$

where \mathbf{r} is the aforementioned desired acceleration vector. Eq. 5.5 can be rewritten as:

$$f(\mathbf{x}) + D(\mathbf{x})\mathbf{u} = \mathbf{r} \quad (5.6)$$

Solving Eq. 5.6 for \mathbf{u} yields the control law for \mathbf{u} which sets the output's acceleration to \mathbf{r} :

$$\begin{aligned} \mathbf{r} - f(\mathbf{x}) &= D(\mathbf{x})\mathbf{u} \\ \mathbf{u} &= D(\mathbf{x})^{-1}[\mathbf{r} - f(\mathbf{x})] \\ &= \begin{bmatrix} m & 0 \\ 0 & -d_2^2 \cdot m \cos(\alpha)^2 + I \end{bmatrix} \left(\mathbf{r} - \begin{bmatrix} 0 \\ \frac{\dot{\alpha}^2 \cdot d_2^2 m \sin(\alpha) \cos(\alpha) + d_2 g m (\sin(\alpha) + \cos(\alpha)) + \frac{1}{2} d_2 g m}{d_2^2 \cdot m \cos(\alpha)^2 + I} \end{bmatrix} \right) \end{aligned}$$

5. DYNAMICS

from which it is seen, that the decoupling matrix has to be invertible for this transformation to be valid. The determinant of $D(\mathbf{x})$ is:

$$\det(D(\mathbf{x})) = -\frac{1}{(d_2^2 \cdot m \cos(\alpha)^2 + I)m} \neq 0 \quad (5.7)$$

Roughly speaking, the nonlinear terms of the system are *canceled out* by this transformation and the system is now a simple double-integrator, as shown in Equation 5.5.

5.1.3 A control law for the PCJM

Putting together the results of the feedback linearization and a state feedback control law which is determined by pole placement a control law for the parallel-coupled joint mechanism is stated:

$$\mathbf{u}(w_1, w_2) = \begin{bmatrix} m & 0 \\ 0 & -d_2^2 \cdot m \cos(\alpha)^2 + I \end{bmatrix} \begin{bmatrix} -[k_1, k_2] \begin{bmatrix} a \\ \dot{a} \end{bmatrix} + f_1 w_1 \\ -[k_3, k_4] \begin{bmatrix} \alpha \\ \dot{\alpha} \end{bmatrix} + f_2 w_2 \end{bmatrix} \quad (5.8)$$

$$- \begin{bmatrix} 0 \\ \frac{\dot{\alpha}^2 \cdot d_2^2 m \sin(\alpha) \cos(\alpha) + d_2 g m (\sin(\alpha) + \cos(\alpha)) + \frac{1}{2} d_2 g m}{d_2^2 \cdot m \cos(\alpha)^2 + I} \end{bmatrix}$$

where w_1 and w_2 are the desired stationary positions. The parameters $k_3 - k_4$, and $f_3 - f_4$ determined in the same way as $k_1 - k_2$ and $k_3 - k_4$ respectively.

Stability: The stability of the control law (5.8) depends on two issues:

- The validity of the nonlinear system's inversion (5.1.2). This can be checked by verifying that the inverse decoupling matrix $D(\mathbf{x})^{-1}$ stays invertible at all times. Usually, this breaks down at singularities.
- The stability of the linear control law, which can be checked by verifying that the Eigen value stay in the left half-plane.

Referring to basic linear algebra, a matrix is invertible if its determinant is nonzero. Equation (5.7) illustrates two reasons why this case never occurs:

1. The function $f(x) = -\frac{1}{x}$ has no zeros for $x \in (-\infty, \infty)$.
2. The denominator $(d_2^2 \cdot m \cos(\alpha) + I)m$ can only be zero for systems that have no mass ($m = 0$), which is impossible for any real mechanical system.

The linear control law is designed using the technique of pole placement, where the eigenvalues of the closed-loop system are chosen by the control law designer. Naturally, eigenvalues with negative real parts are chosen, since it is the goal to design a control law which stabilizes the system.

Discussion of the control law: In the feedback linearization section it is seen that the order of the differential equation is equal to the dimensions of the system. The state feedback control law stabilizes the double integrator that results from the inversion, described in Equation (5.1.2), asymptotically since it moves the integrator's eigenvalues into the left complex half-plane. The larger the eigenvalues' real components, the better the ability to compensate for imperfect parameter estimates, like mass or moment of inertia in the inversion (5.1.2). However, the downside of this is that it also makes the closed-loop system jerkier and move *faster*. In a delicate eye surgery situation, this can be a severe problem. So, one has to either provide *very precise* estimates of mass and moment of inertia, in order to choose reasonably large gains, or propagate the input accelerations through a *pre-filter* before applying them onto the joints of the system.

Roughly speaking, the idea is to specify a *reference* PT2 system

$$G^r(s) = \frac{1}{s^2 + T_1 s + T_2} \quad (5.9)$$

with the desired gains T_1 and T_2 (which would lead to a sufficiently slow moving system). Since the input accelerations are integrated twice by this system, one needs to differentiate the pre-filter's output twice to obtain the desired accelerations.

5.2 Dynamic Analysis of the robot

To derive the dynamic equations of the serial configuration of the robot, its joint space is chosen as generalized coordinates. Therefore, $\mathbf{q} = [L1, L2, L3, L4, L5]^T$, a vector of all joint positions, is a vector of generalized coordinates.

The aim is to derive a description of the robot's dynamics as a second-order mechanical system of the form

$$M(\mathbf{q})\ddot{\mathbf{q}} + C(\mathbf{q}, \dot{\mathbf{q}})\dot{\mathbf{q}} + g(\mathbf{q}) = \mathbf{u} \quad (5.10)$$

where $M(\mathbf{q})$ is the system's mass matrix, $C(\mathbf{q}, \dot{\mathbf{q}})$ are the centrifugal and Coriolis terms and $g(\mathbf{q})$. The gravitational term u is the influence of external forces and moments, translated into generalized coordinates, e.g. as shown above. To examine free motions of the system, set $\mathbf{u} = 0$.

The terms $C(\mathbf{q}, \dot{\mathbf{q}})$ can be derived from $M(\mathbf{q})$ by determining the mass matrix's Christoffel symbols and $g(\mathbf{q})$ is constructed by determining all partial derivatives of some potential function $U(x)$ w.r.t. the generalized coordinates \mathbf{q} . Usually, this is the influence of gravity. The robot's kinetic energy is given by:

$$E_{kin} = \frac{1}{2} \dot{\mathbf{q}}^T M(\mathbf{q}) \dot{\mathbf{q}} \quad (5.11)$$

Therefore, determining the mass matrix is basically the same as determining the kinetic energy from all linear and angular velocities that occur in the system. The PCJMs contribute both a linear and an angular component. The final single prismatic joint only contributes a linear component.

5. DYNAMICS

The Mass Matrix In total, the following parameters of the robot are required and thereby have been computed:

- The *masses* m_b , m_c and m_E of the second PCJM, the single prismatic joint, the end effector and their respective *centers of gravity* (These are needed to determine $g(\mathbf{q})$).
- The *inertia tensors* I_{Kb} and I_{Kc} of the second PCJM's base and the single prismatic joint's base, aligned along their respective bodies' principal axes, i.e.

$$I_{Kb} = \begin{bmatrix} I_{bx} & 0 & 0 \\ 0 & I_{by} & 0 \\ 0 & 0 & I_{bz} \end{bmatrix}, \quad I_{Kc} = \begin{bmatrix} I_{cx} & 0 & 0 \\ 0 & I_{cy} & 0 \\ 0 & 0 & I_{cz} \end{bmatrix} \quad (5.12)$$

- the following translational Jacobians:

$$J_{Ta} = \begin{bmatrix} 1/2 & 1/2 & 0 & 0 & 0 \\ 0 & 0 & 0 & 0 & 0 \\ 0 & 0 & 0 & 0 & 0 \\ 0 & 0 & 0 & 0 & 0 \\ 0 & 0 & 0 & 0 & 0 \end{bmatrix}, \quad J_{Tb} = \begin{bmatrix} 0 & 0 & 0 & 0 & 0 \\ 0 & 0 & 0 & 0 & 0 \\ 1/2 & 1/2 & 0 & 0 & 0 \\ 0 & 0 & 0 & 0 & 0 \\ 0 & 0 & 0 & 0 & 0 \end{bmatrix}, \quad J_{Tc} = \begin{bmatrix} 0 & 0 & 0 & 0 & 0 \\ 0 & 0 & 0 & 0 & 0 \\ 0 & 0 & 0 & 0 & 0 \\ 0 & 0 & 0 & 0 & 0 \\ 0 & 0 & 0 & 0 & 1 \end{bmatrix}, \quad (5.13)$$

- the following rotational Jacobians (mapping from $[L1, L2, L3, L4, L5]$ to $[L_a, \theta_a, L_b, \theta_b, L5]$):

$$J_{Ra} = \begin{bmatrix} 0 & 0 & 0 & 0 & 0 \\ -\frac{1}{d\rho_{12}^2} & \frac{1}{d\rho_{12}^2} & 0 & 0 & 0 \\ 0 & 0 & 0 & 0 & 0 \\ 0 & 0 & 0 & 0 & 0 \\ 0 & 0 & 0 & 0 & 0 \end{bmatrix}, \quad J_{Rb} = \begin{bmatrix} 0 & 0 & 0 & 0 & 0 \\ 0 & 0 & 0 & 0 & 0 \\ 0 & 0 & 0 & 0 & 0 \\ -\frac{1}{d\rho_{34}^2} & \frac{1}{d\rho_{34}^2} & 0 & 0 & 0 \\ 0 & 0 & 0 & 0 & 0 \end{bmatrix} \quad (5.14)$$

Here, to simplify the calculation, ρ_{12} and ρ_{34} are defined as:

$$\rho_{ij} := \sqrt{1 + \frac{(L_j - L_i)^2}{d^2}} \quad (5.15)$$

For $L3$ and $L4$, the mass matrix can be constructed as follows:

$$M(\mathbf{q}) = m_b(J_{Ta}^T J_{Ta}) + J_{Ra}^T(\mathbb{I}_a)J_{Ra}^T + m_c(J_{Tb}^T J_{Tb}) + J_{Rb}^T(\mathbb{I}_b)J_{Rb}^T + m_E(J_{Tc}^T J_{Tc}) \quad (5.16)$$

and the configuration-dependent inertia tensors \mathbb{I}_a and \mathbb{I}_b are:

$$\mathbb{I}_a = R(\theta_a)I_{Ka}R(\theta_a)^T, \quad \mathbb{I}_b = R(\theta_a, \theta_b)I_{Kb}R(\theta_a, \theta_b)^T \quad (5.17)$$

The rotation matrices $R(\theta_a)$ and $R(\theta_a, \theta_b)$ are known from the forward kinematics:

$$R(\theta_a, \theta_b) = \begin{bmatrix} -\frac{(L_3-L_4)(L_1-L_2)}{d^2\rho_{12}\rho_{34}} & \frac{1}{\rho_{12}} & \frac{L_1-L_2}{d\rho_{12}\rho_{34}} \\ -\frac{L_3-L_4}{d\rho_{12}\rho_{34}} & -\frac{L_1-L_2}{d\rho_{12}} & \frac{1}{\rho_{12}\rho_{34}} \\ \frac{1}{\rho_{34}} & 0 & \frac{L_3-L_4}{d\rho_{34}} \end{bmatrix}, \quad R(\theta_a) = \begin{bmatrix} \frac{1}{\rho_{12}} & \frac{L_1-L_2}{d\rho_{12}} & 0 \\ -\frac{L_1-L_2}{d\rho_{12}} & \frac{1}{\rho_{12}} & 0 \\ 0 & 0 & 1 \end{bmatrix} \quad (5.18)$$

The rotation matrices rotate the configuration-independent inertia matrices I_{K_a} and I_{K_b} into the current (angular) configuration and thus construct the configuration-dependent inertia tensors.

The resulting matrix is:

$$M(\mathbf{q}) = \begin{bmatrix} M_{11} & M_{12} & 0 & 0 & 0 \\ M_{21} & M_{22} & 0 & 0 & 0 \\ 0 & 0 & M_{33} & M_{34} & 0 \\ 0 & 0 & M_{43} & M_{44} & 0 \\ 0 & 0 & 0 & 0 & m_E \end{bmatrix} \quad (5.19)$$

where, the matrix elements M_{ij} are

$$\begin{aligned} M_{11} = M_{22} &= \frac{1}{4}m_b + \frac{\frac{(L_1-L_2)^2 I_{bx}}{d^2 \rho_{12}^2} + \frac{I_{by}}{\rho_{12}^2}}{d^2 \rho_{12}^4} \\ M_{12} = M_{21} &= \frac{1}{4}m_b - \frac{\frac{(L_1-L_2)^2 I_{bx}}{d^2 \rho_{12}^2} + \frac{I_{by}}{\rho_{12}^2}}{d^2 \rho_{12}^4} \\ M_{33} = M_{44} &= \frac{1}{4}m_c + \frac{\frac{(L_1-L_2)^2 I_{cy}}{d^2 \rho_{12}^2} + \frac{(L_3-L_4)^2 I_{cx}}{d^2 \rho_{12}^2 \rho_{34}^2} + \frac{I_{cz}}{\rho_{12}^2 \rho_{34}^2}}{d^2 \rho_{34}^4} \\ M_{34} = M_{43} &= \frac{1}{4}m_c - \frac{\frac{(L_1-L_2)^2 I_{cy}}{d^2 \rho_{12}^2} + \frac{(L_3-L_4)^2 I_{cx}}{d^2 \rho_{12}^2 \rho_{34}^2} + \frac{I_{cz}}{\rho_{12}^2 \rho_{34}^2}}{d^2 \rho_{34}^4} \end{aligned} \quad (5.20)$$

The Centrifugal and Coriolis Terms The centrifugal and Coriolis terms can be written in terms of Christoffel symbols:

$$\begin{aligned} C(\mathbf{q}, \dot{\mathbf{q}})\dot{\mathbf{q}} &= [c_1(\mathbf{q}, \dot{\mathbf{q}}), \dots, c_n(\mathbf{q}, \dot{\mathbf{q}})]^T, \\ c_i(\mathbf{q}, \dot{\mathbf{q}}) &= \sum_{j=1}^n \left(\sum_{k=1}^n \Gamma_{ij}^k(\mathbf{q}) \dot{q}_j \dot{q}_k \right) \end{aligned} \quad (5.21)$$

with $\dot{q}_k = \dot{L}_k$, $n = 5$ in our case and $\Gamma_{jk}^i(\mathbf{q})$ being defined as follows:

$$\Gamma_{jk}^i(\mathbf{q}) = \frac{1}{2} \left(\frac{\partial M_{ij}(\mathbf{q})}{\partial q_k} + \frac{\partial M_{ik}(\mathbf{q})}{\partial q_j} - \frac{\partial M_{kj}(\mathbf{q})}{\partial q_i} \right) \quad (5.22)$$

Since $M(\mathbf{q})$ is symmetric, these can be simplified to

$$\Gamma_{jk}^i(\mathbf{q}) = \frac{\partial M_{ij}(\mathbf{q})}{\partial q_k} - \frac{1}{2} \frac{\partial M_{kj}(\mathbf{q})}{\partial q_i} \quad (5.23)$$

The Influence of the Gravity In the inertial frame, the gravity vector is defined as $\vec{g} = [0, -g_0, 0]^T$. The base of the second PCJM is located at the end effector of the first PCJM and therefore not identical to the origin of Frame D due to the displacement shown in section 4. As stated before, its mass is m_b . In Figure 4.4, it can be seen that L_{tool} is zero and that the second PCJM's x-axis is aligned with the first PCJM's z-axis. Therefore, the only displacement that needs to be considered is the distance d_b between the first PCJM's end effector's position along

5. DYNAMICS

the x-axis (of the first PCJM) and the second PCJM's center of gravity (as seen from the first PCJM's end effector). Applying kinematics, the first PCJM end effector's position is known. Modifying it, by adding said displacement d_b :

$$\begin{bmatrix} \frac{1}{2}L_1 + \frac{1}{2}L_2 - \frac{d_m+d_b}{\rho_{12}} \\ (d_m + d_b) \frac{L_2-L_1}{d\rho_{12}} \\ 0 \end{bmatrix} \quad (5.24)$$

Gravity only affects the y-component of this vector, which leads to the first part of the potential energy function U that is required to determine the effect of gravity on the system:

$$m_b g_0 (d_m + d_b) \frac{L_2 - L_1}{d\rho_{12}} \quad (5.25)$$

With d_c being the displacement of the single prismatic joint's base with respect to the second PCJM's end effector, the position of it's center of gravity is

$$\begin{bmatrix} \frac{1}{2}L_1 + \frac{1}{2}L_2 + \frac{(d_m+d_c)}{\rho_{12}} - \frac{(L_3-L_4)(L_1-L_2)(d_m+d_c)}{d^2\rho_{12}\rho_{34}} \\ -\frac{(L_1-L_2)(d_m+d_c)}{d\rho_{12}} - \frac{(L_3-L_4)(d_m+d_c)}{d\rho_{12}\rho_{34}} \\ \frac{1}{2}L_3 + \frac{1}{2}L_4 + \frac{(d_m+d_c)}{\rho_{34}} \end{bmatrix} \quad (5.26)$$

The second part required to find U is as follows:

$$m_c g_0 \left(-\frac{(L_1 - L_2)(d_m + d_c)}{d\rho_{12}} - \frac{(L_3 - L_4)(d_m + d_c)}{d\rho_{12}\rho_{34}} \right) \quad (5.27)$$

The robot's end effector is positioned at

$$\begin{bmatrix} \frac{1}{2}L_1 + \frac{1}{2}L_2 + \frac{d_m}{\rho_{12}} - \frac{(L_3-L_4)(L_1-L_2)d_m}{d^2\rho_{12}\rho_{34}} + \frac{(L_1-L_2)L_5}{d\rho_{12}\rho_{34}} \\ -\frac{(L_1-L_2)d_m}{d\rho_{12}} - \frac{(L_3-L_4)d_m}{d\rho_{12}\rho_{34}} + \frac{L_5}{\rho_{12}\rho_{34}} \\ \frac{1}{2}L_3 + \frac{1}{2}L_4 + \frac{(L_3-L_4)L_5}{d\rho_{34}} + \frac{d_m}{\rho_{34}} \end{bmatrix} \quad (5.28)$$

and thus the third part required to define U is the second element from this vector. Combining this with Equations 5.25 and 5.27 yields:

$$\begin{aligned} U &= m_b g_0 (d_m + d_b) \frac{L_2 - L_1}{d\rho_{12}} \\ &+ m_c g_0 \left(-\frac{(L_1 - L_2)(d_m + d_c)}{d\rho_{12}} - \frac{(L_3 - L_4)(d_m + d_c)}{d\rho_{12}\rho_{34}} \right) \\ &+ m_E g_0 \left(-\frac{(L_1 - L_2)d_m}{d\rho_{12}} - \frac{(L_3 - L_4)d_m}{d\rho_{12}\rho_{34}} + \frac{L_5}{\rho_{12}\rho_{34}} \right) \end{aligned} \quad (5.29)$$

Differentiating with respect to the generalized coordinates \mathbf{q} yields:

$$g(\mathbf{q}) = \frac{\partial U}{\partial \mathbf{q}} = \begin{bmatrix} -\frac{(d_c+d_m)g_0 m_c}{d\rho_{12}} - \frac{(d_b+d_m)g_0 m_b}{d\rho_{12}} - \frac{d_m g_0 m_E}{d\rho_{12}} \\ \frac{(d_c+d_m)g_0 m_c}{d\rho_{12}} + \frac{(d_b+d_m)g_0 m_b}{d\rho_{12}} + \frac{d_m g_0 m_E}{d\rho_{12}} \\ -\frac{(d_c+d_m)g_0 m_c}{d\rho_{12}\rho_{34}} - \frac{d_m g_0 m_E}{d\rho_{12}\rho_{34}} \\ \frac{(d_c+d_m)g_0 m_c}{d\rho_{12}\rho_{34}} + \frac{d_m g_0 m_E}{d\rho_{12}\rho_{34}} \\ \frac{g_0 m_E}{\rho_{12}\rho_{34}} \end{bmatrix} \quad (5.30)$$

Chapter 6

Physical Design and Fabrication

Following proof of the design concept using mathematical modeling and CAD simulation, this chapter describes the physical design and fabrication of the proposed micromanipulator. The chapter starts with PCJM design and fabrication alongside description of the actuators and sensors which are used in the mechanism. Next, the assembly of a serial configuration of PCJMs is shown and lastly, the mounting mechanism of the robot to be integrated into the ophthalmic operation rooms is presented.

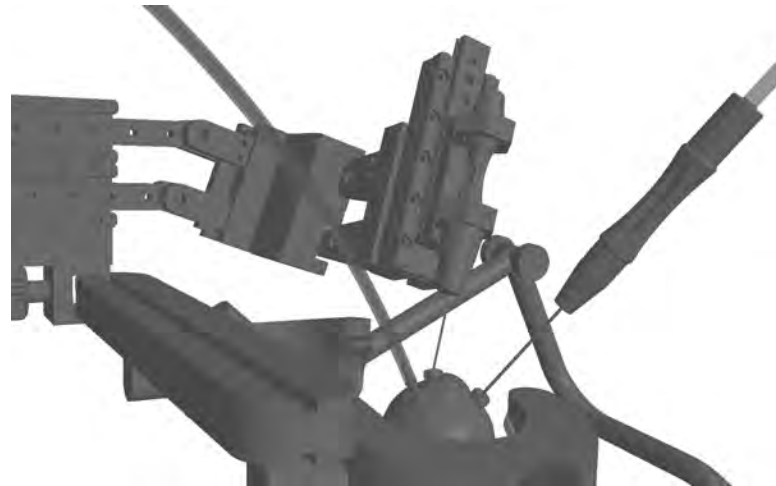


Figure 6.1: Physical design and fabrication of the setup.

6.1 Piezo Actuators

Motorized movements in this design are affected by piezo actuation technology. Conventional piezo actuators rely on the principle of the inverse piezoelectric effect in ceramic materials, which occurs when an externally applied electrical field causes mechanical deformation. Stick-

6. PHYSICAL DESIGN AND FABRICATION

slip piezo actuators were introduced in the 1980s and can be operated in two modes. The *stepping mode* allows large travel ranges and the *scanning mode* offers very high precision. This combination makes them more attractive than conventional piezo actuators, e.g. the walking piezo actuators [92]. High travel ranges for maximizing the reachability within the eye paired with high precision for placing the needle accurately makes this kind of actuator especially suited.

As it shown in Figure 4.4(b), the length change between the tip of the two prismatic actuators were accounted for with a precise and low friction microslider.

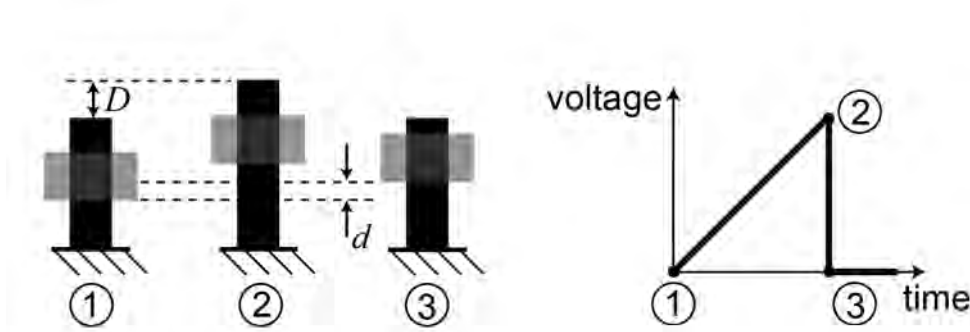


Figure 6.2: The stick-slip phase and the saw-tooth signal.

The position of the slider is controlled by applying a continuous saw-tooth signal to the actuators. The *amplitude* of the signal defines the maximum voltage and affects the displacement in each step. The *frequency* defines the number of steps in one second and can be seen as an indicator for velocity. Figure 6.2 shows, that when the voltage increases from 1 to 2 (stick phase), the piezoelectric element stretches by a distance of D . The friction between the piezoelectric element and the slider causes the slider to advance as well. The piezoelectric element shrinks when the voltage is reduced from 2 to 3 (slip phase). However, the slider does not completely move backwards to its original position due to its inertia. This results in a net forward displacement of $d < D$, also referred to as step width. As opposed to the stepping mode, the voltage signal between 1 and 2 is controlled in the sliding mode to achieve high precision.

Each PCJM consists of two Piezo actuators (see Figure 6.4). The selected actuators are developed by SmarAct GmbH¹ and are equipped with optical microsensors with an accuracy of $\pm 1\mu m$. The actuators of the first PCJM segment are *SmarAct SLCe1750mde* piezo positioners and support a higher resistive force which helps to counteract forces from the second PCJM and the end effector element. The other three elements, which will be discussed later, are of type *SmarAct SLC1750m* (see Figure 6.3). All positioners are equipped with microsensors. The most important characteristics are summarized in Table 6.1.

¹<http://www.smaract.de/>

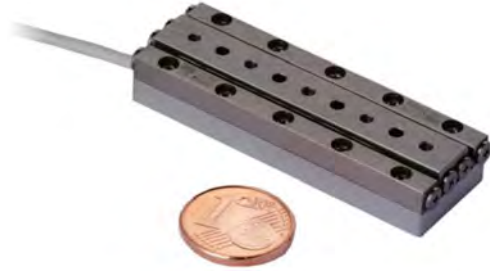


Figure 6.3: The stick-slip piezo actuator SmarAct SLC1750m [1].

Dimensions	$50 \times 17 \times 8.5mm$
Weight	32g
Travel range	$\sim \pm 15mm$
Step width	50 – 500nm
Scan range	$1.5\mu m$
Maximum velocity	$13 \frac{mm}{s}$
Maximum frequency	18.5kHz

Table 6.1: The most important parameters of the SmarAct SLC1750m [1].

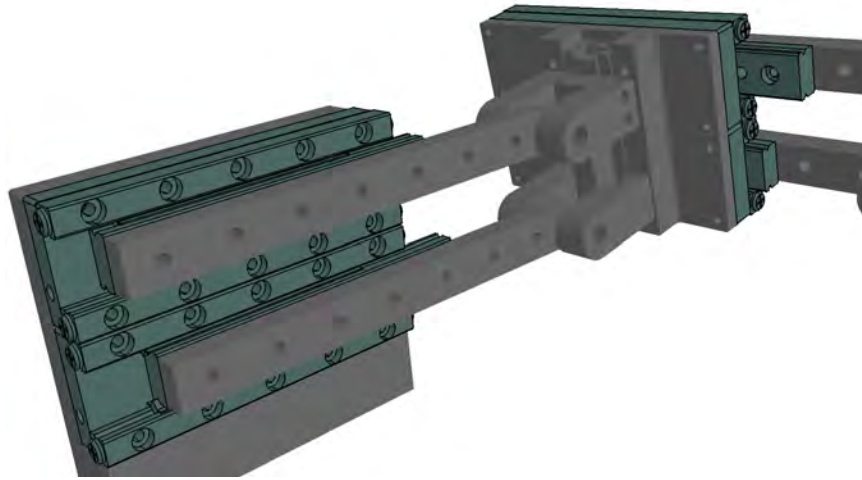


Figure 6.4: Each PCJM consists of two piezo actuators.

6.2 PCJM Fabrication

After placing two actuators in parallel configuration the next step is the development of the passive joint mechanism to transform two linear motions to one rotation and one translation.

The passive joint consists of two segments; a fixed segment (see Figure 6.5(a)), which is attached to the bottom actuators and a moving segment (see Figure 6.5(b)), which is attached to the top actuator. As previously mentioned the length change between the tip of the two prismatic actuators was covered by using a slider (see Figure 6.6(a)). In order to optimize the performance of the passive joint, components (ball bearings and slider) with the lowest possible

6. PHYSICAL DESIGN AND FABRICATION

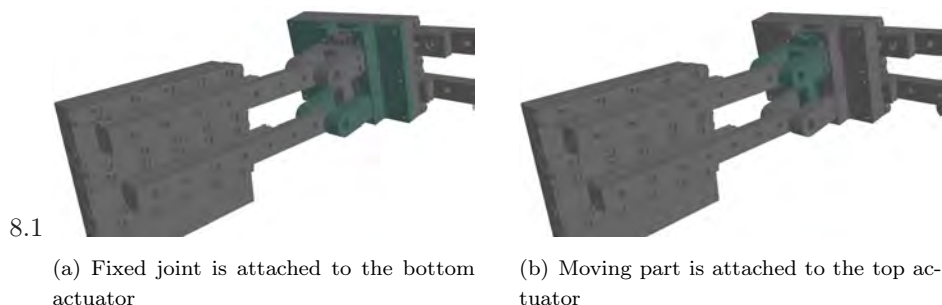


Figure 6.5: The passive joint of a PCJM

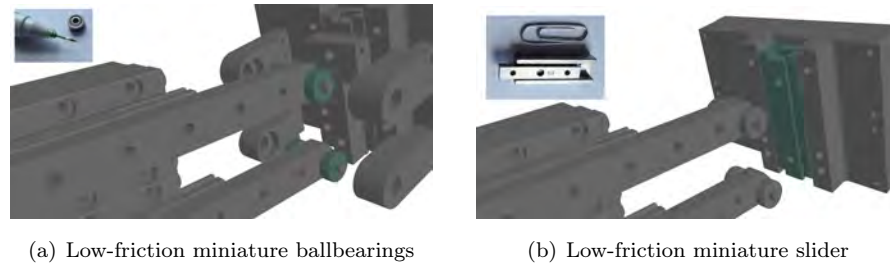
friction were selected (see Figure 6.6(b)).

The mechanical structure of the joint was produced with a precision of $0.01mm$. The material for the production of the robot's structure is aluminum. Following the steps discussed, a parallel coupled joint with piezo electric actuators, precise mechanical components, sub micron optical encoders and customized controller was developed. The properties of this mechanism were measured and were as follows:

- dimensions: $94 \pm 28 \times 33.5 \times 18.5mm$,
- weight: $150g$,
- linear travel range: $\pm 28mm$,
- angular rotation: $\pm 58.7^\circ$,
- linear precision: $1\mu m$,
- angular precision: $3.369 \times 10^{-3^\circ}$,
- maximum output force: $4.97N$,
- maximum linear velocity: $17.5 \frac{mm}{s}$,
- maximum angular velocity: $63.56 \frac{^\circ}{s}$.

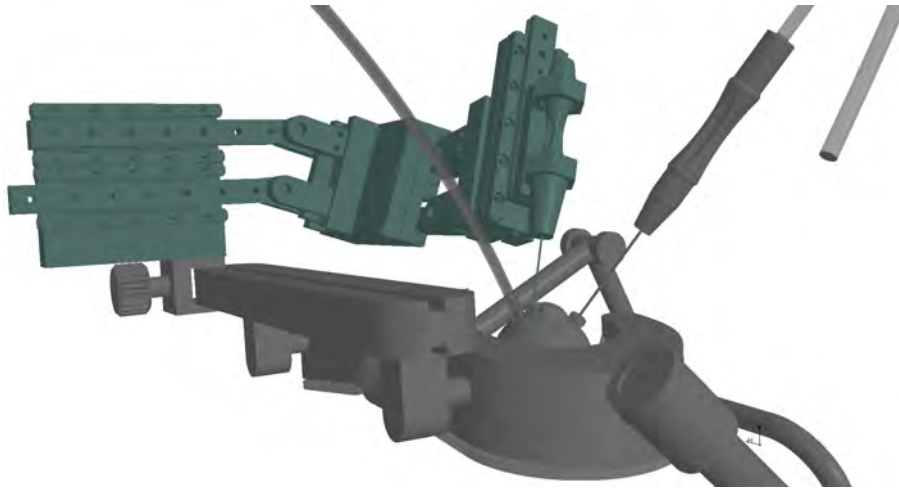
6.3 Robot Fabrication

Previous sections show that the robot is basically the serial configuration of PCJM segments with an actuated end effector. The first step of the robot assembly was having a suitable interface to attach PCJM segments to each other. Two different configurations were considered: 1) Attach the second PCJM to the end effector (front) of the first PCJM (see Figure 6.10(a)) 2) Attach the second PCJM to the middle of the first PCJM (see Figure 6.10(b)). Although the second configuration has better performance in terms of efficiency, ergonomically speaking the

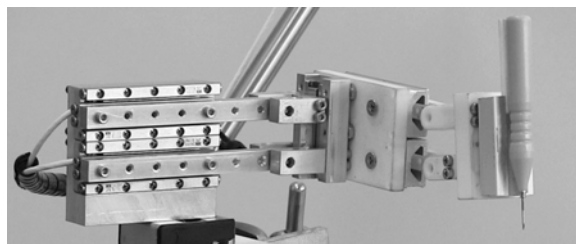


(a) Low-friction miniature ballbearings

(b) Low-friction miniature slider

Figure 6.6: Passive joint components**Figure 6.7:** Physical design and fabrication of the robot.

second configuration is more suitable for ophthalmic operation. First, a 3D printed prototype of the second segment and the tool gripper was produced and attached to the first working segment to perform the clinical experiments for performance analysis (see Figure 6.8). Following the successful experiments, the development of the complete robot was started. During experiments with the mock-up second segment, it was seen that it was better to increase the output force of the first segments, actuators with double piezo stacks. Attached to the end effector of the

**Figure 6.8:** The robot with mock-up second PCJM segment.

6. PHYSICAL DESIGN AND FABRICATION

second PCJM segment there is an additional actuator to enable the translational motion of the tool. Several tool grippers were designed and developed in this project. It is worth mentioning that an optional rotational piezo actuator can be added into the end effector to enable tool rotation and consequently 6 DOF in the robot.

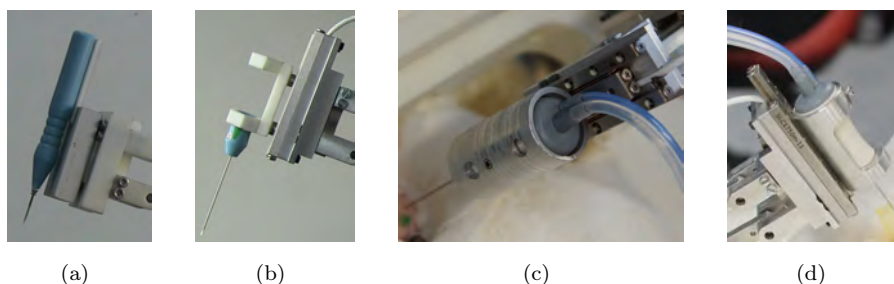


Figure 6.9: Tool Grippers

Two versions of the robot with different serial configurations and the following features were developed:

Robot Size: The larger configuration of the robot has dimensions of $185 \times 44 \times 226mm$, however, both weigh $306g$, which is smaller and lighter than an average surgeon's hand.

Working Space: The working volume of the end effector or the tool tip of the developed robot is a $28 \times 28 \times 28mm$ box. The angular movement of the tool is limited to $\pm 1.2761rad$, $\pm 1.2761rad$ and $2\pi rad$ around X , Y and Z axes, respectively.

Performance Validation: The precision of the tool tip motion, based on the visual observation from the ophthalmic microscope, is less than $5\mu m$ in the x and y directions and $1\mu m$ in the z direction. The output forces of the robot's end effector were measured as $4.97N$ in the x and y directions and $2.84N$ in the z directions. The maximum linear and angular velocity of the tool tip were measured as $67.46 \frac{mm}{s}$ and $86.91 \frac{deg}{s}$ respectively.

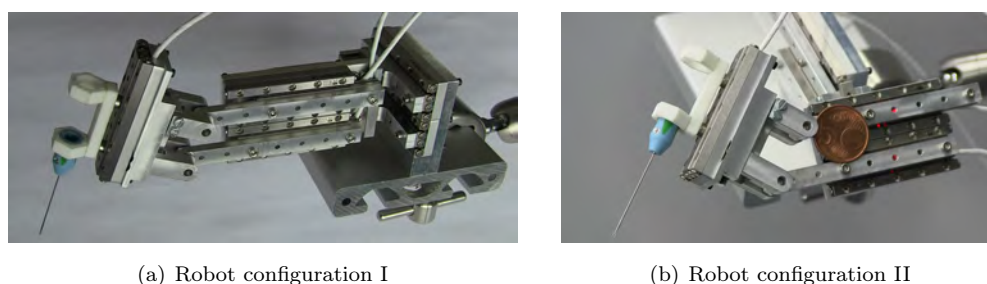


Figure 6.10: Robot configurations

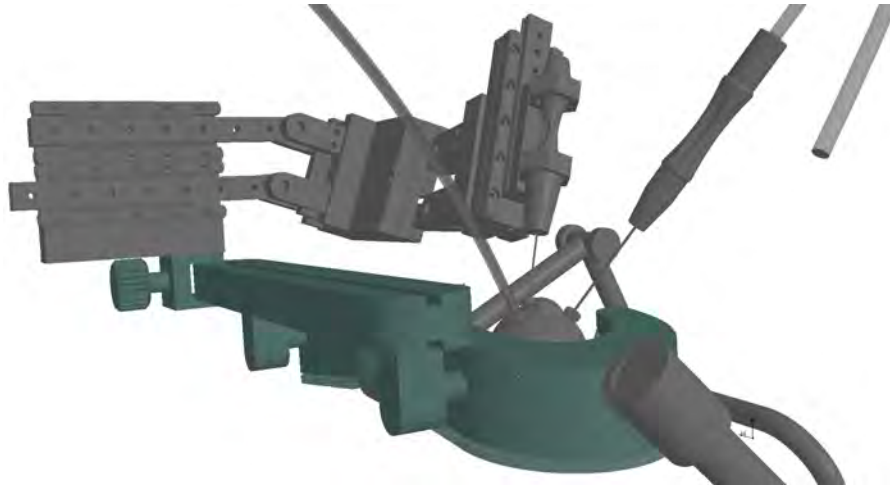


Figure 6.11: The mounting mechanism of the robot.

6.4 Mounting Mechanism

The dimensions and the weight of the robot make it possible to be mounted onto the patient's head. This feature addresses a fundamental problem in robot assisted ophthalmic surgery as unwanted motion of patient's head and body is not an obstacle to achieve high precision anymore. On the course of this project a mounting mechanism was designed and developed which attaches to operation table and carries the robot.

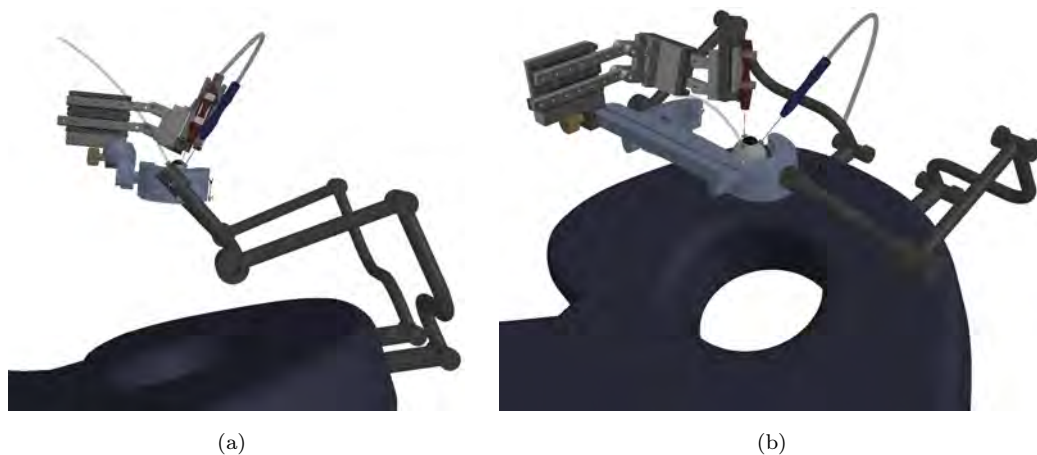


Figure 6.12: Robot mounted on an operating table

The goggle-like mounting structure is normally folded under the operation table in the park position. Whenever the surgeon's skill must be augmented by robotic precision, the surgeon can unfold the mechanism and mount it onto the patient's forehead. A prototype of this mechanism

6. PHYSICAL DESIGN AND FABRICATION

using bio-compatible materials was developed and evaluated.

Chapter 7

Control and Software Architecture

This chapter describes approaches for controlling the robot. Firstly, the linear piezo positioners, the principal actuation elements of the robot, are analyzed. Next, an overall control design is presented which enables tool motion with a 3D mouse. Constrained motion with respect to a RCM is elaborated and additional applications for other virtual fixtures are presented. Simulation environment development for testing the controllers, augmented visualization and training of the surgeons are also introduced. The chapter concludes with a description of the software implementation.

7.1 Linear Piezo Positioner Analysis

Stick-slip piezo actuators, which are used for actuation of the robot, are highly non-linear with unknown parameters. The effect of hysteresis, properties of the contact surface, load force applied to the slider and to some extent temperature and humidity all contribute the behavior of the actuator. More precisely, the step width, which is controlled by the input voltage, varies depending mostly on the hysteresis, the position of the actuator, the direction of movement and applied force. To cover all these factors a complex model is needed. Sources such as Bashash and Jalili [93] and Xu and Li [94] developed an adaptive control design for stick-slip piezo actuators. In [92] a mathematical model was introduced and tested against the *SmarAct SLC-1750m* piezo actuator, the same actuator used for the robot developed in this project.

In order to have a simplified model and avoid effects of the hysteresis from voltage modulation, the aim in this thesis is to control the actuators with a fixed voltage. Instead, the velocity is adjusted by modulating the frequency of the saw-tooth signal. Therefore, a simple velocity-to-frequency mapping is derived and presented within this section.

Experiments: The response of each piezo actuator was recorded and analyzed through experimental study of the robot. For this, the actuators were driven separately with different

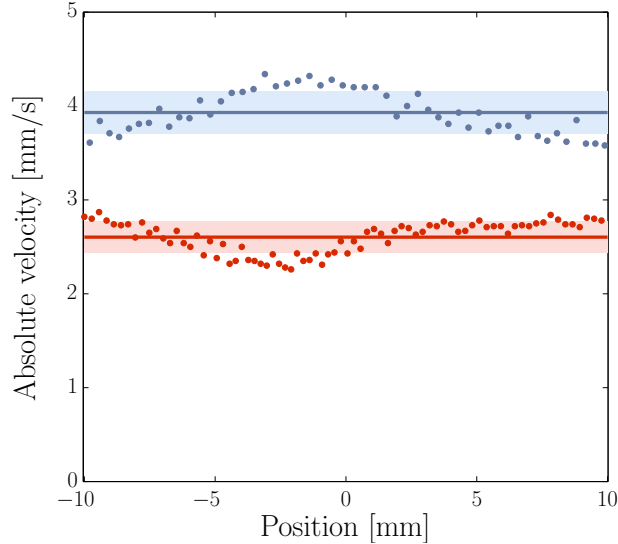
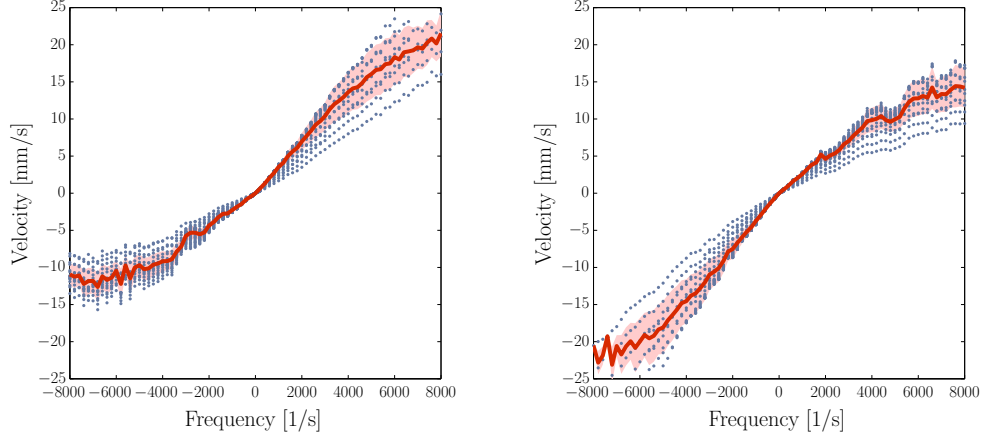


Figure 7.1: The velocity of the second slider against its position, with a frequency of 1000Hz. The lines represent the mean velocity over the complete range and the shaded area the standard deviation. Red indicates the motion from -10mm to 10mm and blue from 10mm to -10mm .

frequencies while keeping all other actuators in the reference position. The voltage amplitude was fixed at $100V$ and the travel range was limited from -10mm to 10mm and vice versa. The robot was in a horizontal position during all experiments. In a specified time interval of 20ms the position of the analyzed actuator was recorded and used to determine the slider's velocity. Due to the proprietary software on the control board and the communication over USB, it cannot be determined when a command to read a position takes actually place. However, if Gaussian noise over the measurements is assumed it complies with the least squares approach in the frequency-to-velocity mapping. Figure 7.1 shows the velocity profile of one linear piezo actuator while moving it from -10mm to 10mm and back to -10mm at 1000Hz.

Experiments such as the one shown in Figure 7.1 were conducted in the frequency ranges from 10Hz to 200Hz with 10Hz steps and from 200Hz to 8000Hz with 200Hz steps. Figures 7.2(a) and 7.2(b) show the velocities for the actuators on the first PCJM over the considered frequency range of motion from -8000Hz to 8000Hz (negative sign shows the direction of the motion). The red line shows the mean of the measured velocities and the area surrounding it represents the standard deviation. The graphs show that higher frequencies lead to a wider range of measured velocities along the travel range. Additionally, the velocity profile is non-linear and curved at the end, meaning that the velocity increases less in high frequency ranges. The figures also show the different behavior of the two actuators. For one, this is due to changing conditions during manufacturing, but is certainly also influenced by the dynamics of



(a) Recorded velocities between -8000Hz and 8000Hz for the first slider. (b) Recorded velocities for the second slider.

Figure 7.2: The result of the experiments to determine the velocities at different frequencies on 03.09.2013.

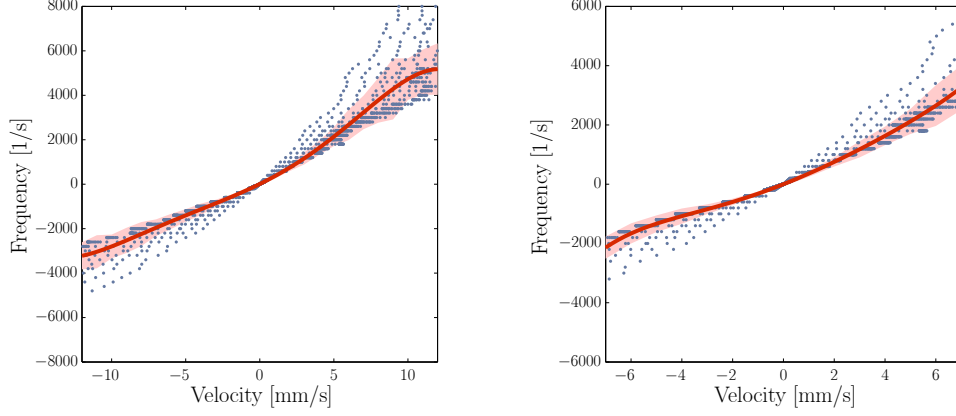
the system i.e. the load force exerted by the second PCJM of the robot.

7.1.1 Velocity-to-Frequency Mapping

From the experiments a frequency-to-velocity mapping is derived for each actuator. The actuator's position is not included, because of simplicity and as the experiments showed, it has not a major impact in the low frequency ranges. A polynomial of degree 5 is chosen to fit the data via least squares, which is a good compromise between complexity and accuracy of the model. The data is split into two parts for each actuator. One polynomial covers the velocity range from $\pm 7 \frac{\text{mm}}{\text{s}}$ and the second covers the rest until $\pm 12 \frac{\text{mm}}{\text{s}}$. From the experiments it was concluded, that higher velocities have a wider range of possible frequencies and thus no stable mapping is possible. Additionally, in practical experiments $\pm 5 \frac{\text{mm}}{\text{s}}$ turned out to be sufficient for operating the robot. Figures 7.3(a) and 7.3(b) display the polynomial mappings of the actuator corresponding to the displacement L_2 .

7.1.2 Calibration Procedure

Due to changing conditions of temperature and humidity, the mapping previously described can change to some extent. To mitigate of this effect, a calibration procedure was performed. The end effector was moved along a predefined trajectory in open-loop mode as shown in Figure 7.4(b). For the mapping within the range of $7 \frac{\text{mm}}{\text{s}}$, the maximum velocity of the trajectory was limited to $5 \frac{\text{mm}}{\text{s}}$ and for the mapping until $12 \frac{\text{mm}}{\text{s}}$, to $10 \frac{\text{mm}}{\text{s}}$. The position of each linear actuator was recorded and the actual velocities v_{act} determined. These velocities were compared to the



(a) Mapping of velocities within $\pm 12 \frac{mm}{s}$ to frequencies.

(b) Mapping of velocities within $\pm 7 \frac{mm}{s}$ to frequencies.

Figure 7.3: Frequency-to-velocity mapping for the second linear actuator.

desired velocities v_{des} and the previously defined mapping corrected by adjusting the mapped frequency f linearly. For each recorded velocity the following steps were performed:

$$e = v_{act} - v_{des} \quad (7.1)$$

$$v_{new} = v_{des} - \frac{e}{2} \quad (7.2)$$

$$f_{new} = f_{act} \frac{v_{new}}{v_{des}} \quad (7.3)$$

The error $e = v_{act} - v_{des}$ defines the difference between the measured and desired velocity. Because a positive error corresponds to a velocity that is too high, the frequency was also set too high. As a result, the error was halved and subtracted from the desired velocity define v_{new} , which corresponds to a lower frequency. The error was halved in order to prevent over-fitting in a later step. The original frequencies f_{act} were then linearly corrected by the ratio of v_{new} and v_{des} . The values of v_{des} and f_{new} are taken as an input for the velocity-to-frequency mapping with a polynomial of degree 5.

This correction step was performed for all actuators over several iterations. Each iteration included the movement along the predefined trajectory with the updated mappings. Figure 7.4(a) shows the root-mean-squared error (RMSE) of several iterations of the end effector's position and the individual RMSE of each actuator during one calibration procedure. The RMSE for one actuator i is calculated over the whole trajectory between the desired position $\hat{L}_{i,j}$ and recorded position $L_{i,j}$ as:

$$RMSE_i = \sqrt{\frac{\sum_{j=1}^n (\hat{L}_{i,j} - L_{i,j})^2}{n}} \quad (7.4)$$

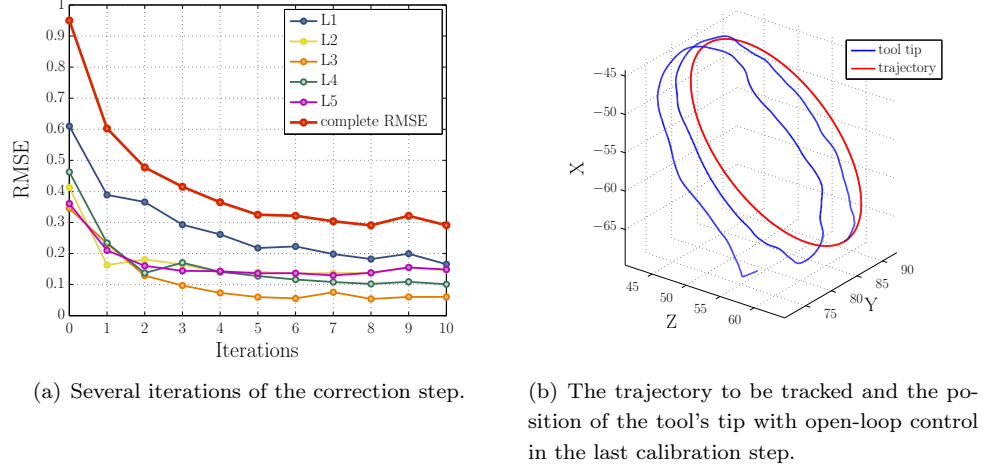


Figure 7.4: The calibration procedure and the trajectory to be tracked.

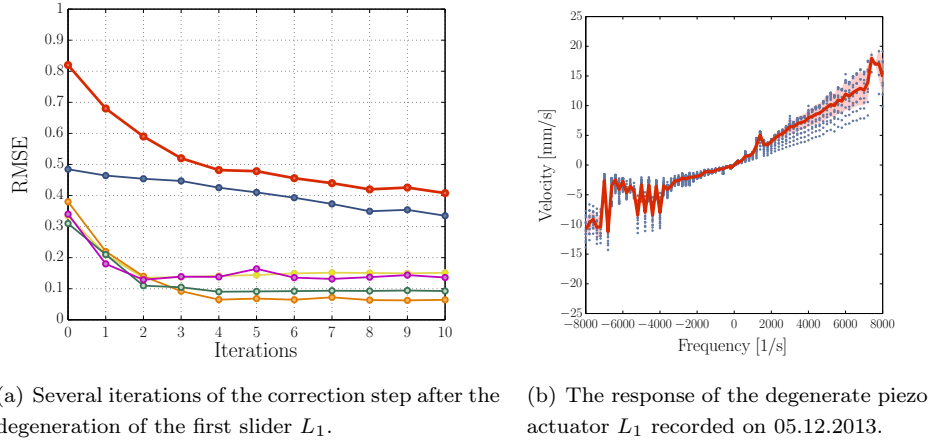


Figure 7.5: The calibration procedure with a degenerate piezo actuator.

The complete RMSE is defined as:

$$RMSE = \sqrt{\frac{\sum_{j=1}^n \|\hat{\mathbf{L}}_j - \mathbf{L}_j\|^2}{n}} \quad (7.5)$$

where $\mathbf{L}_j = (L_{1,j} \ L_{2,j} \ L_{3,j} \ L_{4,j} \ L_{5,j})^T$ and $\hat{\mathbf{L}}_j = (\hat{L}_{1,j} \ \hat{L}_{2,j} \ \hat{L}_{3,j} \ \hat{L}_{4,j} \ \hat{L}_{5,j})^T$. The first joint has the highest contribution to the overall RMSE and after the seventh iteration no major improvement takes place, as indicated in Figure 7.4(a). The position of the tool tip with respect to the desired trajectory in the last calibration step is displayed in Figure 7.4(b).

Over long period of use, the behavior of the actuator corresponding to L_1 changed signif-

icantly. As seen in Figure 7.5(b), the response is very different from the experiment recorded earlier shown in Figure 7.2(a). This may be due to a hardware defect meaning that insufficient friction was able to be provided. Because of this, the calibration error displayed in Figure 7.4(a) increased as Figure 7.5(a) illustrates. However, experiments for this thesis in the low-velocity range until $5 \frac{mm}{s}$ could still be performed without significant problems.

7.2 Control Design

With the developed mapping from the previous section, the robot is controlled via the 3D mouse. In this section, a desired point and orientation is defined by the 3D mouse, and the robot tries to track it via a simple proportional control system. This proved to be sufficient for manual control. The desired position and actual position of the robot's end effector are defined as:

$$\mathbf{x}_{des} = \begin{pmatrix} x' \\ y' \\ z' \\ \alpha' \\ \beta' \\ \gamma' \end{pmatrix} \quad \mathbf{x} = \begin{pmatrix} x \\ y \\ z \\ \alpha \\ \beta \\ \gamma \end{pmatrix} \quad (7.6)$$

with $\mathbf{x}_{des}, \mathbf{x} \in \mathbb{R}^3 \times \mathcal{S}^3$. The vector \mathbf{o} defines the displacement in encoder units along each axis of the 3D mouse, with values in the range of ± 350 . They are mapped to a velocity vector via the function $\mathbf{v}(\mathbf{o})$. The vector is used as an increment which is added to the desired position from the former time step \mathbf{x}_{des}^{t-1} and defines the desired position of the current time step \mathbf{x}_{des}^t i.e.

$$\mathbf{x}_{des}^t = \mathbf{x}_{des}^{t-1} + \mathbf{v}(\mathbf{o})\Delta t \quad (7.7)$$

where Δt defines the sampling rate in the control-loop.

7.2.1 Input Device Mapping

To allow smoother control, the displacements are not linearly mapped to velocities, but the following rule is used for translational movement:

$$v_t(o) = \begin{cases} b(\exp(a(o - o_{thresh})) - 1) & \text{if } o > o_{thresh} \\ -b(\exp(a(|o| - o_{thresh})) - 1) & \text{if } o < -o_{thresh} \\ 0 & \text{if } |o| \leq o_{thresh} \end{cases} \quad (7.8)$$

where $o_{thresh} = 30$ is set as a threshold to filter noise from the input device and the coefficients are set to $a = 0.1815$, $b = 0.0102$. The mapping is shown in Figure 7.6.

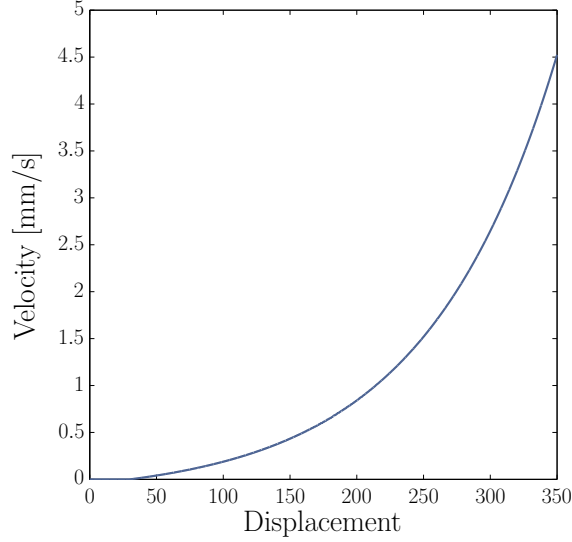


Figure 7.6: The mapping from the offset of the input device to velocity.

The function for rotational motion is similar. However, due to the parallel kinematics, the rotational velocity $v_r(o)$ is converted into translational movement $v_t(o)$ via:

$$v_t(o) = l(q_5) \sin(v_r(o)) \quad (7.9)$$

Here, $l(q_5)$ is the function that defines the distance of the end effector to the upper joint of the second PCJM and depends on the displacement q_5 of the last joint. Using the dimensions of the robot, the function is defined as $l(q_5) = 18.33 + q_5$.

By rearranging Equation 7.9, the rotational movement is given as:

$$v_r(o) = \arcsin\left(\frac{v_t(o)}{18.33 + q_5}\right) \quad (7.10)$$

Assuming a maximum displacement of 15mm for q_5 and a maximum translational velocity of $v_t(350) \approx 4.5 \frac{mm}{s}$ (see Figure 7.6), the maximum velocity for v_r is determined by:

$$v_{r_{max}} = \arcsin\left(\frac{v_t(350)}{18.33 + 15}\right) \quad (7.11)$$

$$= 0.14 \text{ rad/s} \quad (7.12)$$

The mapping is then defined by:

$$v_r(o) = v_t(o) \frac{v_{r_{max}}}{4.5} \quad (7.13)$$

7.2.2 P-Control

With the relationship of joint velocities to Cartesian velocities via the Jacobian $\dot{\mathbf{p}} = \mathbf{J}(\mathbf{q})\dot{\mathbf{q}}$ and the error $\mathbf{e}_p = \mathbf{p}_{des} - \mathbf{p}$, the proportional control law can be derived from:

$$\dot{\mathbf{q}} = \mathbf{J}(\mathbf{q})^{-1} \mathbf{K}_p \mathbf{e}_p \quad (7.14)$$

with \mathbf{K}_p being a semi-positive diagonal matrix. Since $\dot{\mathbf{q}}$ corresponds to the simplified serial robot from kinematics section, the velocities need to be transformed to the parallel link velocities. This is achieved by using the mapping from control section and deriving it with respect to time, which, for the first two joints yields:

$$\frac{d}{dt} L_1(t) = \frac{d}{dt} (q_0(t) - d \tan(q_1(t))) \quad (7.15)$$

$$= \dot{q}_0(t) - \frac{2d \dot{q}_1(t)}{\cos(2q_1(t)) + 1} \quad (7.16)$$

$$\frac{d}{dt} L_2(t) = \dot{q}_0(t) \quad (7.17)$$

Similarly, the results for the other joints are:

$$\frac{d}{dt} L_3(t) = \dot{q}_2(t) + \frac{2d \dot{q}_3(t)}{\cos(2q_3(t)) + 1} \quad (7.18)$$

$$\frac{d}{dt} L_4(t) = \dot{q}_2(t) \quad (7.19)$$

$$\frac{d}{dt} L_5(t) = \dot{q}_4(t) \quad (7.20)$$

$$\frac{d}{dt} L_6(t) = \dot{q}_5(t) \quad (7.21)$$

In matrix form this can be rewritten as:

$$\dot{\mathbf{L}} = \begin{pmatrix} \dot{L}_1 \\ \dot{L}_2 \\ \dot{L}_3 \\ \dot{L}_4 \\ \dot{L}_5 \\ \dot{L}_6 \end{pmatrix} = \mathbf{M} \dot{\mathbf{q}} = \begin{pmatrix} 1 & -\frac{2d}{\cos(2q_1(t))+1} & 0 & 0 & 0 & 0 \\ 1 & 0 & 0 & 0 & 0 & 0 \\ 0 & 0 & 1 & \frac{2d}{\cos(2q_3(t))+1} & 0 & 0 \\ 0 & 0 & 1 & 0 & 0 & 0 \\ 0 & 0 & 0 & 0 & 1 & 0 \\ 0 & 0 & 0 & 0 & 0 & 1 \end{pmatrix} \begin{pmatrix} \dot{q}_0 \\ \dot{q}_1 \\ \dot{q}_2 \\ \dot{q}_3 \\ \dot{q}_4 \\ \dot{q}_5 \end{pmatrix} \quad (7.22)$$

With the elaborated velocity-to-frequency mapping $m(\dot{\mathbf{L}})$, the frequencies \mathbf{f} to control the robot are calculated as follows¹:

$$\mathbf{f} = m(\mathbf{M} \mathbf{J}(\mathbf{q})^{-1} \mathbf{K}_p \mathbf{e}_p) \quad (7.23)$$

¹The last joint \dot{q}_5 is currently not implemented and is not intended to be realized with a piezo actuator i.e. the last entry of \mathbf{f} can be ignored.

7.3 Virtual Fixtures

Using a robot assisted surgery setup enables more control possibilities. One possibility is to constrain the robot from entering certain portions of the workspace and thus provide a safety barrier. This concept is called the *virtual fixture*. This section explains how the robot can be used to assist the surgeon pivot the tool around the entry point on the sclera. Furthermore, two more applications of virtual fixtures are described and implemented on the robot.

7.3.1 Remote Center-of-Motion

One of the most important benefits of robot-assisted minimally invasive surgery is the restriction of motions through the entry point on the incision points. More specifically, the link penetrating the tissue is only allowed to move along its axis and rotate fixed at the insertion ports. This concept is known as Remote Center of Motion (RCM). It reduces stress on the tissue and thus accelerates the healing process after the surgery. For ophthalmic surgery the RCM is especially useful to maintain the eyeball in a certain position to perform operations on the retina. As the surgeon uses the microscope to look at the retina through the widened pupil, the eye should not be rotated while moving the tool. This is only possible by restricting the motion of the last link with respect to the entry point on the surface of the eye.

In order to implement the RCM for the robotic assistant, the general approach in [95] is adapted for the current setup. One major advantage of this approach in comparison to [96] is that it does not require the definition of a tangent plane at the point where the tool is inserted into the eye.

In our case the RCM is located on the axis of the tool shaft (see Figure 7.7) and its position can be written as:

$$\mathbf{p}_{rcm} = \mathbf{p}_5 + \lambda(\mathbf{p}_{tool} - \mathbf{p}_5) \quad (7.24)$$

By allowing $\lambda \in \mathbb{R}^+$, positions of the RCM along the axis that are not directly on the shaft can be obtained.

Taking the derivative of the equation with respect to time yields:

$$\dot{\mathbf{p}}_{rcm} = \dot{\mathbf{p}}_5 + \lambda(\dot{\mathbf{p}}_{tool} - \dot{\mathbf{p}}_5) + \dot{\lambda}(\mathbf{p}_{tool} - \mathbf{p}_5) \quad (7.25)$$

Given the Jacobians \mathbf{J}_{rcm} and \mathbf{J}_5 at the respective points \mathbf{p}_{rcm} and \mathbf{p}_5 , the equation can be reformulated by making use of the fact that $\dot{\mathbf{p}}_i = \mathbf{J}_i \dot{\mathbf{q}}$

$$\dot{\mathbf{p}}_{rcm} = \mathbf{J}_5 \dot{\mathbf{q}} + \lambda(\mathbf{J}_{tool} \dot{\mathbf{q}} - \mathbf{J}_5 \dot{\mathbf{q}}) + \dot{\lambda}(\mathbf{p}_{tool} - \mathbf{p}_5) \quad (7.26)$$

In matrix form this can be written as:

$$\dot{\mathbf{p}}_{rcm} = \begin{pmatrix} \mathbf{J}_5 + \lambda(\mathbf{J}_{tool} - \mathbf{J}_5) \\ \mathbf{p}_{tool} - \mathbf{p}_5 \end{pmatrix}^T \begin{pmatrix} \dot{\mathbf{q}} \\ \dot{\lambda} \end{pmatrix} = \mathbf{J}_{rcm} \begin{pmatrix} \dot{\mathbf{q}} \\ \dot{\lambda} \end{pmatrix} \quad (7.27)$$

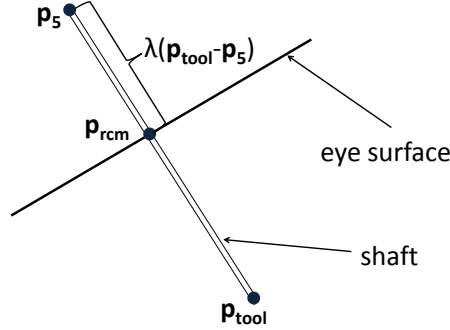


Figure 7.7: The location of \mathbf{p}_{rcm} .

With this formulation, it is possible to restrict the motion of \mathbf{p}_{rcm} by setting its velocity to zero i.e.

$$\dot{\mathbf{p}}_{rcm} = \mathbf{J}_{rcm} \begin{pmatrix} \dot{\mathbf{q}} \\ \dot{\lambda} \end{pmatrix} \stackrel{!}{=} \mathbf{0}_{3 \times 1} \quad (7.28)$$

with $\mathbf{J}_{rcm} \in \mathbb{R}^{3 \times 7}$. Enforcing this equation reduces the degrees of freedom of the robot by two. That means that for fulfilling a task in an n_t -dimensional space, the robot must have at least $n \geq n_t + 2$ degrees of freedom [95].

RCM Control Design

To satisfy the RCM constraint while moving the instrument within the eye, Equation 7.28 has to be included into the control design. For this purpose, two methods are most commonly used: The first is based on the concept of *task-priority* [97], as implemented in [96], and the second on the *alternative kinematics*¹ [99] approach, as shown in [95] and [100]. In this thesis, the approach using *alternative kinematics* is implemented where the RCM constraint can be directly incorporated into the robot task.

The robot has five degrees of freedom excluding the rotation of the needle from which two are used to fulfill the RCM constraint. As a result, three degrees of freedom are left, which match the three-dimensional workspace necessary to place the tip of the needle within the eye-ball.

The robot task, including the optional needle rotation, is expressed with coordinates $\mathbf{x}_t = \begin{pmatrix} x & \alpha & \beta & \gamma \end{pmatrix}^T$. The task space is defined by $\mathcal{T} = \mathbb{R} \times S^3$. Hence the robot task is defined with the Cartesian x position and the three angles α , β and γ corresponding to the rotation

¹Instead of *alternative kinematics* some authors refer to the same concept as *extended Jacobian*, introduced in [98].

about the x , y and z -axis, where α defines the optional rotation of the tool itself. Taking the RCM constraint into account, the extended task can be defined as

$$\mathbf{x}_{ext} = \begin{pmatrix} \mathbf{x}_t^T & \mathbf{p}_{rcm}^T \end{pmatrix}^T \quad (7.29)$$

$$= \begin{pmatrix} x & \alpha & \beta & \gamma & x_{rcm} & y_{rcm} & z_{rcm} \end{pmatrix}^T \in \mathbb{R} \times S^3 \times \mathbb{R}^3 \quad (7.30)$$

The kinematics of the extended task are then given by

$$\dot{\mathbf{x}}_{ext} = \begin{pmatrix} \mathbf{J}_t & \mathbf{0}_{4 \times 1} \\ & \mathbf{J}_{rcm} \end{pmatrix} \begin{pmatrix} \dot{\mathbf{q}} \\ \dot{\lambda} \end{pmatrix} = \mathbf{J}_{ext} \begin{pmatrix} \dot{\mathbf{q}} \\ \dot{\lambda} \end{pmatrix} \quad (7.31)$$

with $\mathbf{J}_{ext} \in \mathbb{R}^{7 \times 7}$. Given a desired robot task $\hat{\mathbf{x}}_t$, the actual positions of the joints \mathbf{x}_t , and the desired position of the RCM, which can be registered by the surgeon at the location of the cannula $\hat{\mathbf{p}}_{rcm}$ on the surface of the eye with respect to the world frame, the extended task error is given by

$$\mathbf{e}_{ext} = \begin{pmatrix} \hat{\mathbf{x}}_t - \mathbf{x}_t \\ \hat{\mathbf{p}}_{rcm} - \mathbf{p}_{rcm} \end{pmatrix} \quad (7.32)$$

Similar to the unconstrained movement from Section 7.2, the kinematic control is then written as

$$\begin{pmatrix} \dot{\mathbf{q}} \\ \dot{\lambda} \end{pmatrix} = \mathbf{J}_{ext}^{-1} \begin{pmatrix} \mathbf{K}_t & \mathbf{0}_{4 \times 3} \\ \mathbf{0}_{3 \times 4} & \mathbf{K}_{rcm} \end{pmatrix} \mathbf{e}_{ext} = \mathbf{J}_{ext}^{-1} \mathbf{K}_{ext} \mathbf{e}_{ext} \quad (7.33)$$

where $\mathbf{K}_t \in \mathbb{R}^{4 \times 4}$ and $\mathbf{K}_{rcm} \in \mathbb{R}^{3 \times 3}$ are both positive definite diagonal matrices. The control law guarantees decoupled exponential convergence of the task to the desired value [95].

Algorithmic Singularities

In case of unconstrained movement, it was already shown that the robot does not possess any singularities within its workspace. However, with the augmented kinematics applied in the control design, further singularities can be introduced due to rank deficiency or linear dependencies in the sub matrix \mathbf{J}_{rcm} [98]. These are called *algorithmic singularities*, but can be avoided by choosing the kinematic functions accurately. In the introduced control design, the angles ψ and ϕ are chosen instead of y and z coordinates to avoid algorithmic singularities within the robot's workspace. To prove that we look at the determinant of \mathbf{J}_{ext} :

$$\det(\mathbf{J}_{ext}) = -\cos(q_1)^2 \cos(q_3)^3 (d_4 + q_4)$$

Only if $q_1 = \frac{\pi}{2} + k\pi, k \in \mathbb{Z}$ or $q_3 = \frac{\pi}{2} + k\pi, k \in \mathbb{Z}$ the determinant becomes zero, which is impossible to achieve due to the design of the robot.

7.3.2 Further Applications

In the following, two further possible applications of virtual fixtures are presented.

7.3.2.1 Automatic Location of the RCM

During an ophthalmic surgery the eye usually needs to be rotated to access different areas on the retina. This results in a relocation of the RCM on the surface of the eye. To achieve this, the surgeon normally follows a registration procedure. This can be done with the help of a marker on the instrument. The surgeon pulls the instrument out of the eye until the marker becomes visible and then pushes a button on the 3D mouse. The RCM is then reset to the position of the marker. However, this procedure is time consuming and distracts the surgeon from the actual task during an eye surgery. As a result, a method for automatically locating the RCM with the current setup is presented.

If the eye is assumed to be a simple sphere [90], it can be described with four points in Cartesian space. Before a procedure begins, the surgeon follows the previously explained registration procedure four times at different locations. That is, the eye is rotated to four different positions and the instrument pulled away from the eye until the marker becomes visible. By pushing the button on the 3D mouse, the coordinates of the marker are recorded, and after the fourth registration procedure the parameters of a sphere can be determined as explained in bellow. The most general way of describing the geometry of a sphere is implicitly in the projective space \mathbb{P}^3 with the equation:

$$\mathbf{x}^T \mathbf{Q} \mathbf{x} = 0$$

with \mathbf{x} representing a point in \mathbb{P}^3 and \mathbf{Q} the quadric surface, which is given by the diagonal matrix $\mathbf{Q} = \text{diag}(1, 1, 1, -1)$ (see e.g.[101]). The quadric is transformed as follows:

$$\mathbf{Q}' = \mathbf{T}^T \mathbf{Q} \mathbf{T}$$

with

$$\mathbf{T} = \begin{pmatrix} \mathbf{R} & \mathbf{t} \\ \mathbf{0} & 1 \end{pmatrix}$$

where \mathbf{R} represents a rotation matrix and \mathbf{t} a translational offset. In case of a sphere, \mathbf{R} is a diagonal matrix i.e. $\text{diag}(s, s, s)$ where s is a scaling factor. Thus the scaling of the sphere and its offset with respect to the robot base are encoded in \mathbf{T} . Given the four registered points, one can define four equations with $\mathbf{x}_i^T \mathbf{Q}' \mathbf{x}_i = 0$ to determine s and \mathbf{t} . To set the RCM automatically when it is moved, the intersection of the tool shaft with the sphere needs to be calculated. A point on the tool shaft can be expressed as

$$\mathbf{p}_l = \mathbf{p}_5 + \hat{\lambda} \mathbf{p}_{tool}, \hat{\lambda} \in \mathbb{R}$$

To determine the point of intersection, one has to calculate the value of $\hat{\lambda}$ via the equation:

$$\begin{pmatrix} \mathbf{p}_l^T & 1 \end{pmatrix} \mathbf{Q}' \begin{pmatrix} \mathbf{p}_l \\ 1 \end{pmatrix} = 0$$

This yields at most two results for $\hat{\lambda}$ if there is an intersection with the sphere. The desired solution for $\hat{\lambda}$ can then be determined from the orientation of the eye within the workspace. In our case, the eye points in the positive direction along the x -axis and thus the smaller value of $\hat{\lambda}$ is the correct solution. As a result, the position of the RCM is defined as

$$\mathbf{p}_{rcm} = \mathbf{p}_5 + \hat{\lambda}\mathbf{p}_{tool}$$

7.3.2.2 Epiretinal Membrane Peeling

For epiretinal membrane peeling, the tip of the needle needs to be moved in a constant and steady path along the macular area of the retina. In this section, it is explained how the robot can be utilized for this procedure. Again, it is assumed that the eye on which the operation is performed can be geometrically described as a sphere. However, an extension to a general quadric [101] is also possible. It is also assumed that the tool can be registered exactly to the patient's eye.

Similar to the automatic location of the RCM, the intersection of the axis of the instrument and the retinal surface, defined by a sphere, needs to be calculated. Following the same steps as before two values for $\hat{\lambda}$ are computed. However, for retinal membrane peeling the correct value i.e. the value at the retina for $\hat{\lambda}$ corresponds to the bigger value. To keep a certain distance l_{dist} from the retinal surface, the value of the intersection point \mathbf{p}_x can be adjusted by:

$$\mathbf{p}_x = \mathbf{p}_5 + \hat{\lambda}\mathbf{p}_{tool} - l_{dist} \frac{\mathbf{p}_{tool} - \mathbf{p}_5}{\|\mathbf{p}_{tool} - \mathbf{p}_5\|}$$

The value corresponding to the x position i.e. $\mathbf{p}_x(1)$ is then the input for the desired value in the control design.

7.4 Simulation Environment

The simulation environment developed for this thesis offers the possibility to test control algorithms without the hardware. It also provides a basis for augmented visualization during a surgery and training.

The user interface is shown in Figure 7.8. It includes a model of the robot and a model of a patient's head [102]. The left eye can be manipulated with the robot's instrument. A blue ring around the eye indicates the pars plana i.e. the outer diameter around the cornea where the cannulas are to be inserted. This visual marker helps to move the tool into the eye at the correct position. A network connection between the low-level control application (see Section 7.5) and the simulation environment allows the position of the real robot to be communicated to the simulation and displayed in the simulation environment.

An additional window offers a view into the eye from the top, similar to that of a microscope

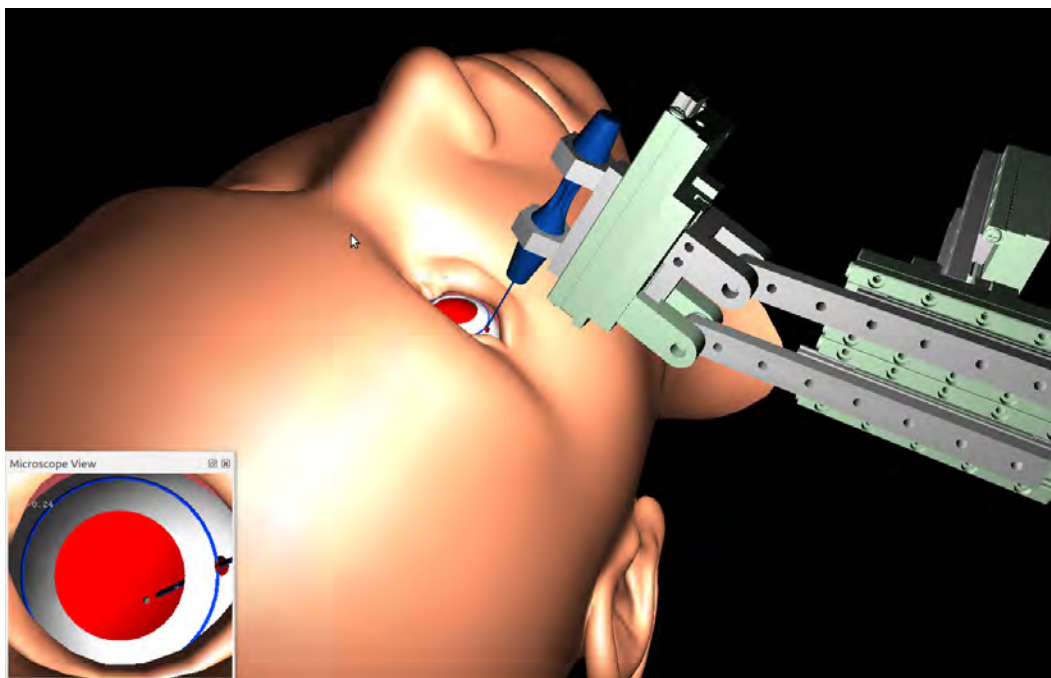


Figure 7.8: The user interface of the simulation environment.

used during an ophthalmic surgery. The following functionalities are currently implemented in the simulation environment:

- **Forward kinematics:** The user can specify the displacements for each linear positioner, which define the pose of the robot. This is calculated via forward kinematics..
- **Inverse kinematics:** The user specifies the pose of the end effector i.e. x , y and z for translation and α , β , γ for its orientation. Given these values, the offsets of each linear positioner are calculated and set via inverse kinematics. This functionality mainly serves to verify the inverse kinematics.
- **Direct control:** The user can control the robot in the simulation environment either with the 3D mouse with the keyboard. The control algorithms are the same as those implemented on the real robot. The control modes can be switched from unconstrained motion (see Section 7.2) to constrained motion (see Section 7.3.1). The RCM is visualized as a red sphere. This functionality provides testing of control modes without the real robot and is also a tool for training surgeons on certain clinical procedures.
- **Slave control:** This function allows the user to set an initial position of the real robot, which is sent to the low-level control application. Additionally, the low-level control application sends the current position of the real robot to the simulation environment, which can display it. This serves as a basis for augmented visualization that would help the surgeon locate and move the tool during a clinical procedure.

- **Positioning and manipulation of the eye:** In Section 4.3.4 the best position of the eye with respect to the robot for the maximum reachability within the eye is determined. In the simulation, the eye and head may be placed at a desired position with respect to the robot base. Furthermore, the eye can be manipulated. Collisions between the tool and eye are registered and movements of the tool result in rotations of the eye around its center. A visual marker within the eye shows where the tool is aimed at, as indicated in the *Microscope View* in Figure 7.8.
- **RCM control demonstration:** This functionality is only for demonstration purposes and shows the constrained motion with an RCM along a spiral trajectory. The position of the RCM and the parameters of the spiral can be set.

Due to the fact that the robot in the simulation environment behaves similar to the real robot, it can already be used for getting accustomed to controlling the robot and its workspace boundaries. Furthermore, it is intended to use the application during a surgery for augmented visualization. However, this requires further development in the direction of registering the patient to the 3D model. Also, a 3D model of the patients eye and an image of the retina would be necessary to fully benefit from augmented visualization.

7.5 Implementation

The software was implemented in C++ and uses mainly the following libraries:

- **Qt4:** is the software framework used for the development of the graphical user interface for the simulation environment.
- **Coin3D:** offers programming tools for 3D graphics in OpenGL for the simulation environment. It is free and an open-source implementation of the Open Inventor API.
- **Robotics library:** covers a range of tools for common tasks in robotics including mathematics, kinematics and dynamics [103]. It is used to retain an abstract view of the robot in the low-level control application as well as in the simulation environment.
- **Eigen:** provides comprehensive support for linear algebra, which is especially useful for the development of control algorithms presented in this thesis.

7.5.1 Software Architecture

Figure 7.9 outlines the software architecture. It represents the real implementation, as that the blunt shapes define collections of classes and functions. The architecture is structured into three parts: the simulation environment, the low-level control application and the software running on the control boards for the linear positioners. Since the latter is proprietary, it is not known exactly how it is implemented. It provides a serial interface for sending commands (see [104]). In this thesis, most commonly commands for sending a desired frequency and voltage are used;

7. CONTROL AND SOFTWARE ARCHITECTURE

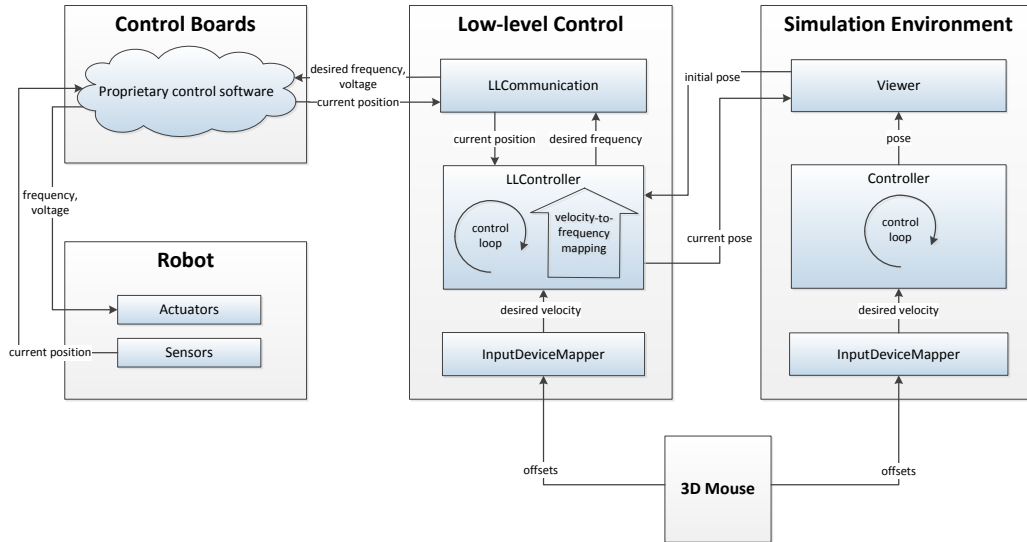


Figure 7.9: The software architecture.

these are passed on to the actuators of the robot. For closed-loop control it also provides an interface to obtain the position of the linear actuators measured by the microsensors. In the following, the two main applications and components developed within this thesis are explained:

- **Low-level Control**

The low-level control application contains the algorithms for controlling the robot via a 3D mouse. It communicates with the control boards via serial-over-USB to send appropriate frequencies to drive the piezo actuators and to receive their current position. It provides a network interface for the simulation environment, which can send an initial position for the robot. This is useful for moving the tool to a desired position at the beginning of a procedure without using the 3D mouse. The three main components are:

- **InputDeviceMapper:**

This component receives the translational and the rotational offsets from the 3D mouse and maps them to desired velocities (see Section 7.2), which then define the desired position. These values are passed on to the actual controller, which uses them as an input for the control design.

- **LLController:**

The low-level controller implements the two main algorithms for controlling the robot. The control-loop is outlined in algorithm. Given the desired velocity in Cartesian space from the *InputDeviceMapper* and the current position of the actuators, either the control design for unconstrained movement (see Section 7.2) or constrained movement with an RCM (see Section 7.3.1) is applied. The control de-

sign method is switched by a flag that is set by pressing a button on the 3D mouse. Both control designs yield a desired velocity for each of the linear positioners. These have to be mapped to frequencies, which follows the approach described in Section 7.1.1. The frequencies are passed on to the low-level communication component.

In each control-loop the current position of the robot is transferred to the simulation environment over a network interface. At the start-up of the application the component offers a network interface for receiving an initial position to the robot. The control-loop will be explained in more detail.

– **LLCommunication:**

The low-level communication component communicates with the control boards over the serial interface and receives a message that contains the current position of the actuators, which are measured by the microsensors. The message is unpacked and the position of each actuator is given to the *LLController* component for applying the desired control scheme. In exchange, it receives the frequencies that have to be applied for reaching a certain velocity from the *LLController* component. These frequencies are packed into messages and sent to the control boards via serial-over-USB.

• **Simulation Environment**

The simulation environment is a stand-alone application and offers testing of control algorithms and a basis for training and augmented visualization (see Section 7.4). It consists of three main components:

– **InputDeviceMapper**

This component is another instance of the *InputDeviceMapper* from the low-level control application. The values from the 3D mouse are mapped to desired velocities and passed to the controller component.

– **Controller**

The controller in the simulation environment is very similar to the *LLController* component in the low-level control application and also implements the control designs for unconstrained and constrained motion. However, due to the fact that no real positions are measured, it predicts virtual positions of the actuators and thus assumes a perfect environment. The robot's pose in each loop is then transferred to the *Viewer* component.

– **Viewer**

This component displays a 3D model of the patient's head and the robot. One eye can be manipulated with the robot's instrument. The user can select different options for controlling the robot and for verifying algorithms (see Section 7.4). Depending on the selected control mode, the *Viewer* receives the robot's pose from the *Controller* component or via a network interface from the low-level control application. It also allows an initial pose to be sent to the low-level control application.

Control-loop

The mentioned algorithm lists the steps in the control-loop. It uses the predefined matrices \mathbf{K}_p and \mathbf{K}_{ext} for the control designs and an initial position that is set by the simulation environment. The matrix \mathbf{M} contains the mapping from the simplified serial robot to the robot with parallel kinematics (see Section 7.2). The desired Cartesian position \mathbf{x}_{des} is set to the initial position and λ to 1, which locates the RCM on the tip of the instrument (see Section 7.3.1). In the actual control-loop the configuration of the robot is read and converted into the serial configuration \mathbf{q} (line 5). To obtain the current Cartesian position \mathbf{x}_{curr} of the robot, forward kinematics is applied. The desired position is determined through the desired velocity given by the 3D mouse (line 7). With this, the error between desired and actual position can be calculated.

If the control mode is set to *rcm* the extended error needs to be determined. It includes the position of the RCM, which is determined by λ (see Section 7.3.1). With the extended Jacobian \mathbf{J}_{ext} and \mathbf{K}_{ext} , the joint velocities $\dot{\mathbf{q}}$ for the serial robot and $\dot{\lambda}$ are calculated. Additionally, λ needs to be updated after each time step.

For the unconstrained movement, only the Jacobian \mathbf{J} is needed, and together with \mathbf{K}_p and the Cartesian error, the joint velocities can be determined.

Given the joint velocities $\dot{\mathbf{q}}$, the frequencies are then calculated. For this, the velocities need to be transformed into the velocities that correspond to the parallel robot via \mathbf{M} (see Section 7.2). After this step, the frequencies are passed on to the low-level communication which sends them to the control boards, where they are applied to the piezo actuators.

7.5.2 Hardware Setup

Figure 7.9 shows that the proprietary software runs on the control boards that directly communicate with the robot. As a result, the control boards and the robot are tightly coupled and constitute the slave. The low-level control and simulation environment are separate applications and provide interfaces for each other. Together with the 3D mouse they constitute the master. They can either run on the same or on different hosts connected over a network. Currently, both applications run on a conventional notebook with Ubuntu 12.04. Tests with a Raspberry Pi board running the low-level control were not satisfactory, because the board lacks speed for an adequate sample rate in the control-loop. Also, the communication from the low-level control application to the proprietary software via serial-over-USB inhibits real-time capabilities of the current setup. However, it was concluded that for experimental usage and demonstration purposes the setup yields very promising results.

7.6 Middle-Ware Based Software Architecture

To keep the time delay between the surgeon's motion and robot reaction low and to keep the setup compact for seamless integration of the device into operation rooms, a middleware driven architecture using an embedded platform was also implemented [2].

```

1: function controlLoop( $\mathbf{K}_p$ ,  $\mathbf{K}_{ext}$ ,  $\mathbf{x}_{init}$ ,  $\mathbf{M}$ )
2:    $\mathbf{x}_{des} \leftarrow \mathbf{x}_{init}$ 
3:    $\lambda \leftarrow 1$ 
4:   while true do
5:      $\mathbf{q} \leftarrow \text{getConfiguration}()$ 
6:      $\mathbf{x}_{curr} \leftarrow \text{forwardKinematics}(\mathbf{q})$ 
7:      $\mathbf{x}_{des} \leftarrow \mathbf{x}_{des} + \text{getDesiredVelocity}() * \Delta t$ 
8:      $error \leftarrow \mathbf{x}_{des} - \mathbf{x}_{curr}$ 
9:     if mode == rcm then
10:       $error_{ext} \leftarrow \text{getExtendedError}(error, \lambda)$ 
11:       $\mathbf{J}_{ext} \leftarrow \text{getExtJacobian}(\mathbf{q}, \lambda)$ 
12:       $\dot{\mathbf{q}}, \dot{\lambda} \leftarrow \mathbf{J}_{ext}^{-1} \mathbf{K}_{ext} error_{ext}$ 
13:       $\lambda \leftarrow \lambda + \dot{\lambda} * \Delta t$ 
14:     else
15:       $\mathbf{J} \leftarrow \text{getJacobian}(\mathbf{q})$ 
16:       $\dot{\mathbf{q}} \leftarrow \mathbf{J}^{-1} \mathbf{K}_p error$ 
17:      $\mathbf{f} \leftarrow \text{velocityToFrequency}(\mathbf{M} \dot{\mathbf{q}})$ 
18:     sendFrequencies( $\mathbf{f}$ )

```

This software architecture provides hard real-time operation along with plug-and-play functionality through low level device drivers. Mitchel et al. [28] presents robotic systems for steady micro manipulation. Jung et al. [105] present a component-driven architecture for robotic integration. However, in this part of the work we focus mainly on middle-ware architecture for embedded systems.

To facilitate a distributed operation and easy integration we have employed embedded middleware based architecture. It enables the representation of process data at a higher level of abstraction and thereby facilitates easy integration and seamless data sharing within a unified ecosystem. It also provides an API for user space application development.

The main distributed components (see Figure 7.10) are the input device controller and the high level robot controller. Each component is hosted on an independent Raspberry Pi board¹. The board consists of an ARM 700 MHz processor running a Debian Linux Kernel patched for hard real-time performance. The Xenomai² real-time patch is used which allows the development of hard real-time applications from user space. It supports USB for I/O and Ethernet for networking purposes. The middleware used is the embedded extension of Internet Communication Engine (ICE) [106] called IceE. It uses TCP/IP as the communication medium and is

¹Raspberry pi <http://www.raspberrypi.org/>

²P. Gerum, *Xenomai* implementing a rtos emulation framework on gnu/linux, GNU Free Documentation License (2004).

7. CONTROL AND SOFTWARE ARCHITECTURE

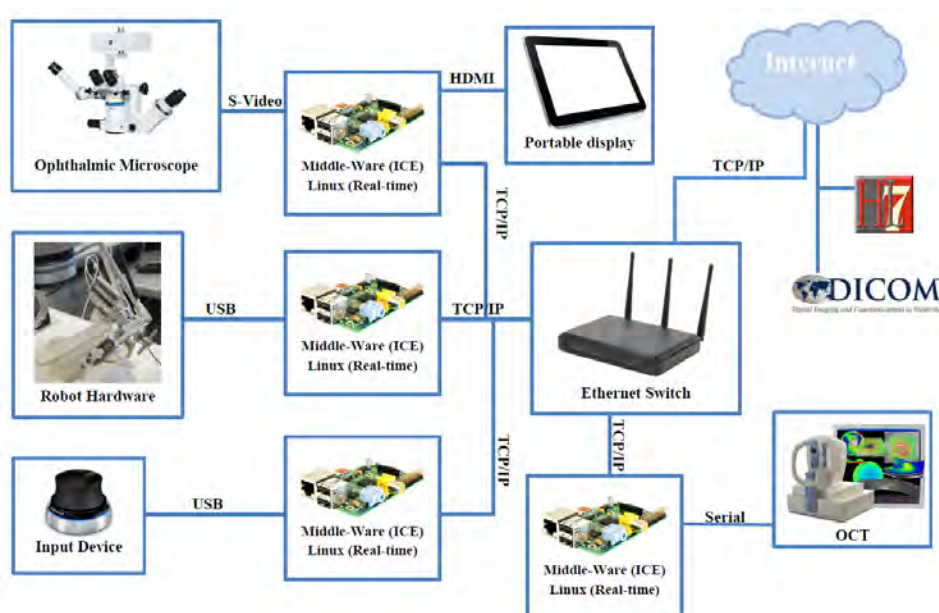


Figure 7.10: Middle ware based system architecture [2].

independent of platform and programming language. IceE uses a message scripting language called Slice [106], with which the user can represent the data in the form of message objects and define interfaces for transporting these messages. Thereafter, the Slice tools automatically generate source code for the message interfaces in various programming languages.

In the proposed architecture, a message interface is written for the data acquired from the 3D mouse by the input device controller. It consists of the translation and rotation data specified in a structure along with the interface function for transporting them over the network. A publish/subscribe mechanism is used wherein the input device controller hosts an Ice-Publisher. The high level robot controller implements an Ice-Subscriber to read the published message containing the data from the 3D mouse. This data is further processed and mapped to the robot joints through the robot inverse kinematics.

Both the input device and the robot controller components contain a hard real-time process using the Xenomai Library and the real-time patched Linux Kernel. In the input device application the data from the 3D mouse is acquired using the Spacenv library¹. This data is then packaged in the form of the ICE message object and published using the message interface. The high level robot controller component reads this data using the subscriber and processes it for tremor reduction and motion scaling. Thereafter, the data is mapped to the robot joints through inverse kinematics.

The robot itself is controlled in the velocity mode. A low-level device driver was developed

¹A free, compatible alternative for 3Dconnexion's 3D input device drivers and SDK. <http://spacenv.sourceforge.net> (May 2013).

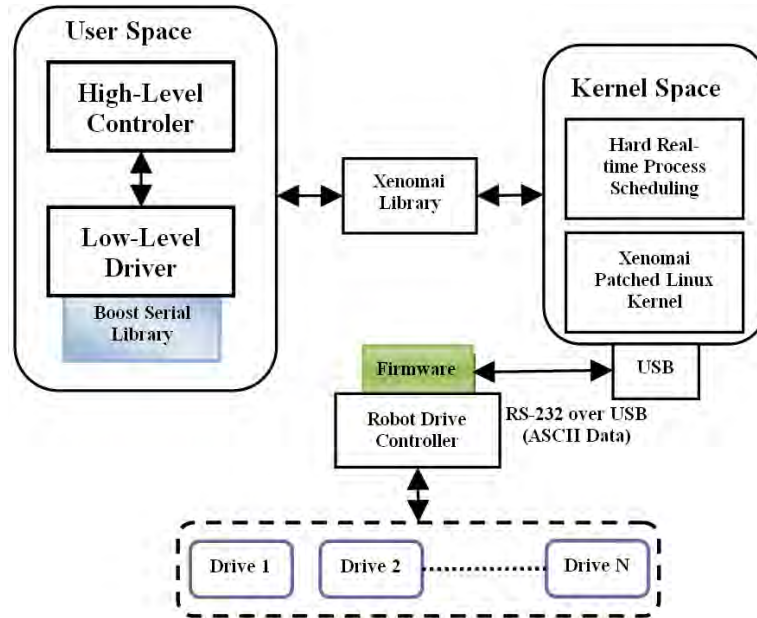


Figure 7.11: Robot controller block diagram [2].

in order to control the individual piezo drives of the robot. The driver sends ASCII based motion and feedback commands to the drives through a Serial over USB protocol. This data is received by the firmware hosted on the low-level-robot control board which implements the power electronics. The complete control loop runs in a hard real-time process hosted by the high-level robot controller. Figure 7.11 illustrates the robot controller, consisting of the high level and low level components. Figure 7.12 shows the setup which is introduced here. It noteworthy that the entire apparatus including robot, controllers and etc. can be packed in a suitcase.

7. CONTROL AND SOFTWARE ARCHITECTURE

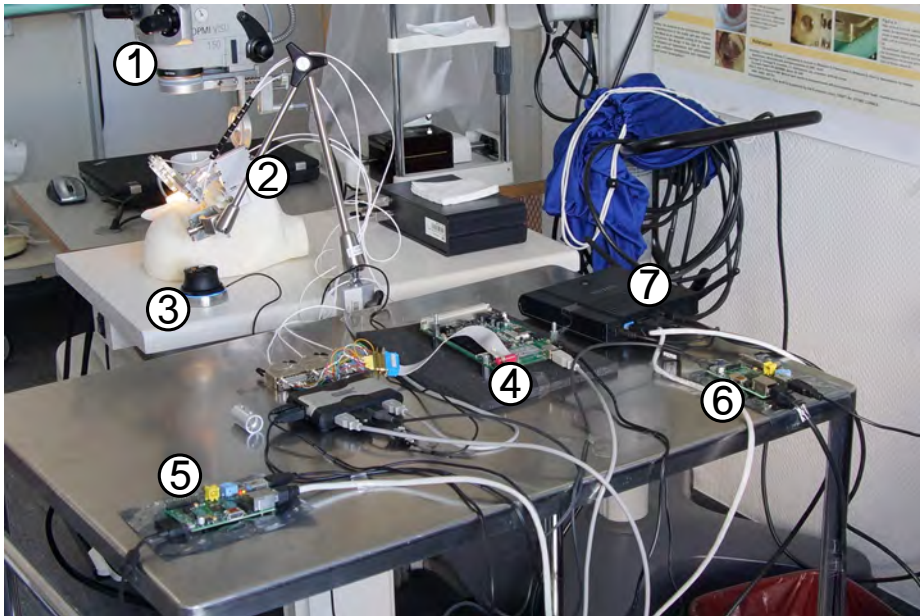


Figure 7.12: The embedded system based controller setup: 1. Microscope, 2. Robot, 3. 3D Mouse, 4. Power Electronic boards, 5. Robot Controller (Embedded), 6. Input Device Controller (Embedded), 7. Ethernet Switch [2].

Chapter 8

Experiments

In order to evaluate each step in the development of this work several experiments were performed from the beginning of the project. These experiments were supervised by ophthalmic surgeons from the design stage to the clinical experiments. The location of the experiments was a research and training lab at *Klinik und Poliklinik für Augenheilkunde am Klinikum rechts der Isar der Technischen Universität München*¹. The equipment and their arrangement are almost the same as an ophthalmic operation room. This chapter discusses the following experiments: OR compatibility experiment, PCJM concept evaluation experiment, Hybrid parallel-serial robot concept evaluation experiment, Virtual fixture experiments and retinal experiments.

8.1 OR Compatibility Evaluation

OR Compatibility Evaluation refers to tests which analyzed whether the robotic setup is compatible with the conventional ophthalmic operation atmosphere, to show:

- Minimum effort or change for setup of the robot.
- Setup compatibility with the other equipments such as the ophthalmic microscope and infusion device.
- The setup does not inhibit the surgeons and for OR assistants reaching and seeing the operation site.

Three OR compatibility evaluation experiments were performed in this work. The first experiment showed that the first prototype will not satisfy its objective, as the robot could not integrate the ophthalmic microscope. The kinematics of the robot needed to be changed. The second experiment showed that the second prototype could solve the compatibility problem and It would be well-suited to ophthalmic ORs. The third experiment proved the concept of the mounting mechanism.

¹<http://www.augenklinik.med.tum.de/>

8. EXPERIMENTS

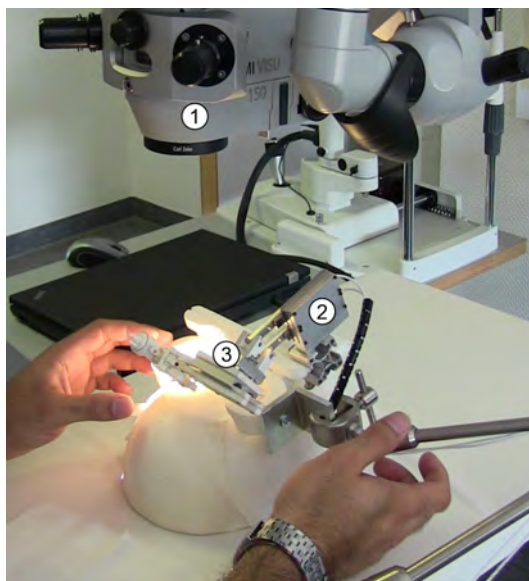


Figure 8.1: PCJM Evaluation, second PCJM segment and the tool gripper are prototypes: 1. microscope, 2. Actuated PCJM, 3. Mockup PCJM

8.2 PCJM Evaluation

Having evaluated the compatibility of the robot in the OR, the feasibility of performing retinal surgery using PCJM components was examined. Two methods were used for these experiments. In the first method a single PCJM was used to move the tooltip in two degrees of freedom; in the second method a 3D prototype of the second PCJM was printed and connected to the real PCJM and the experiments was performed and the motion of the tool tip was captured.

8.3 Robot Evaluation

This section refers to experiments with the completed robot in which all DOFs are actuated and controlled. One euro cent coins were used for the first manipulation tasks (See Figure 8.2) due to the small size (16.25 mm in diameter). The user was asked to move the tooltip along the tree branches on the tail-side of a one cent coin following a desired trajectory. In certain points the user was required to replicate the injection procedure. In the next round of experiments an open pig's eye was used for retinal manipulation. For this set of experiments a deep frozen pig's eye was used. As a result, retinal vessel manipulation was not possible because the retinal membrane was detached.

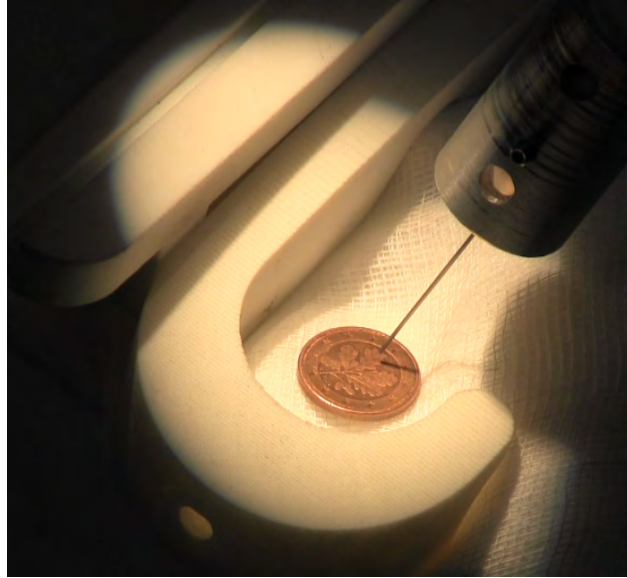


Figure 8.2: Precise motion experiments on one Euro cent coin

8.4 Virtual Fixture Evaluation

This set of experiments did not follow any special procedure for treating diseases within the eye. The aim was to evaluate the virtual fixture approach and implementation. This was done in two experimental sessions at the *Klinikum rechts der Isar*. During the first session important observations were made with the aim of assessing and improving the ongoing development. These observations included:

- Switching from the RCM control mode to the unconstrained mode caused undesired jerks of the end effector. This was related to the fact that during RCM control the position errors of the end effector with respect to the z and y coordinates are not considered. These errors are kept small because of the enforced restriction by the RCM control design. However, by switching to the unconstrained mode where these errors are considered, they are high enough to cause undesired motion.
- The control of the robot with the 3D mouse proved to be too noisy. This was caused by the linear mapping of the displacement of the input device to the desired velocity of the end effector.
- the position of the robot was crucial with respect to the areas covered within the eye, in order to optimize the visibility of the accessible areas.
- for surgeon the position of the needle cannot be intuitively estimated with the microscope alone, because no depth information is available.

The following measures were taken into account for the listed observations:

8. EXPERIMENTS

- to remove the jerks when switching from the RCM control mode to the unconstrained control mode, the most effective method is to take the actual position of the end effector during RCM mode as the desired position for the unconstrained mode. This reduces the error to zero and thus removes undesired movements.
- the linear mapping of the input device was changed to exponential mapping. This greatly contributes to smoother motions of the instrument when controlling it with the 3D mouse.
- in the first experimental session a lookup-table was used for the velocity-to-frequency mapping. To make tracking of a trajectory more accurate, the piezo actuators were examined more closely. This led to the implementation of the polynomial velocity-to-frequency mapping, which is previously presented.
- to increase the reachability within the eye, the position of the robot with respect to the eye was analyzed in-depth. The results from reachability analysis served as the basis for the experiments during the second session.
- the simulation environment was coupled with the software running the low-level control, which should help to obtain a more accurate idea of the needle's position with respect to the background of the eye.

The measures taken were evaluated during the second session. The experiments conducted and their results are presented in the following.

8.4.1 Experimental Setup

Figure 8.3 shows the overall setup at the Department of Ophthalmology at the *Klinikum rechts der Isar*. As previously described, a conventional notebook was used for running the simulation environment and the software for controlling the robot. A 3D mouse connected to the notebook was used as an input device.

The experiments during the second session were conducted with fresh (not from frozen) porcine eyes, which have a similar size and shape to human eyes. The eye was fixed in position using needles on a dummy head and two cannulas were placed on it. During eye surgery one is used as an entry port for the tool and the other one for inserting a device for illuminating the retina. An additional third cannula is usually placed for the insertion of an infusion line to keep the intraocular pressure constant. However, in these experiment this was not necessary. To allow the microscope to focus on the background of the eye, a special lens was placed on top of the cornea. The setting is shown in Figure 8.4.

8.4.2 Experimental Results

The first experiments served mainly to determine the best position of the robot with respect to the eye. It turned out that the goggles had to be removed to place the robot more closely towards the eye. Following reachability analysis, it was concluded that in practice as well as in

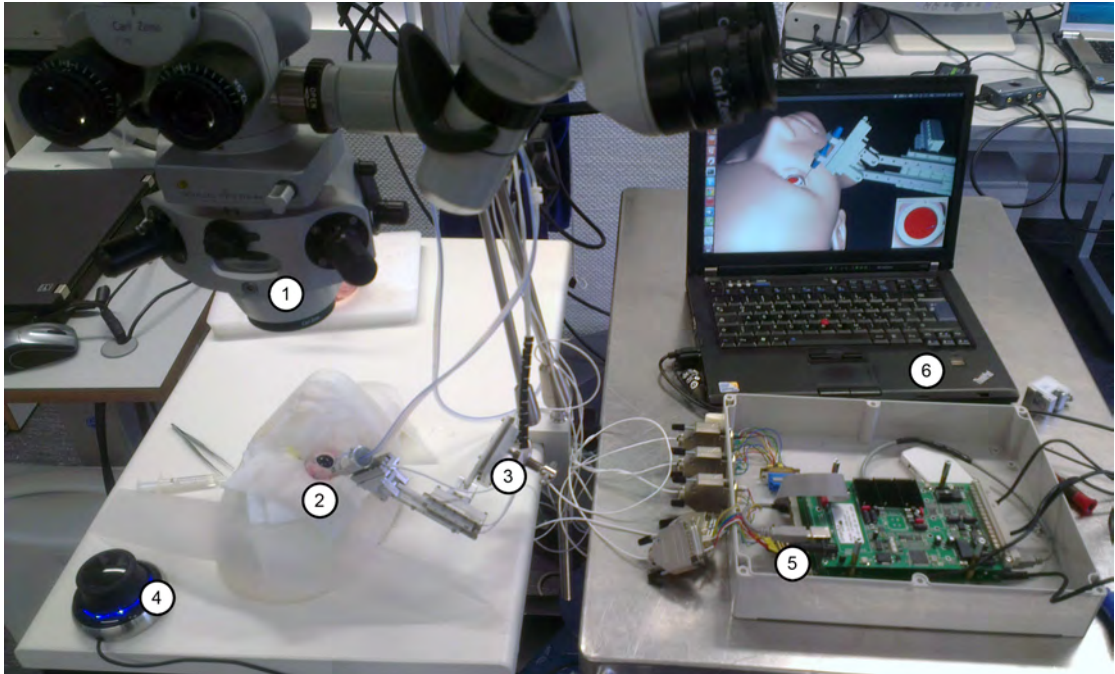


Figure 8.3: The overall setup: 1. microscope, 2. porcine eye fixed in position on the dummy head, 3. robotic assistant, 4. SpaceNavigator 3D mouse, 5. control boards, 6. notebook running the simulation environment and the control software.

the simulation very good results are obtained by tilting the robot by about 30 degrees around the z -axis. Additionally, the robot was placed such that the needle was orthogonal to the surface of the eye as can be seen in Figure 8.3. All linear actuators were put into the zero (reference) position except for the last link which was moved to -13mm and the needle was placed exactly at the entry point (see also Figure 8.4).

Figure 8.5 shows a sequence of images taken from a video during one very successful test run lasting for more than six minutes. During this experiment the remote center-of-motion was set at the beginning and the retina was touched several times. Because the eye was fixed in position with needles, no rotation of the eye was possible. Therefore, the RCM was not changed during the whole procedure.

In this experiment some very important results were gathered. Figure 8.6(a) and Figure 8.6(b) show the trajectory within the eye and Figure 8.6(c) the trajectory without the eye superimposed. The position of the eye was roughly estimated and in this case is only a visual help. The red circles indicate where contact with the retina was made. The blue circle indicates the position of the RCM. Figure 8.6(d) shows the needle's position over time in x -direction i.e. how far it reached into the eye. Again, the red circles indicate where contact was made with the retina. The difference in height is due to the curvature of the eye. The maximum absolute translational velocity of the needle was measured as $2.15 \frac{\text{mm}}{\text{s}}$.

8. EXPERIMENTS

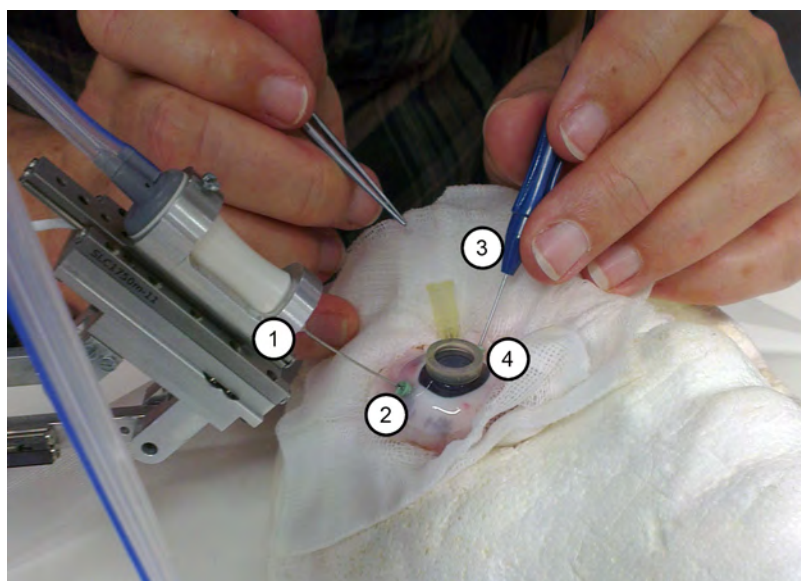


Figure 8.4: The experimental setup: 1. tool gripper, 2. needle placed at the entry point on the surface of the eye, 3. tool for illumination, 4. additional lens for focusing on the retina with the microscope.

Position of the RCM

One important consideration during eye surgery is that the RCM should maintain its position to put minimal stress on the tissue so as not to cause undesired movement of the eye. Figure 8.7 shows the error from the raw position data in the x , y and z -directions during the experiment

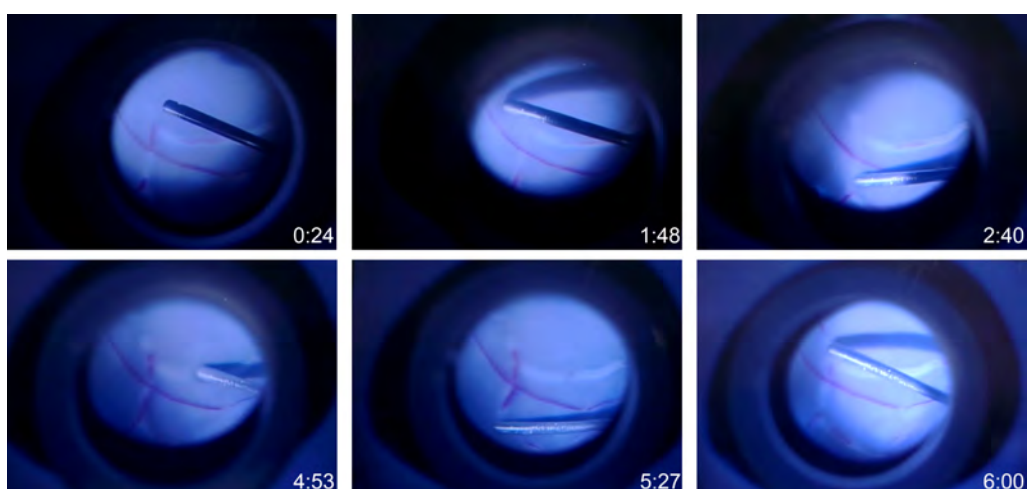
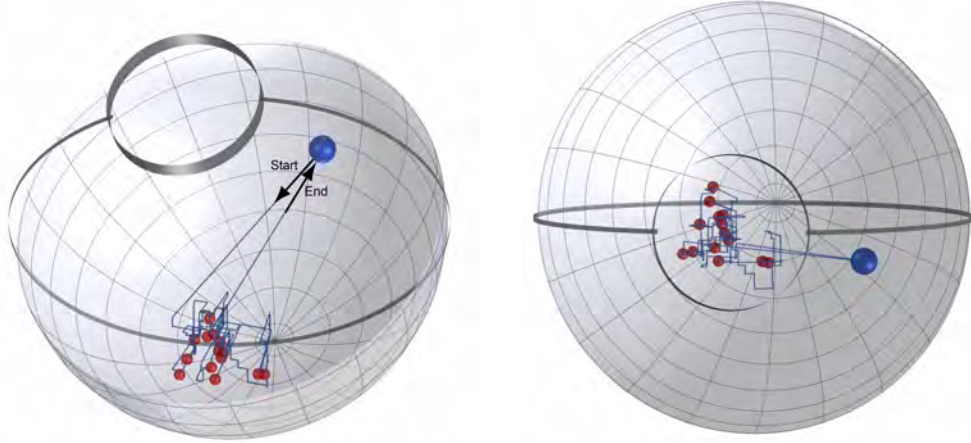
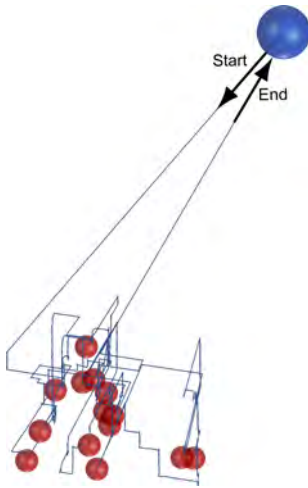


Figure 8.5: Sequence of images from a video taken during one experiment. The retina was touched several times.

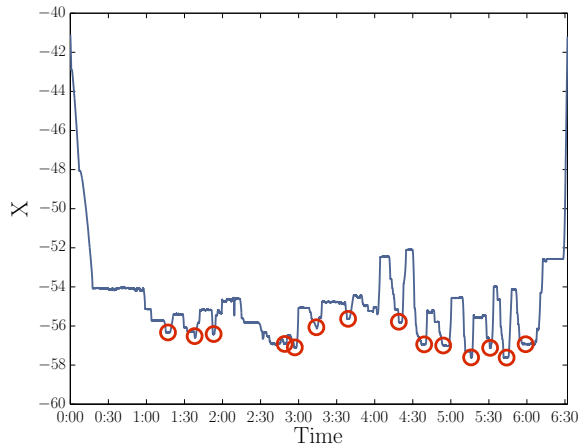


(a) Trajectory followed during one experiment.

(b) Top view of the eye.



(c) The trajectory without the eye.



(d) x -position of the end effector.

Figure 8.6: Trajectory of one experiment lasting for more than six minutes. The red circles indicate where the eye was touched.

previously described. It is seen that only a maximum error of 0.16mm is reached, which is not expected to cause too much stress to the tissue. Then, to assess the stress more accurately, a force sensor would be necessary. To further minimize the error, changes in the control design are necessary, which is discussed in the next paragraph. An interesting observation is that the error in the z -direction corresponds to the error in x -direction. These errors are related to the angular movement around the y -axis of the robot (see Figure 8.7(d)), which causes the RCM to move in the x and z directions. The same effect was not observed when rotating about the

8. EXPERIMENTS

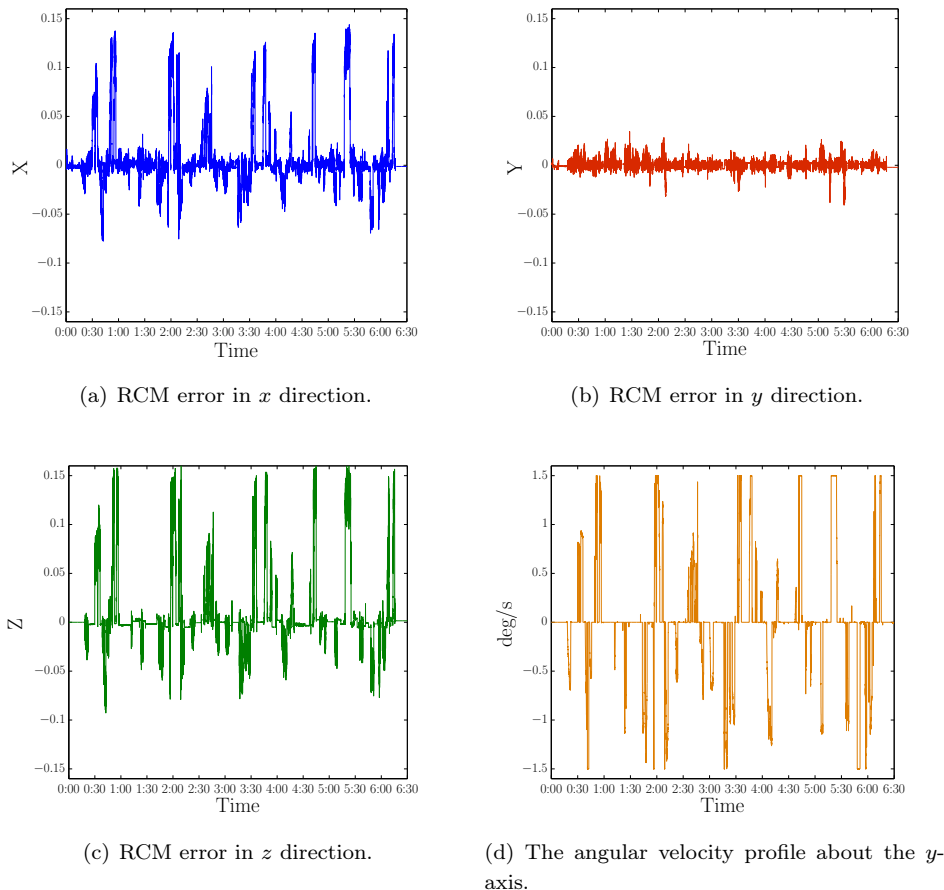


Figure 8.7: The error of the RCM from raw position data of the linear actuators.

z -axis.

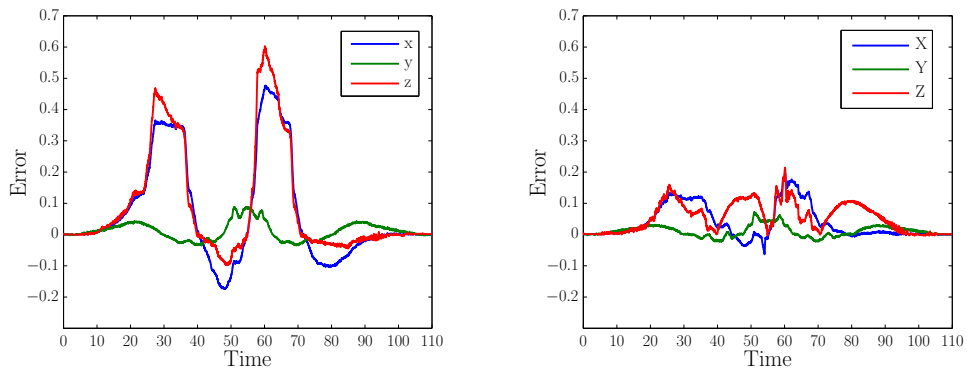
Improvement of Control

For evaluating the tracking error from the previously implemented lookup table and the polynomial mapping, a reference trajectory was used similar to the one previously as mapping discussed. The maximum velocity to be reached was set to $2 \frac{mm}{s}$, as this was also roughly the maximum velocity obtained during the experiments as pointed out before. Figure 8.8(a) and Figure 8.8(b) show the mean tracking error of ten runs and Figure 8.8(c) shows the velocity profile along all three axes.

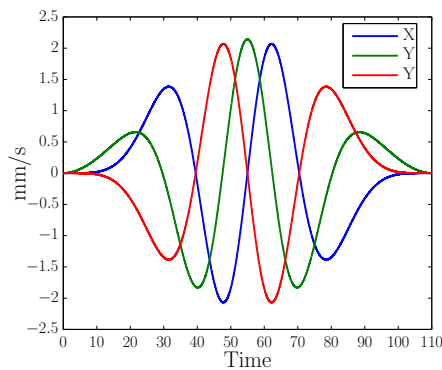
Setting the proportional gains for the control accordingly, the maximum error obtained is significantly reduced with the polynomial mapping. The error peaks are reached when the velocities are the highest as intuition suggests. An interesting observation is that the error in the z -direction corresponds to the error in the x -direction especially in Figure 8.8(a) and also shows

correlation with Figure 8.8(b). The reasons for this effect maybe the same as with the error of the position of the RCM.

For more accurate tracking a differential term in the control law would be beneficial, but tests showed that this did not lead to improvements with the current setup. One reason for this is that the serial-over-USB connection does not allow real-time control and due to the fact that the software running on the control boards is proprietary, no information is available as to whether additional latency is added from this side. A more sophisticated approach would be to develop custom control boards running an inner control-loop and an additional outer control-loop on another device. This is also referred to as cascaded control.



(a) Tracking error obtained with the lookup-table. (b) Tracking error obtained with the polynomial mapping.



(c) The velocity profile in x,y and z -direction.

Figure 8.8: Comparison of the tracking error with two different velocity-to-frequency mappings.

8. EXPERIMENTS

Further Observations

During the experiments it was observed that the whole area seen through the microscope can be reached by the end effector. Nonetheless, it is recommendable to increase the range of the last link to at least $\pm 20mm$ for more flexibility. Furthermore, during testing and some experiments the software running on the control boards sometimes abruptly terminated and caused the actuator to move on with the current speed. Developing custom control boards to prevent this is an important issue for future development. It was also noticed that different loads can change the behavior of the actuators. In [92] this issue was investigated for the case of one actuator. It would be necessary to perform an in-depth analysis of the current setup. This might lead to a complex dynamic model of the robot and to replacing the current actuators with models that can deal with higher loads.

Chapter 9

Bench to Bedside Translation

This chapter investigates the commercial aspects of the technology described in the previous chapters. These aspects include: social impacts, acceptance of technology by the end users, market potential and competition as well as certification strategies.

9.1 Technology and Value Proposition

The value proposition and the benefit to the customer of the technology described in this thesis were informed by the review of the State of the Art in treatment of Central Retinal Vein Occlusion (CRVO).

Setup developed consists of four elements: 1) The robot, 2) The input device, 3) controllers and 4) The real time simulator. The robot, equipped with a conventional surgical tool, is mounted on the operation table. The mounting mechanism fixes the patient's head with respect to the table. The surgeon controls the robot using an intuitive input device while looking through the ophthalmic microscope. Meanwhile the real time simulation visualizes the surgical site for the surgeon with augmented reality. The particular advantage of this technology is the novel and simple kinematics which, due to the usage of the piezo motors, allows the robot to be miniaturized and mounted onto the patient's head. The setup offers around 5 micron precision, which is around 20 times better than a human surgeon. Considering all these features, such a setup is promising for realization of CRVO treatment, which is not feasible by contemporary methods.

9.2 End User Benefits

In the literature it was concluded that the injection of rt-PA is the most promising method of solving RVO. But due to the human motor limitations of the surgeons, rt-PA injection directly into the retinal blood vessels is yet not possible. The robot developed fills this gap and provides a direct-single injection solution for RVO treatment. Such a setup in ophthalmic

9. BENCH TO BEDSIDE TRANSLATION

surgery opens new avenues for treatment of diseases such as RVO and will also up-skill the surgeons in performing other intra-ocular operations. RVO treatment is expected to provide a route to market for this robot, as it is essentially the only clinically compatible system for such a treatment.

9.3 Target Market and Market Size

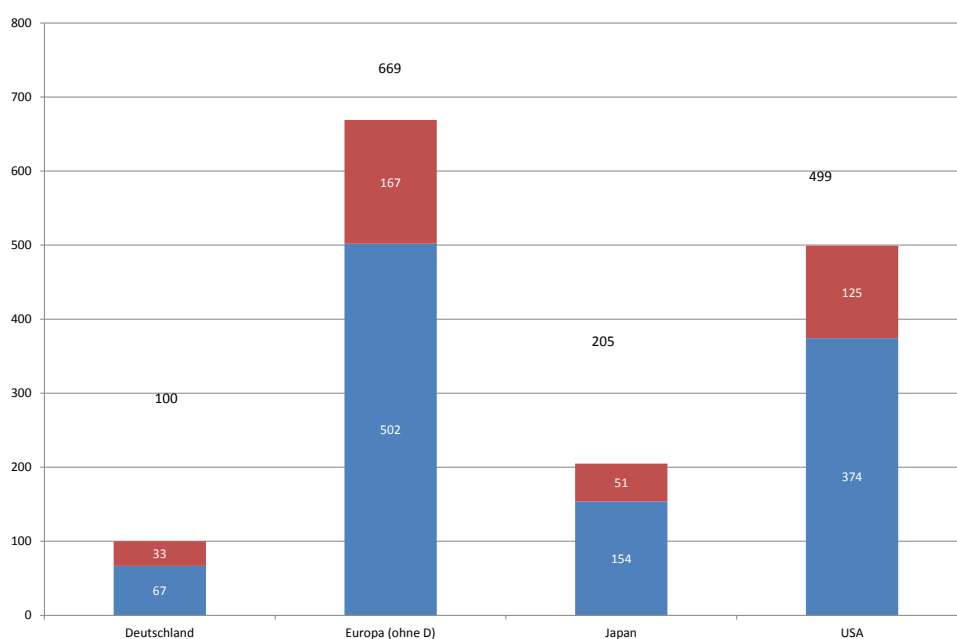


Figure 9.1: Number of new patients diagnosed with Retinal Vein Occlusion per year (x1000):patients with Central Retinal Vein Occlusion are shown in red and the patient with Branch Retinal Vein Occlusion are shown in blue

The following market analysis provides the basis for the market entry strategy in the area of Robot-assisted retinal vein cannulation.

Around 100,000 patients in Germany are diagnosed with CRVO every year (See Figure 9.1¹). Specialized eye clinics are these patients' contact points with ophthalmologists. Around 100 clinics in Germany provide secondary treatments for CRVO; these clinics are identified as potential customers for the proposed setup in this country. If it can be assumed that the patients are roughly evenly distributed between clinics, i.e. 1000 patients per clinic, an average of five CRVO operations would need to be performed per day.

In the medical device industry products are mainly acquired by purchase²; lease for rental

¹The burden of disease of retinal vein occlusion: review of the literature - Eye (2011) 25, 981-988

²(K. Traub, December 5, 2012)

of medical devices are less common, according to expert interviews¹. Figure 9.2 Shows the potential market for Europe, Japan and the US.

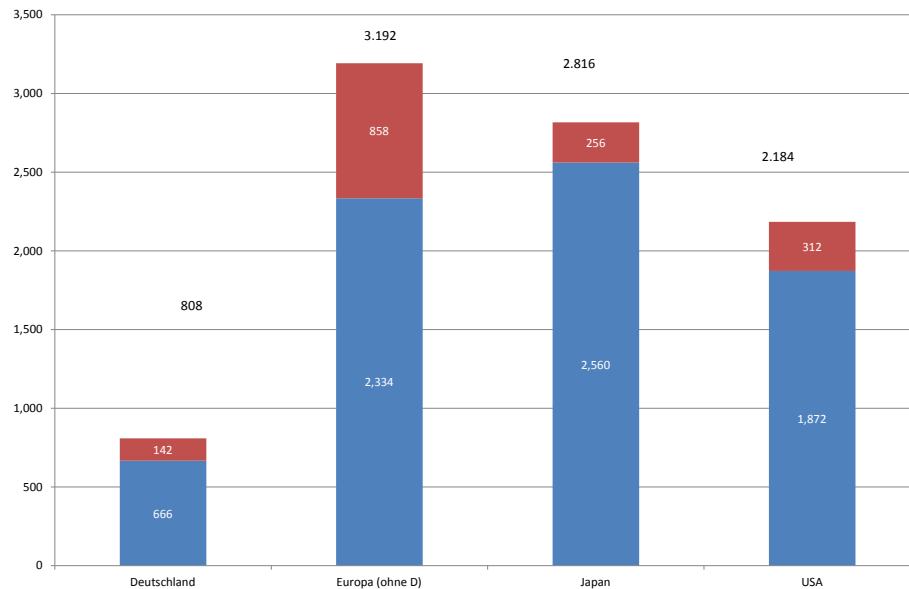


Figure 9.2: Total number of patients suffering from Retinal Vein Occlusion (X1000):patients with Central Retinal Vein Occlusion are shown in red and patients with Branch Retinal Vein Occlusion are shown in blue

9.4 Stakeholders

Customer: Medical devices occupy a unique position in the market. Although the clinics are the main customers of the devices, the surgeons make the choice. Therefore, customer acquisition should be prioritized on the grounds of surgeons' satisfaction. The only aspect which the clinics take into account is the cost-effectiveness, due to the fact that their financial resources are limited.

State: Medical technology market, worldwide, is highly regulated. In the U.S. certification is administrated by Food and Drug Administration (FDA), in Japan by the Pharmaceuticals and Medical Devices Agency (PMDA), and in Europe is under jurisdiction of the Conformance Europeenne (CE). The certification process verifies and confirms the safety of a product for humans and the environment. The certification of the medical devices, regardless of the region, is mandatory. However, the type of certification, depending on the functionality of the device, varies. CE certification in Europe is carried out by an authorized approval body, such as the

¹Personal meeting with M. Struppe, November, 28, 2012 and J. Traub, 5. December 2012

9. BENCH TO BEDSIDE TRANSLATION

Technical Inspection Association (TUV) in Germany. ISO 14981 (Application of risk management to medical devices) requires a risk assessment (Hazard Analysis). The most common tool is a Failure Modes Effects Analysis (FMEA) or a Failure Modes Effects and Criticality Analysis (FMECA) which are both defined in IEC 60812.

The implementation of FMEA and FMECA should begin early in the design phase and evolve as hazards are identified as methods of control are developed. Since many technical adaptations of the product are required to obtain, it is wise to carry out the product approval process in parallel to development. The individual requirements for certification are well documented and are freely available from the authorized agencies. An essential process step is the risk analysis for the classification of the medical device in one of the risk classes (I - II - III, for FDA and I - IIa - IIb - III for CE). The functionality of the proposed setup of this work has been analyzed by experts and the setup is recognized as a Class IIb device, i.e. a device with a high level of risk but not implantable or in direct contact with human body tissue ¹. For approval of products in the risk class IIb category, clinical trials as a basis for the evaluation of the safety and efficacy are required ². In order to validate the results, the clinical trial must be conducted at independent clinics³. For class III devices, Pre-Market Approval (PMA) is also needed. An alternative for bringing a new medical device to market in the US is to aim for the 510(k) method which describes a device as “substantially equivalent” to a previous legally marketed device. In addition to product registration, Intellectual Property considerations such as patent and utility model protection play an important role in all countries, especially in the target markets, due to the existence of competition.

Strategic Partners: Due to the complex market structures in the medical technology domain, collaborations for startups are extremely valuable. Eye clinics should be included as early as possible in the development loop and may conduct the clinical trials from the very early stages. Surgeons will not only provide valuable customer feedback, but will also add necessary medical knowledge. Furthermore, complicated and costly product certification approval of such setups requires research associations or non-profit organizations as strategic partners. Organizations which are active in certification, funding organizations and pharmaceutical companies (specially manufacturers of rt-PA) could be potential strategic partners. In order to achieve cost benefits and long-term focus on the core competence of the development of the technology, distribution partners are also regarded as important partners.

¹Personal interview: J. Spaeth, personal interview, 5. December 2012; M. Struppe, personal interview, 28. November 2012; J. Traub, personal interview, 5. December 2012

² Institut der deutschen Wirtschaft Köln, 2010; Luntz and Schroeder, 2009

³J. Traub, personal interview, December 5, 2012

Chapter 10

Conclusion and future work

This chapter summarises the roadmap of the ‘Hybrid Parallel-Serial Micromanipulator to Assist Ophthalmic Surgery’. In addition, the scope for further work addressing open research questions will be investigated.

10.1 Conclusion

This thesis has described the design and development of a robot to assist in vitreo-retinal surgery. The setup addressed Retinal Vein Occlusion (RVO), a currently untreatable retinal disease affecting more than 16 million patients. The robot developed during the course of this work assists the surgeon performing the treatment and enhances precision and dexterity to such an extent, that this form of surgery may now become clinically viable. The first step in designing a clinically adoptable setup was a precise definition of the clinical requirements. In this work the requirements were defined by: 1) Studying the anatomy of the eye as well as gaining an understanding of the disease, 2) Quantitative observation of surgeons’ motions during conventional ophthalmic surgery by means of an electromagnetic tracking setup, 3) Modeling the eye by considering the mechanical characteristics of its tissue and muscles. Following these steps, the requirements of the robot for such an operation were listed. This information was later used to design the system and finally for evaluation purposes. The first design step was the preparation of an early stage prototype. This prototype was evaluated by expert surgeons in order that they may be involved from the beginning of the design phase. Taking the feedback of the surgeons into consideration was the initial design point for the second prototype. The next milestone was the invention of the parallel coupled joint mechanism (PCJM). PCJM was proven to be a compact and precise joint mechanism for the robot. The PCJM design and evaluation encompassed mathematical modeling, CAD design, kinematic analysis and experimental evaluations. After the successful evaluation of the PCJM in clinical environments, a serial configuration was designed. The kinematics of the micromanipulator developed was evaluated under several different evaluation criteria and was modified accordingly. Mathematical modeling, CAD modeling and kinematic analysis of the entire manipulator was carried out,

10. CONCLUSION AN FUTURE WORK

similar to that of the individual PCJMs. Following the successful proof of the kinematic concept, dynamic analysis was performed as a stepping stone towards system control. In parallel to the dynamic analysis, fabrication of the robot was carried out. Based on the aforementioned analysis, requirements and the hardware features, the micromanipulator controller was designed and the beta version of the software architecture was released. The simulation environment was integrated into the software architecture. The purpose of the simulation environment was to simplify evaluation of the control and software as well as to provide a training platform for surgeons to practise robotic surgery, before using the robot. The “bench-to-bedside” implementation of the robot was considered with a view to making it OR-compatible. The park position of the robot is when it is folded under the operation table below the patient’s head. When the surgeon needs an augmented manipulation using the robot, the robot is unfolded from the park position, mounted and fixed it on the patient head, and the input device is used to control the robot and move the tool inside the eye. Clinical trials on animals’ eyes were performed successfully and initial steps for certification and commercialization were taken.

10.2 Future work

There are still open research questions in the domain of robot assisted eye surgery which present opportunities for future work carrying on from this thesis. For example, design and fabrication of a suitable micro-needle for retinal vein cannulation is one such interesting research area. The current needles have limitations such as the size, tool-tip shape and stiffness. Such a needle is attached to the end effector of the robot and is controlled by the surgeon. Such a needle (micro-pipette) should be less than $20\mu m$ in diameter and should be designed in such a way as to enable correct orientation with respect to the vein for injection. Furthermore, integration of intra-ocular imaging techniques such as Optical Coherence Tomography (OCT) will be helpful for robot path planing and navigation. Visual feedback from the microscope cannot give the surgeon a precise information; specifically it is difficult for surgeons to measure the depth of the tool and the the distance between the tool tip and retina. Additionally, in order to provide higher precision of the PCJM mechanical structures one can fabricate both parallel piezo actuators as a single part, which has the added advantage of reducing the costs.

10.3 Concluding Remarks

A hybrid parallel-serial micromanipulator was developed, the relevant controller was designed and the software architecture was implemented. A compact, intuitive and clinically adoptable surgical robot as small as an average surgeon’s hand, along with a sophisticated simulation environment, were the products of this research. The augmentation of human skill with robotic precision enables groundbreaking surgical techniques which promise a brighter future for patients with untreatable eye conditions.

References

- [1] SMARACT GMBH. *Product Catalogue*, **13**. 2013. http://www.smaract.de/FTP/SmarAct_Catalogue__vol13.pdf. Last accessed: December 10, 2013. viii, xi, 73
- [2] S. NAIR, M. ALI. NASSERI, M. EDER, C. P. LOHMANN, AND A. KNOLL. **Embedded Middleware and Hard Real-time based Architecture for Robot Assisted Ophthalmic Surgery**. In *The Hamlyn Symposium on Medical Robotics*, 2013. ix, 96, 98, 99, 100
- [3] B. SICILIANO AND O. KHATIB, editors. *Springer Handbook of Robotics*. Springer, 2008. 3
- [4] S. RIZZO, F. PATELLI, AND D. CHOW. *Vitreo-retinal Surgery: Progress III*. Essentials in Ophthalmology. Springer Verlag, 2008. 4, 5, 50
- [5] R. MACHERNER. **The development of pars plana vitrectomy: a personal account**. *Graefe's archive for clinical and experimental ophthalmology*, **233**(8):453–468, 1995. 4
- [6] G. DOGANGIL, O. ERGENEMAN, JAKE J. ABBOTT, SA. PANÁĀĒ, H. HALL, S. MUNTWYLER, AND B. J. NELSON. **Toward Targeted Retinal Drug Delivery with Wireless Magnetic Microrobots**. *2008 IEEE/RSJ International Conference on Intelligent Robots and Systems*, 2008. 6, 7
- [7] L. O. HATTENBACH, J. PUCHTA, AND I. HILGENBERG. **Experimental Endoscopic Endovascular Cannulation: A Novel Approach to Thrombolysis in Retinal Vessel Occlusion**. *Retina*, 2011. 6, 7, 8, 9, 10
- [8] C. J. POURNARAS AND I. K. PETROPOULOS. **The rationale of retinal endovascular fibrinolysis in the treatment of retinal vein occlusion**. *Retina*, 2012. 6, 8, 9, 10
- [9] O. ERGENEMAN, J. POKKI, V. POCEPCOVA, J. J. ABBOTT, H. HALL, AND B. J. NELSON. **Characterization of Puncture Forces for Retinal Vein Cannulation**. *Journal of Medical Devices*, 2011. 7
- [10] S. P. N. SINGHY AND C. N. RIVIERE. **Physiological tremor amplitude during retinal microsurgery**. In *Bioengineering Conference, 2002. Proceedings of the IEEE 28th Annual Northeast*, pages 171–172. IEEE, 2002. 10, 21

REFERENCES

- [11] R.H. TAYLOR, B.D. MITTELSTADT, H.A. PAUL, W. HANSON, P. KAZANZIDES, J.F. ZUHARS, B. WILLIAMSON, B.L. MUSITS, E. GLASSMAN, AND W.L. BARGAR. **An image-directed robotic system for precise orthopaedic surgery.** *Robotics and Automation, IEEE Transactions on*, **10**(3):261–275, 1994. 13
- [12] Y.S. KWON, J. HOU, E.A. JONCKHEERE, AND S. HAYATI. **A robot with improved absolute positioning accuracy for CT guided stereotactic brain surgery.** *Biomedical Engineering, IEEE Transactions on*, **35**(2):153–160, 1988. 13
- [13] B. DAVIES. **Robotics in minimally invasive surgery.** In *Through the Keyhole: Microengineering in Minimally Invasive Surgery, IEE Colloquium on*, page 5/1â5/2, 1995. 13
- [14] A. GUERROUAD AND P. VIDAL. **SMOS: stereotaxical microtelemanipulator for ocular surgery.** In *Engineering in Medicine and Biology Society, 1989. Images of the Twenty-First Century., Proceedings of the Annual International Conference of the IEEE Engineering in*, pages 879–880 vol.3, 1989. 14, 15
- [15] S. CHARLES, H. DAS, T. OHM, C. BOSWELL, G. RODRIGUEZ, R. STEELE, AND D. IS-TRATE. **Dexterity-enhanced telerobotic microsurgery.** In *Advanced Robotics, 1997. ICAR '97. Proceedings., 8th International Conference on*, pages 5–10, 1997. 14, 15
- [16] WEI WEI, R. GOLDMAN, N. SIMAAN, H. FINE, AND STANLEY CHANG. **Design and Theoretical Evaluation of Micro-Surgical Manipulators for Orbital Manipulation and Intraocular Dexterity.** In *Robotics and Automation, 2007 IEEE International Conference on*, pages 3389–3395, 2007. 14, 16
- [17] K.W. GRACE, J.E. COLGATE, M.R. GLUCKSBERG, AND J.H. CHUN. **A six degree of freedom micromanipulator for ophthalmic surgery.** In *Robotics and Automation, 1993. Proceedings., 1993 IEEE International Conference on*, pages 630–635 vol.1, 1993. 15
- [18] D-Y YU, SJ CRINGLE, AND IJ CONSTABLE. **Robotic ocular ultramicrosurgery.** *Australian and New Zealand journal of ophthalmology*, **26**(S1):S6–S8, 1998. 15
- [19] P. S JENSEN, K. W GRACE, R. ATTARIWALA, J E. COLGATE, AND M. R GLUCKSBERG. **Toward robot-assisted vascular microsurgery in the retina.** *Graefe's archive for clinical and experimental ophthalmology*, **235**(11):696–701, 1997. 15
- [20] Y. IDA, N. SUGITA, T. UETA, Y. TAMAKI, K. TANIMOTO, AND M. MITSUISHI. **Micro-surgical robotic system for vitreoretinal surgery.** *International journal of computer assisted radiology and surgery*, **7**(1):27–34, 2012. 15
- [21] T. UETA, Y. YAMAGUCHI, Y. SHIRAKAWA, T. NAKANO, R. IDETA, Y. NODA, A. MORITA, R. MOCHIZUKI, N. SUGITA, M. MITSUISHI, ET AL. **Robot-assisted vitreoretinal surgery: development of a prototype and feasibility studies in an animal model.** *Ophthalmology*, **116**(8):1538–1543, 2009. 15

-
- [22] T. NAKANO, N. SUGITA, T. UETA, Y. TAMAKI, AND M. MITSUISHI. **A parallel robot to assist vitreoretinal surgery.** *International journal of computer assisted radiology and surgery*, **4**(6):517–526, 2009. 15
- [23] W. WEI, C. POPPLEWELL, S. CHANG, H. F FINE, AND N. SIMAAN. **Enabling Technology for Microvascular Stenting in Ophthalmic Surgery.** *Transactions of the ASME-W-Journal of Medical Devices*, **4**(1):014503, 2010. 16
- [24] W. WEI, R. E GOLDMAN, H. F FINE, S. CHANG, AND N. SIMAAN. **Performance evaluation for multi-arm manipulation of hollow suspended organs.** *Robotics, IEEE Transactions on*, **25**(1):147–157, 2009. 16
- [25] J-L BOURGES, J-P HUBSCHMAN, J. WILSON, S. PRINCE, T-C TSAO, AND S. SCHWARTZ. **Assessment of a Hexapod Surgical System for Robotic Micro-Macro Manipulations in Ocular Surgery.** *Ophthalmic Research*, **46**(1):25–30, 2010. 16
- [26] R. HENDRIX. *Robotically assisted eye surgery: A haptic master console.* PhD thesis, PhD thesis defended, Eindhoven University, 2011. 16
- [27] P. KUMAR, R. AND BERKELMAN, P. GUPTA, A. BARNES, P. S. JENSEN, L. WHITCOMB, AND R. H. TAYLOR. **Preliminary experiments in cooperative human/robot force control for robot assisted microsurgical manipulation.** In *Robotics and Automation, 2000. Proceedings. ICRA'00. IEEE International Conference on*, **1**, pages 610–617. IEEE, 2000. 18, 19
- [28] B. MITCHELL, J. KOO, I. IORDACHITA, P. KAZANZIDES, A. KAPOOR, J. HANDA, G. HAGER, AND R. H. TAYLOR. **Development and application of a new steady-hand manipulator for retinal surgery.** In *Robotics and Automation, 2007 IEEE International Conference on*, pages 623–629. IEEE, 2007. 18, 19, 97
- [29] A. UNERI, M. BALICKI, J. HANDA, P. GEHLBACH, R. H TAYLOR, AND I. IORDACHITA. **New steady-hand eye robot with micro-force sensing for vitreoretinal surgery.** In *Biomedical Robotics and Biomechatronics (BioRob), 2010 3rd IEEE RAS and EMBS International Conference on*, pages 814–819. IEEE, 2010. 18, 19, 20
- [30] M. BALICKI, J-H HAN, I. IORDACHITA, P. GEHLBACH, J. HANDA, R. H. TAYLOR, AND J. KANG. **Single fiber optical coherence tomography microsurgical instruments for computer and robot-assisted retinal surgery.** In *Medical Image Computing and Computer-Assisted Intervention–MICCAI 2009*, pages 108–115. Springer, 2009. 19
- [31] I. FLEMING, M. BALICKI, J. KOO, I. IORDACHITA, B. MITCHELL, J. HANDA, G. HAGER, AND R. H. TAYLOR. **Cooperative robot assistant for retinal microsurgery.** In *Medical Image Computing and Computer-Assisted Intervention–MICCAI 2008*, pages 543–550. Springer, 2008. 19

REFERENCES

- [32] R. H. TAYLOR AND D. STOIANOVICI. **Medical robotics in computer-integrated surgery.** *Robotics and Automation, IEEE Transactions on*, **19**(5):765–781, 2003. 19
- [33] D. KRAGIC, P. MARAYONG, M. LI, A. M. OKAMURA, AND G. D. HAGER. **Human-machine collaboratimaclachlan2012microne systems for microsurgical applications.** *The international journal of robotics research*, **24**(9):731–741, 2005. 19
- [34] R. H. TAYLOR, J. FUNDA, B. ELDRIDGE, S. GOMORY, K. GRUBEN, D. LAROSE, M. TALAMINI, L. KAVOUSSI, AND J. ANDERSON. **A telerobotic assistant for laparoscopic surgery.** *Engineering in Medicine and Biology Magazine, IEEE*, **14**(3):279–288, 1995. 19
- [35] R. H. TAYLOR, P. JENSEN, L. WHITCOMB, A. BARNES, R. KUMAR, D. STOIANOVICI, P. GUPTA, Z. WANG, E. DEJUAN, AND L. KAVOUSSI. **A steady-hand robotic system for microsurgical augmentation.** *The International Journal of Robotics Research*, **18**(12):1201–1210, 1999. 19
- [36] R. H. TAYLOR AND L. JOSKOWICZ. **Computer-integrated surgery and medical robotics.** *Standard Handbook of Biomedical Engineering and Design, 2nd edn*, New York, NY: McGraw Hill, pages 29–3, 2003. 19
- [37] W. T. ANG. *Active tremor compensation in handheld instrument for microsurgery.* PhD thesis, Carnegie Mellon University, the Robotics Institute, 2004. 19
- [38] J. C. TABARÉS, R. A. MACLACHLAN, C. A. ETTENSOHN, AND C. N. RIVIERE. **Cell micromanipulation with an active handheld micromanipulator.** In *Engineering in Medicine and Biology Society (EMBC), 2010 Annual International Conference of the IEEE*, pages 4363–4366. IEEE, 2010. 19
- [39] W. T. ANG, C. N. RIVIERE, AND P. K. KHOSLA. **An active hand-held instrument for enhanced microsurgical accuracy.** In *Medical Image Computing and Computer-Assisted Intervention–MICCAI 2000*, pages 878–886. Springer, 2000. 19
- [40] L. DENG AND Y. TAN. **Modeling of rate-dependent hysteresis in piezoelectric actuators.** In *Control Applications, 2008. CCA 2008. IEEE International Conference on*, pages 978–982. IEEE, 2008. 19
- [41] W. T. ANG, S. Y. KHOO, P. K. KHOSLA, AND C. N. RIVIERE. **Physical model of a MEMS accelerometer for low-g motion tracking applications.** In *Robotics and Automation, 2004. Proceedings. ICRA'04. 2004 IEEE International Conference on*, **2**, pages 1345–1351. IEEE, 2004. 19
- [42] W. T. LATT, U-X TAN, C. Y. SHEE, C. N. RIVIERE, AND W. T. ANG. **Compact sensing design of a handheld active tremor compensation instrument.** *Sensors Journal, IEEE*, **9**(12):1864–1871, 2009. 19

-
- [43] B. C. BECKER, S. VOROS, R. A. MACLACHLAN, G. D. HAGER, AND C. N. RIVIERE. **Active guidance of a handheld micromanipulator using visual servoing.** In *Robotics and Automation, 2009. ICRA'09. IEEE International Conference on*, pages 339–344. IEEE, 2009. 19
- [44] W. T. ANG, C. N. RIVIERE, AND P. K. KHOSLA. **Design and implementation of active error canceling in hand-held microsurgical instrument.** In *Intelligent Robots and Systems, 2001. Proceedings. 2001 IEEE/RSJ International Conference on*, **2**, pages 1106–1111. IEEE, 2001. 19
- [45] C. N. RIVIERE, W. T. ANG, AND P. K. KHOSLA. **Toward active tremor canceling in handheld microsurgical instruments.** *Robotics and Automation, IEEE Transactions on*, **19**(5):793–800, 2003. 19
- [46] W. T. ANG AND C. N. RIVIERE. **Neural network methods for error canceling in human-machine manipulation.** In *Engineering in Medicine and Biology Society, 2001. Proceedings of the 23rd Annual International Conference of the IEEE*, **4**, pages 3462–3465. IEEE, 2001. 19
- [47] R. A. MACLACHLAN, B. C. BECKER, JAIME CUEVAS T., G. W. PODNAR, L. A. LOBES, AND C. N. RIVIERE. **Micron: an actively stabilized handheld tool for microsurgery.** *Robotics, IEEE Transactions on*, **28**(1):195–212, 2012. 19, 20
- [48] W. T. ANG, P. K. KHOSLA, AND C. N. RIVIERE. **Kalman filtering for real-time orientation tracking of handheld microsurgical instrument.** In *Intelligent Robots and Systems, 2004.(IROS 2004). Proceedings. 2004 IEEE/RSJ International Conference on*, **3**, pages 2574–2580. IEEE, 2004. 19
- [49] F. A. GARMÓN, W. T. ANG, PK KHOSLA, AND C. N. RIVIERE. **Rate-dependent inverse hysteresis feedforward controller for microsurgical tool.** In *Engineering in Medicine and Biology Society, 2003. Proceedings of the 25th Annual International Conference of the IEEE*, **4**, pages 3415–3418. IEEE, 2003. 19
- [50] W. T. ANG, P. K. KHOSLA, AND C. N. RIVIERE. **An intelligent hand-held microsurgical instrument for improved accuracy.** In *Engineering in Medicine and Biology Society, 2001. Proceedings of the 23rd Annual International Conference of the IEEE*, **4**, pages 3450–3453. IEEE, 2001. 19
- [51] B. C. BECKER, R. A. MACLACHLAN, G. D. HAGER, AND C. N. RIVIERE. **Handheld micromanipulation with vision-based virtual fixtures.** In *Robotics and Automation (ICRA), 2011 IEEE International Conference on*, pages 4127–4132. IEEE, 2011. 19
- [52] U-X TAN, F. WIDJAJA, W. T. LATT, K. C. VELUVOLU, C. Y. SHEE, C. N. RIVIERE, AND W. T. ANG. **Adaptive rate-dependent feedforward controller for hysteretic piezoelectric actuator.** In *Robotics and Automation, 2008. ICRA 2008. IEEE International Conference on*, pages 787–792. IEEE, 2008. 19

REFERENCES

- [53] W. T. ANG, P. PRADEEP, AND C. RIVIERE. **Active tremor compensation in microsurgery.** In *Engineering in Medicine and Biology Society, 2004. IEMBS'04. 26th Annual International Conference of the IEEE*, **1**, pages 2738–2741. IEEE, 2004. 19, 28
- [54] A. D. JAGTAP AND C. N. RIVIERE. **Applied force during vitreoretinal microsurgery with handheld instruments.** In *Engineering in Medicine and Biology Society, 2004. IEMBS'04. 26th Annual International Conference of the IEEE*, **1**, pages 2771–2773. IEEE, 2004. 19
- [55] D. Y. CHOI AND C. N. RIVIERE. **Flexure-based manipulator for active handheld microsurgical instrument.** In *Engineering in Medicine and Biology Society, 2005. IEEE-EMBS 2005. 27th Annual International Conference of the*, pages 2325–2328. IEEE, 2005. 19
- [56] J. G. AVEDILLO, D. Y. CHOI, AND C. N. RIVIERE. **Inverse kinematic model of flexure-based microsurgical manipulator.** In *Engineering in Medicine and Biology Society, 2005. IEEE-EMBS 2005. 27th Annual International Conference of the*, pages 5775–5777. IEEE, 2005. 19
- [57] D. Y. CHOI, R. SANDOVAL, R. A. MACLACHLAN, L. HO, L. A. LOBES, AND C. N. RIVIERE. **Test of tracing performance with an active handheld micromanipulator.** In *Engineering in Medicine and Biology Society, 2007. EMBS 2007. 29th Annual International Conference of the IEEE*, pages 3638–3641. IEEE, 2007. 19
- [58] R. MACLACHLAN AND C. N. RIVIERE. **Optical tracking for performance testing of microsurgical instruments.** 2007. 19
- [59] W. T. ANG, P. K. KHOSLA, AND C. N. RIVIERE. **Feedforward controller with inverse rate-dependent model for piezoelectric actuators in trajectory-tracking applications.** *Mechatronics, IEEE/ASME Transactions on*, **12**(2):134–142, 2007. 19
- [60] B. C. BECKER, S. VOROS, L. A. LOBES, J. T. HANDA, G. D. HAGER, AND C. N. RIVIERE. **Retinal vessel cannulation with an image-guided handheld robot.** In *Engineering in Medicine and Biology Society (EMBC), 2010 Annual International Conference of the IEEE*, pages 5420–5423. IEEE, 2010. 19
- [61] B. C. BECKER, R. A. MACLACHLAN, L. A. LOBES, AND C. N. RIVIERE. **Semiautomated intraocular laser surgery using handheld instruments.** *Lasers in surgery and medicine*, **42**(3):264–273, 2010. 19
- [62] T. MEENINK. *Vitreo-retinal eye surgery robot: sustainable precision.* PhD thesis, PhD thesis defended, Eindhoven University, 31 October, 2011. 20, 50
- [63] L. F. HOTRAPHINYO AND C. N. RIVIERE. **Three-dimensional accuracy assessment of eye surgeons.** In *Engineering in Medicine and Biology Society, 2001. Proceedings of the 23rd Annual International Conference of the IEEE*, **4**, pages 3458–3461. IEEE, 2001. 21

-
- [64] C. N. RIVIERE AND P. S. JENSEN. **A study of instrument motion in retinal microsurgery.** In *Engineering in Medicine and Biology Society, 2000. Proceedings of the 22nd Annual International Conference of the IEEE*, **1**, pages 59–60. IEEE, 2000. 21
- [65] B. C. BECKER, H. TUMMALA, AND C. N. RIVIERE. **Autoregressive modeling of physiological tremor under microsurgical conditions.** In *Engineering in Medicine and Biology Society, 2008. EMBS 2008. 30th Annual International Conference of the IEEE*, pages 1948–1951. IEEE, 2008. 21
- [66] U-X TAN, K. C. VELUVOLU, W. T. LATT, C. Y. SHEE, C. N. RIVIERE, AND W. T. ANG. **Estimating displacement of periodic motion with inertial sensors.** *Sensors Journal, IEEE*, **8**(8):1385–1388, 2008. 21
- [67] D. O. IBÁÑEZ, F. P. BAQUERÍN, D. Y. CHOI, AND C. N. RIVIERE. **Performance envelope and physiological tremor in microsurgery.** In *Bioengineering Conference, 2006. Proceedings of the IEEE 32nd Annual Northeast*, pages 121–122. IEEE, 2006. 21
- [68] M. ALI NASSERI, E. C. DEAN, S. NAIR, M. EDER, M. KNOLL, A. AND MAIER, AND C. P. LOHMANN. **Clinical motion tracking and motion analysis during ophthalmic surgery using electromagnetic tracking system.** In *Biomedical Engineering and Informatics (BMEI), 2012 5th International Conference on*, pages 1058–1062. IEEE, 2012. 22, 23, 27, 28
- [69] J. B. HUMMEL, M. R. BAX, M. L. FIGL, Y. KANG, MAURER J. C., W. W. BIRKFELLNER, H. BERGMANN, AND R. SHAHIDI. **Design and application of an assessment protocol for electromagnetic tracking systems.** *Medical physics*, **32**:2371, 2005. 23
- [70] Z. ZHANG. **Flexible camera calibration by viewing a plane from unknown orientations.** In *Computer Vision, 1999. The Proceedings of the Seventh IEEE International Conference on*, **1**, pages 666–673. Ieee, 1999. 25
- [71] S. SCHUTTE, S. P. VAN DEN BEDEM, F. VAN KEULEN, F. C. VAN DER HELM, AND H. J. SIMONSZ. **A finite-element analysis model of orbital biomechanics.** *Vision research*, **46**(11):1724–1731, 2006. 30, 31, 33
- [72] Z. YIYI, W. GUANGZHI, D. HUI, AND J. YONGHONG. **Finite Element Modeling and Biomechanical Analysis of Eyeball and Extraocular Muscles.** In *Engineering in Medicine and Biology Society, 2005. IEEE-EMBS 2005. 27th Annual International Conference of the*, pages 4978–4981. IEEE, 2006. 30, 32
- [73] E. UCHIO, S. OHNO, J. KUDOH, K. AOKI, AND L. T. KISIELEWICZ. **Simulation model of an eyeball based on finite element analysis on a supercomputer.** *British Journal of Ophthalmology*, **83**(10):1106–1111, 1999. 30
- [74] R. E. NORMAN, J. G. FLANAGAN, I. A. SIGAL, S. M. RAUSCH, I. TERTINEGG, AND C. R. ETHIER. **Finite element modeling of the human sclera: influence on**

REFERENCES

- optic nerve head biomechanics and connections with glaucoma. *Experimental eye research*, **93**(1):4–12, 2011. 30
- [75] Q. WEI, S. SUEDA, AND D. K. PAI. **Biomechanical simulation of human eye movement**. In *Biomedical Simulation*, pages 108–118. Springer, 2010. 30, 50
- [76] D. KLEUT, M. JOVANOVIĆ, AND B. D. RELJIN. **3D Visualisation of MRI images using MATLAB**. *Journal of Automatic Control*, **16**(1):1–3, 2006. 30, 32, 33
- [77] J. WU, M. ALI NASSERI, M. EDER, M. A. GAVALDON, C. P. LOHMANN, AND A. KNOLL. **The 3D Eyeball FEA Model with Needle Rotation**. *APCBEE Procedia*, **7**:4–10, 2013. 31, 32, 35
- [78] V. MANJUNATH, M. TAHA, J. G. FUJIMOTO, AND J. S. DUKER. **Choroidal thickness in normal eyes measured using Cirrus HD optical coherence tomography**. *American journal of ophthalmology*, **150**(3):325–329, 2010. 32, 33
- [79] C. D. CHO, S. K. LEE, AND M. ANSARI. **Hyperelastic muscle simulation**. *Key Engineering Materials*, **345**:1241–1244, 2007. 32, 33
- [80] Z. ZHUANG, F. ZHANG, AND S. CEN. **ABAQUS nonlinear finite element analysis and examples**. *Science Press, Beijing*, pages 169–172, 2005. 32
- [81] I. L. JONES, M. WARNER, AND J. D. STEVENS. **Mathematical modelling of the elastic properties of retina: a determination of Young’s modulus**. *Eye*, **6**(6):556–559, 1992. 33
- [82] B. ALAMOUTI AND J. FUNK. **Retinal thickness decreases with age: an OCT study**. *British journal of ophthalmology*, **87**(7):899–901, 2003. 33
- [83] M. GOMEZ-PEREZ, P. YOUNG, AND V. B. XUAN. **New tools for analyzing biomechanical problems**. 33
- [84] M. ALI NASSERI, M. EDER, D. EBERTS, S. NAIR, M. MAIER, D. ZAPP, C. P. LOHMANN, AND A. KNOLL. **Kinematics and dynamics analysis of a hybrid parallel-serial micromanipulator designed for biomedical applications**. In *Advanced Intelligent Mechatronics (AIM), 2013 IEEE/ASME International Conference on*, pages 293–299. IEEE, 2013. 39, 61
- [85] L. ROMDHANE. **Design and analysis of a hybrid serial-parallel manipulator**. *Mechanism and Machine Theory*, **34**(7):1037–1055, 1999. 43
- [86] T. K. TANEV. **Kinematics of a hybrid (parallel–serial) robot manipulator**. *Mechanism and Machine Theory*, **35**(9):1183–1196, 2000. 43
- [87] G. YANG, W. CHEN, AND E. H. L. HO. **Design and kinematic analysis of a modular hybrid parallel-serial manipulator**. In *Control, Automation, Robotics and*

- Vision, 2002. ICARCV 2002. 7th International Conference on*, **1**, pages 45–50. IEEE, 2002. 43
- [88] M. ALI NASSERI, M. EDER, S. NAIR, E. C. DEAN, M. MAIER, D. ZAPP, C. P. LOHMANN, AND A. KNOLL. **The introduction of a new robot for assistance in ophthalmic surgery**. In *Engineering in Medicine and Biology Society (EMBC), 2013 35th Annual International Conference of the IEEE*, pages 5682–5685. IEEE, 2013. 45
- [89] J. DENAVIT AND R. S. HARTENBERG. **A kinematic notation for lower-pair mechanisms based on matrices**. *Trans. of the ASME. Journal of Applied Mechanics*, **22**:215–221, 1955. 44
- [90] I.A. SIGAL, J.G. FLANAGAN, I. TERTINEGG, AND C.R. ETHIER. **Finite element modeling of optic nerve head biomechanics**. *Investigative ophthalmology & visual science*, **45**(12):4378–4387, 2004. 50, 90
- [91] M.W. CHARLES AND N. BROWN. **Dimensions of the human eye relevant to radiation protection (dosimetry)**. *Physics in Medicine and Biology*, **20**(2):202, 1975. 50
- [92] M. PAK. *Mathematical Modelling and Parameter Estimation of a Stick-Slip Piezo Actuator*. Bachelor’s thesis, Technische Universität München, Munich, Germany, 2012. 72, 79, 110
- [93] S. BASHASH AND N. JALILI. **Robust Adaptive Control of Coupled Parallel Piezo-Flexural Nanopositioning Stages**. *IEEE/ASME Transactions on Mechatronics*, **14**(1):11–20, 2009. 79
- [94] Q. XU AND Y. LI. **Sliding mode control of a piezo-driven micropositioning system using extended Kalman filter**. In *Proceedings of the IEEE International Conference on Automation and Logistics (ICAL)*, pages 427–432, 2010. 79
- [95] N. AGHAKHANI, N. GERAVAND, M. AND SHAHRIARI, M. VENDITTELLI, AND G. ORILO. **Task Control with Remote Center of Motion Constraint for Minimally Invasive Robotic Surgery**. In *Proceedings of the IEEE International Conference on Robotics and Automation (ICRA)*, pages 5807–5812, 2013. 87, 88, 89
- [96] H. AZIMIAN, R.V. PATEL, AND M.D. NAISH. **On constrained manipulation in robotics-assisted minimally invasive surgery**. In *Proceedings of the 3rd IEEE RAS and EMBS International Conference on Biomedical Robotics and Biomechatronics (BioRob)*, pages 650–655, 2010. 87, 88
- [97] Y. NAKAMURA, H. HANAFUSA, AND T. YOSHIKAWA. **Task-priority based redundancy control of robot manipulators**. *The International Journal of Robotics Research*, **6**(2):3–15, 1987. 88

REFERENCES

- [98] J. BAILLIEUL. **Kinematic programming alternatives for redundant manipulators.** In *Proceedings of the IEEE International Conference on Robotics and Automation (ICRA)*, **2**, pages 722–728, 1985. 88, 89
- [99] H. SERAJI. **Configuration control of redundant manipulators: theory and implementation.** *Robotics and Automation, IEEE Transactions on*, **5**(4):472–490, 1989. 88
- [100] R.C.O. LOCKE AND R.V. PATEL. **Optimal Remote Center-of-Motion Location for Robotics-Assisted Minimally-Invasive Surgery.** In *Proceedings of the IEEE International Conference on Robotics and Automation (ICRA)*, pages 1900–1905, 2007. 88
- [101] R. HARTLEY AND A. ZISSERMAN. *Multiple view geometry in computer vision*. Cambridge university press, 2003. 90, 91
- [102] BITMAPWORLD. **Female head**, 2013. <http://www.turbosquid.com/3d-models/polygonal-female-head-3ds/265937>. Last accessed: December 16, 2013. 91
- [103] M. RICKERT. *Efficient Motion Planning for Intuitive Task Execution in Modular Manipulation Systems*. Phd thesis, Technische Universität München, Munich, Germany, 2011. 93
- [104] SMARACT GMBH. *SCU - Simple Control Unit RS232 Interface Documentation*, 2012. 93
- [105] M-Y JUNG, A. DEGUET, AND P. KAZANZIDES. **A component-based architecture for flexible integration of robotic systems.** In *Intelligent Robots and Systems (IROS), 2010 IEEE/RSJ International Conference on*, pages 6107–6112. IEEE, 2010. 97
- [106] M. HENNING AND M. SPRUIELL. **Distributed programming with ice.** *ZeroC Inc. Revision*, **3**, 2003. 97, 98